

**Numerical investigation of ageing in the
mechanical behaviour of crosslinked
polyurethane adhesives under the
influence of moisture**

Dissertation

zur Erlangung des Grades
des Doktors der Ingenieurwissenschaften
der Naturwissenschaftlich-Technischen Fakultät
der Universität des Saarlandes

vorgelegt von

Siva Pavan Josyula, M.Sc.

Saarbrücken
2023

Tag des Kolloquiums: 19.11.2024

Dekan:	Prof. Dr.-Ing. Dirk Bähre
Gutachter:	Prof. Dr. Martin H. Müser
	Prof. Dr.-Ing. Ralf Müller
Akad. Mitarbeiter:	Dr.-Ing. Idriss El Azhari
Vorsitz:	Prof. Dr. Ralf Busch

Acknowledgement

This dissertation is an outcome of two years and three months of research work carried out under the IGF-project 19730 N as a research assistant at Lehrstuhl für Angewandte Mechanik, Universität des Saarlandes. The IGF-project 19730 N is carried out in cooperation with Lehrstuhl für Adhäsion und Interphasen in Polymeren, Universität des Saarlandes and Fraunhofer-Institut für Fertigungstechnik und Angewandte Materialforschung (IFAM), Bremen.

First of all, I would like to express my deepest gratitude to my doctoral supervisor Prof. Dr.-Ing. Stefan Diebels for accepting me as a Ph.D. student under his guidance at Lehrstuhl für Angewandte Mechanik, Universität des Saarlandes. His constructive feedback and constant support helped me excel and accept challenges in completing this project. I want to extend my deepest gratitude to Prof. Dr. Martin H. Müser from Lehrstuhl Materialsimulation, Universität des Saarlandes and Prof. Dr.-Ing. habil. Ralf Müller from the Fachgebiet Kontinuumsmechanik, Fachbereich Bau- und Umweltingenieurwissenschaften, Technische Universität Darmstadt for accepting to be examiners of my dissertation.

I would like to sincerely thank the German Federation of Industrial Research Associations - AiF and the industrial partners for funding the project. Next, I would also like to thank my project partners Bettina Zimmer, M.Sc. from Lehrstuhl für Adhäsion und Interphasen in Polymeren, Universität des Saarlandes and Dipl.-Ing. Andreas Wulf, Dr.-Ing. Olaf Hesebeck, Dr. Katharina Koschek and Dr. Markus Brede from Fraunhofer-Institut für Fertigungstechnik und Angewandte Materialforschung for their cooperation and support in the experimental investigation required for understanding the ageing process in adhesives under the influence of moisture in this project.

Further, I would like to extend my gratitude to my colleagues at Lehrstuhl für Angewandte Mechanik, Universität des Saarlandes to participate in discussions and provide me with a friendly environment. I want to thank Praatek Sharma, M.Sc. and Ing. Luciano Fissore for long discussions on the numerical implementation of material models in deal.II. I want to extend my gratitude to apl. Prof. Dr.-Ing. Dr. rer. nat. Anne Jung for technical discussions, reviewing presentations and proofreading project reports written in German language with helpful suggestions.

I must express my profound gratitude to my family for the unflinching love and motivation they provided me since my childhood. Which gave me endless courage, support in all means to follow my dreams. I want to extend special thanks to my brother and his family for their continuous motivation and support throughout my doctoral studies.

Saarbrücken, October 2023

Siva Pavan Josyula

Abstract

Applications of adhesives are exponentially increasing in the production of lightweight bonded structures. The mechanical behaviour of these materials is very complex because of the ageing process under environmental conditions. IGF-project 19730 N addresses the ageing of crosslinked polyurethane adhesives under the influence of moisture concentration at an isothermal condition of 60° C. An extensive experimental investigation was planned with a primary focus on ageing and softening due to moisture absorption. The data generated from the experimental investigation is used for the numerical investigation. The motivation of this work is to develop material models to analyse the material behaviour using finite element method. The finite-strain viscoelastic behaviour is modelled based on phenomenological theories. The viscoelastic material model is coupled with the diffusion model to investigate the ageing of the mechanical behaviour. The Langmuir-type diffusion model is used in this work to investigate the anomalous moisture diffusion. Further, a phase-field fracture material model is implemented to investigate the crack propagation in the samples aged under different humid conditions. Finally, the damage model is coupled with the diffusion model to numerically analyse the moisture influence on fracture toughness of the material.

Zusammenfassung

Die Anwendungen von Klebstoffen zur Fertigung leichter Verbundstrukturen nehmen exponentiell zu. Aufgrund des Alterungsprozesses unter Umweltbedingungen ist das mechanische Verhalten dieser Materialien sehr komplex. IGF-Projekt 19730 N untersucht die Alterung von vernetzten Polyurethanklebstoffen unter dem Einfluss der Feuchtigkeit bei isothermen Bedingungen von 60° C. Es wurde eine extensive experimentelle Untersuchung geplant, bei der das Alterungsverhalten und die Weichmachung aufgrund von Feuchteaufnahme im Hauptgrund stehen. Die Ergebnisse der experimentellen Untersuchung werden für die numerische Untersuchung verwendet. Der Grund für diese Arbeit ist die Entwicklung von Materialmodellen zur Berechnung des Materialverhaltens mit Hilfe der Finite-Elemente-Methode. Das viskoelastische Verhalten wird auf der Grundlage phänomenologischer Theorien modelliert. Das viskoelastische Materialmodell wird mit dem Diffusionsmodell gekoppelt, um die Alterung des mechanischen Verhaltens zu untersuchen. Das Langmuir-Modell für die Diffusion wird in dieser Arbeit verwendet, um die anomale Feuchtigkeitsdiffusion zu untersuchen. Außerdem wird ein Phasenfeld-Bruchmaterialmodell implementiert, um die Rissausbreitung in den unter verschiedenen feuchten Bedingungen gealterten Proben zu untersuchen. Das Schadensmodell wird mit dem Diffusionsmodell gekoppelt, um den Einfluss der Feuchtigkeit auf die Bruchfestigkeit numerisch zu berechnen.

Contents

1	Introduction	1
1.1	Motivation and state of the art	2
1.1.1	Outline of thesis	4
2	Fundamentals of continuum mechanics	7
2.1	Kinematics of finite deformation	8
2.2	Stress tensors	11
2.3	Balance principles	12
3	Modelling coupled diffusion and finite-strain viscoelasticity	15
3.1	Modelling anomalous diffusion of moisture	15
3.1.1	Comparison of Langmuir and Fick's diffusion models	17
3.2	Finite-strain viscoelasticity	20
3.2.1	Kinematic split	24
3.3	Modelling the coupled formulation	25
3.3.1	Constitutive theory	26
3.3.2	Influence of moisture on viscoelastic properties	30
3.3.3	Governing equation	31

3.3.4	Boundary conditions	32
4	Phase-field modelling of fracture	33
4.1	Fundamentals of fracture	34
4.2	Griffiths's theory of failure	35
4.3	Modelling phase-field fracture model	35
4.3.1	Regularization of the crack surface density function	36
4.3.2	Degradation of the bulk energy	38
4.3.3	Degradation function	39
4.4	Thermodynamic consistency	40
4.4.1	Material theory	41
4.5	Governing balance equations	44
4.5.1	Boundary conditions	45
4.6	Mesh sensitivity study	45
5	Numerical implementation	51
5.1	Coupled diffusion and viscoelasticity	52
5.1.1	Linearisation	54
5.1.2	Finite element implementation	55
5.2	Modelling phase-field damage model	60
5.2.1	Finite element implementation	60
5.3	Implementation in deal.II	64
6	Identification of moisture diffusion parameters	67
6.1	Gravimetric investigation	68

6.1.1	Moisture diffusion in adhesive-A	69
6.1.2	Moisture diffusion in adhesive-B	70
6.2	Langmuir-type diffusion parameters	74
6.2.1	Diffusion parameters for adhesive-A	74
6.2.2	Diffusion parameters for adhesive-B	81
6.2.3	Effective diffusion parameters	83
7	Parameter identification of the ageing mechanical properties	87
7.1	Ageing of mechanical properties	88
7.1.1	Parameter identification for coupled formulation	92
7.1.2	Investigation of the coupled problem	93
7.2	Phase-field damage parameters	96
7.2.1	Dry sample	98
7.2.2	Aged sample	100
8	Coupled diffusion-deformation-damage	105
8.1	Diffusion coupled with phase-field damage	105
8.1.1	Thermodynamical consistency	106
8.1.2	Material theory	107
8.1.3	influence of moisture diffusion on fracture toughness	110
8.2	Boundary conditions	111
8.3	Finite element implementation	112
8.3.1	Numerical implementation	114
8.4	Numerical simulation of notched specimen	115

8.4.1	Moisture-dependent mechanical properties	117
8.5	Numerical evaluation	118
9	Summary and outlook	125
9.1	Summary	125
9.2	Outlook for the future work	127
A	Theoretical Background	145
A.1	Stress and elasticity tensors	145
B	Publications, Lectures and Posters	149
B.1	Publications and proceedings	149
B.2	Lectures	150
B.3	Poster	150

1

Introduction

The results presented in this dissertation were obtained as a part of AiF project (IGF-Project Nr. 19730 N) titled “Berechnung des instationären mechanischen Verhaltens von alternden Klebverbindungen unter Einfluss von Wasser auf den Klebstoff” at the Lehrstuhl für Angewandte Mechanik headed by Prof. Dr.-Ing. Stefan Diebels at the Universität des Saarlandes in cooperation with Lehrstuhl für Adhäsion und Interphasen in Polymeren headed by Prof. Dr. rer. nat. Wulff Possart at the Universität des Saarlandes and Dipl.-Ing. Andreas Wulf, Dr.-Ing. Olaf Hesebeck, Dr. Katharina Koschek and Dr. Markus Brede from Fraunhofer-Institut für Fertigungstechnik und Angewandte Materialforschung (IFAM), Bremen.

The demand for efficient structural components and products is growing with an increase in the applications of lightweight manufacturing methods of aircraft, wind energy [150] and automotive engineering [27, 9, 129, 33] or the need to miniaturise the components in technologically advanced areas like microelectronics [155]. Such complex applications in the modern industry can be achieved from composite structures engineered with various tailored materials. In manufacturing composite structures, the demand for efficient bonding methods is increasing to bond similar or distinct materials [131, 79, 10].

Adhesive bonding technology is one of the oldest bonding processes because of the practical advantages over friction and joining processes. The force transmission in bonded joints ensures a homogeneous stress distribution for the joint to remain intact during deformation and absorb high energies. Therefore, bonded joints are used in the crash zones of automobiles. In addition, using adhesive helps dampen vibrations and reduces mechanical stresses. For this reason, structural bonding is now a highly recommended joining technique, even in high-tech applications. Polymers dominate manufacturing lightweight structures or material composites such as coating and adhesive [104, 80, 156, 1]. Epoxies, polyamides and polyurethane are the most widespread structural adhesives.

1.1 Motivation and state of the art

The molecular interactions between the adhesive and the adherents result in the bonding of materials. These bonded joints are chosen because of their advantages over mechanically bonded joints. Nevertheless, the bonding process with adhesives is very complex because of the individual surface pre-treatment processes, adhesive mixing and application at bonded joints. The bonding process and the curing of adhesives need to be coordinated and controlled at a defined time, temperature and pressure.

The reliability of bonded joints for a longer product lifetime is the primary concern in the industrial application [66, 96, 107]. The adhesive material interacts with the surrounding atmosphere or diffusing media because its hygroscopic behaviour leads to ageing in the bonded joints [13, 93]. The term ageing defines changes in properties of the adhesive bond that occur during the service time [116]. The ageing of adhesives affects the performance of bonded joints resulting in the degradation of mechanical properties like strength, durability, and fracture toughness. Therefore, the influence of temperature and humidity must be considered in manufacturing bonded joints.

Crosslinked polyurethane adhesives are investigated to understand their mechanical behaviour in manufacturing bonded joints. The crosslinked polyurethane adhesives show large deformation viscoelastic behaviour. Therefore a finite-strain viscoelastic model is used to model the mechanical behaviour within the framework of continuum finite-strain theory. These

materials absorb moisture from the surrounding atmosphere because of their hygroscopic nature. Further, the mechanical and diffusion models are coupled to investigate the ageing process under moisture influence. A phase-field damage model is used to investigate the failure under tension in the aged samples.

Various research works are carried out on the numerical modelling of rubber-elastic, quasi-incompressible materials with conventional theories of material modelling based on the theories of continuum mechanics. These theories are classified into phenomenological [105, 123, 157, 64] and micro-mechanical models. Generally, the phenomenological models are formulated based on the principal invariants [105, 123, 124] to model hyperelastic behaviour. Many efforts are made to model time-dependent viscoelastic behaviour by extending phenomenological models with an evolution equation to describe viscous behaviour [122, 141, 58, 101, 86, 57, 121].

The early work of Treloar [143, 144, 145, 146] is the basis for most of the advanced micromechanically motivated material models. The initial work of Treloar [143, 144] concerns the molecular network theory and micromechanical approaches used in formulating hyperelasticity laws. It is necessary to distinguish between Gaussian and non-Gaussian theories in large deformations to model an efficient material model since they need to be more comprehensive in describing geometrical nonlinearity. Therefore, non-Gaussian theories based on inverse Langevin chain statistics are proposed to formulate network material models under large deformation. A typical example of a material model based on the Langevin function is proposed by Arruda and Boyce [8, 20], Anand [5], Bischoff et al. [14], and Wu et al. [153].

Experimental investigation performed to investigate the ageing process is used to develop a coupled diffusion and deformation material model. Many material models are proposed to analyse the moisture influence on the mechanical behaviour [30, 38, 106, 127, 148]. The influence of the fluid transport on the mechanical behaviour due to the swelling deformation is investigated in the polymer gels [61, 151]. Sharma et al. [130] have proposed a model to investigate polyamide ageing due to moisture transport. Goldschmidt et al. [46] investigated the ageing phenomena of epoxy adhesives under the influence of moisture with the coupled formulation. Fick's law of diffusion is more popular because of the simplistic formulation, but the diffusion in the crosslinked polyurethane adhesive is anomalous [67] in nature. Therefore, the diffusion material model proposed by Carter & Kibler [23] called Langmuir-type diffusion is used to simulate moisture absorption and desorption at an

isothermal condition. The Langmuir-type diffusion model is used to analyse the moisture transport in polymers [75, 137] and in structural adhesives like epoxy [117, 135, 140].

In order to manufacture reliable bonded joints, it must be demonstrated that the adhesives acting as an interface in bonded joints will not fail under operating loads. The failure of the adhesive bonds results from the separation caused by the growth of one or more cracks through the material. In this context, the damage behaviour is investigated with a phase-field theory of fracture, where a continuous field variable represents the cracks. This method allows a simple algorithmic implementation, as the crack surfaces need not be explicitly modelled. The Phase-field fracture is modelled based on a variational approach by minimising the energy potential to analyse the fracture behaviour [40]. Several contributions are made to model the ductile [25, 83, 97] and the brittle [6, 29, 36, 78, 149] fracture with phase-field fracture formulations. A Phase-field variable is introduced to distinguish between the damaged and undamaged material [19].

The parameters belonging to the material model must be identified to represent the material behaviour consistent with the experimental investigation. In the automated process of identification of parameters, the data sets obtained from the experiments are compared with data sets generated by numerical analysis. The error is minimised by optimising the parameters set [15]. Based on this gradient-free method, numerous works [45, 70] have already been carried out to identify the material parameters of material models to investigate viscoelastic materials. This work uses a gradient-free search algorithm to identify the optimal material parameters.

1.1.1 Outline of thesis

The objective of the dissertation is to model the mechanical behaviour of adhesives under the influence of moisture concentration. The experimental investigation for the moisture diffusion and mechanical behaviours are investigated at Lehrstuhl für Adhäsion und Interphasen in Polymeren, Saarland University and Fraunhofer-Institut für Fertigungstechnik und Angewandte Materialforschung (IFAM), Bremen. The test data obtained from the experimental investigation were used in this work to model diffusion, viscoelastic and fracture behaviours using the finite element method. These behaviours

are coupled to investigate the influence of moisture on mechanical behaviour. The thesis is organised as follows:

Chapter 2 presents the fundamentals of non-linear continuum mechanics used to model the mechanical behaviour of bodies under external loading conditions. This chapter also includes kinematics used to describe deformation, fundamental mapping of geometry, stress measures, and body motion. In addition, fundamental physical effects are introduced with the balance equations. At this point, the balance equation for momentum is explained in detail as it represents the basis for the subsequent implementation in the context of the finite element method.

Chapter 3 deals with the coupled formulation between moisture diffusion and finite-strain viscoelasticity to understand the ageing of the material under the moisture influence. The moisture transport is modelled with the Langmuir-type diffusion model to consider mobile and immobile moisture concentrations. The moisture diffused in the material will degrade the stiffness of the material. Therefore moisture dependent stiffness parameters are defined to formulate the multi-physically coupled material model. Hence, the constitutive equations for stress are calculated as a function of the local moisture concentration.

Chapter 4 introduces the phase-field fracture model based on the variational approach for a viscoelastic material. The generalised formulation for phase-field fracture is based on the diffusive crack in the geometry, and this formulation is derived by regularising the crack surface. The phase-field equation for fracture is governed by the crack driving force.

Chapter 5 deals with the numerical aspects involved in this work. This chapter briefly describes the numerical methods used to implement the material theory in the open-source finite element library deal.II [7]. The implementation of the coupled material models discussed in Chapters 3 and 4 within the finite element method framework are explained with the help of algorithms in this chapter.

This work investigates two commercially available adhesives, adhesive-A and adhesive-B, for moisture diffusion. The ageing of mechanical behaviour under the influence of moisture is numerically investigated on the adhesive-A. **Chapter 6** focuses on identifying the material parameters of the Langmuir-type diffusion model for both commercial adhesives. The gradient-free algorithm proposed by Nelder & Mead [109] is used to identify the optimal material

parameters. The diffusion test data used to identify the optimal parameters of the Langmuir-type diffusion model are carried out at Fraunhofer-Institut für Fertigungstechnik und Angewandte Materialforschung (IFAM), Bremen.

Chapter 7 discusses identifying the mechanical parameters and the numerical investigations on the multi-physically coupled diffusion and viscoelasticity. The uniaxial tensile tests conducted at Lehrstuhl für Adhäsion und Interphasen in Polymeren, Saarland University on aged samples of adhesive-A are used to investigate the moisture influence on the viscoelastic behaviour of the material. The optimal stiffness parameters identified from the curve fitting process are investigated to derive the relationship between the stiffness parameters and moisture concentration. Tear tests are carried out on the aged angular sample following DIN ISO 34-1 standard to investigate the tear strength of the adhesive at Fraunhofer-Institut für Fertigungstechnik und Angewandte Materialforschung (IFAM), Bremen. The tear test data is used to identify the critical energy release rate required to investigate damage behaviour using a phase-field damage model.

In **Chapter 8**, the multi-physically coupled material model formulation between viscoelasticity, moisture diffusion and phase-field damage is discussed. The stability of the proposed formulation is discussed with the help of numerical examples. In this, a double V-notched sample is used to perform a numerical investigation for the damage behaviour on the aged samples with inhomogeneous moisture distribution. The load-displacement data from numerical simulations of the samples with inhomogeneous moisture distribution is compared with the results of dry and saturated samples to check the reliability of the material model.

Since modelling polymer adhesive bonds is highly complex, a description of the material behaviour can only be comprehensive sometimes. For this reason, an outlook on possible future work is given in the conclusion. **Chapter 9** briefly summarises the work carried out in the thesis.

2

Fundamentals of continuum mechanics

This chapter summarises the fundamental equations of continuum mechanics necessary to develop and understand the proposed material model concerning the finite-strain viscoelastic behaviour of a material. The quantities and methods are introduced to provide an overview for a reader of this thesis. Marques and Creus [94], Cho [26], and others offer supplementary literature on viscoelasticity. The kinematics of large deformations and stresses in the continuum are explained initially. Subsequently, conservation laws associated with the finite element formulation are introduced. Detailed explanations of continuum mechanics and the conservation laws discussed here are found in references [16, 50, 56, 63, 85] and the fundamentals of the finite element method are summarised by Zienkiewicz et al. [159, 160].

A macroscopic body \mathcal{B} is a system of an infinite set of uniformly and continuously distributed material points. Physical quantities such as stresses, displacements or temperatures are associated with the material points. The body is defined in a three-dimensional Euclidean space at time $t > 0$ with the boundary $\partial\mathcal{B}$. A base system \mathbf{e}_i with $i = 1, 2, 3$ is defined for the material point of the problem, where the position vector is defined to identify each material point.

2.1 Kinematics of finite deformation

Kinematics describes geometry, motion, and deformation of the body's \mathcal{B} as a function of time t . Each material point of the body is described by a position vector $\mathbf{x}(\boldsymbol{\chi}, t)$ in Euclidean space. The position vectors of the material points of the body in the reference configuration are expressed by the vector $\mathbf{X}(\boldsymbol{\chi}, t)$. For time $t > t_0$, the position vectors are represented by the vector $\mathbf{x}(\boldsymbol{\chi}, t)$ in the current configuration, see Figure 2.1.

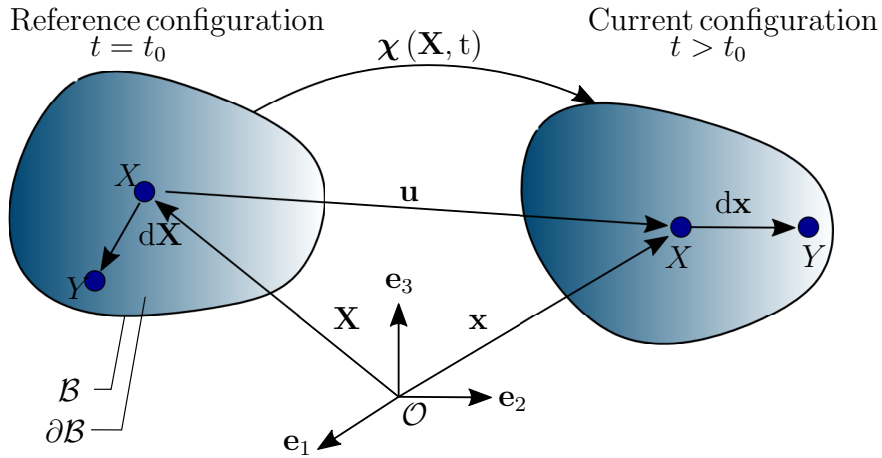


Figure 2.1: Description of the continuum material domain in reference (left) and current configuration (right)

The motion of the body is defined with a vector field $\boldsymbol{\chi}$ using the unique mapping of the body from the reference to current configurations. Here, the position \mathbf{x} of a material point in the current configuration is a function of the time t and the reference configuration's position vector \mathbf{X} . Since the motion of the deformable body $\boldsymbol{\chi}$ is invertible, the material point can be traced back from the current configuration into the reference configuration \mathbf{X} with the inverse of the motion $\boldsymbol{\chi}^{-1}$. The definition for position vectors in the current and reference configurations follows

$$\mathbf{x} = \boldsymbol{\chi}(\mathbf{X}, t), \quad \mathbf{X} = \boldsymbol{\chi}^{-1}(\mathbf{x}, t). \quad (2.1)$$

The gradient is represented as the derivative with respect to the position vector \mathbf{x} of the current configuration

$$\text{grad}(\bullet) = \frac{\partial(\bullet)}{\partial \mathbf{x}}, \quad (2.2)$$

symbol $\text{div}(\bullet)$ used later is associated with the divergence operator related to $\text{grad}(\bullet)$. In contrast, the derivative with respect to the position vector \mathbf{X} of the reference configuration is represented with

$$\text{Grad}(\bullet) = \frac{\partial(\bullet)}{\partial \mathbf{X}}. \quad (2.3)$$

The displacement vector describes the motion of a material point from the reference to the current configurations. This displacement vector is calculated as the difference between the current and the reference configuration position vectors. The displacement vector \mathbf{u} is expressed as

$$\mathbf{u}(\mathbf{X}, t) = \mathbf{x}(\mathbf{X}, t) - \mathbf{X}. \quad (2.4)$$

The partial derivative of the motion function to the position vector \mathbf{X} of the reference configuration results in the local deformation gradient tensor \mathbf{F}

$$\mathbf{F} = \frac{\partial \boldsymbol{\chi}(\mathbf{X}, t)}{\partial \mathbf{X}} = \frac{\partial \mathbf{x}}{\partial \mathbf{X}} = \text{Grad } \mathbf{x} = \mathbf{I} + \text{Grad } \mathbf{u}, \quad (2.5)$$

where \mathbf{I} is the second-order tensor. The deformation gradient tensor \mathbf{F} is used to map the differential line element $d\mathbf{X}$ of the reference configuration to the line element $d\mathbf{x}$ of the current configuration using

$$d\mathbf{x} = \mathbf{F} \cdot d\mathbf{X}. \quad (2.6)$$

The description of the motion $\boldsymbol{\chi}(\mathbf{X}, t)$ is unique and invertible. Therefore, the inverse of the deformation gradient tensor \mathbf{F}^{-1} exists, which maps the infinitesimal line element $d\mathbf{x}$ back to the reference configuration

$$d\mathbf{X} = \mathbf{F}^{-1} \cdot d\mathbf{x} \quad \text{with} \quad \mathbf{F}^{-1} = \frac{\partial \mathbf{X}}{\partial \mathbf{x}}. \quad (2.7)$$

The Jacobi determinant of the deformation gradient tensor \mathbf{F} measures volume change due to the body's deformation. This measure is used to map an infinitesimal volume element dV in the reference configuration onto a deformed volume element dv in the current configuration with

$$dv = J dV, \quad (2.8)$$

where the Jacobi determinant is calculated as

$$J = \det \mathbf{F}. \quad (2.9)$$

A relationship between a vector element $d\mathbf{A}$ of an infinitesimal surface element in the reference configuration and a surface element in the current configuration $d\mathbf{a}$ is established with the help of the deformation gradient tensor \mathbf{F} and the Jacobi determinant J

$$d\mathbf{a} = (\det \mathbf{F})\mathbf{F}^{-T} \cdot d\mathbf{A}. \quad (2.10)$$

The deformation of a body comprises a rigid body motion and the actual deformation. The deformation gradient tensor is associated with the orthogonal rotation tensor \mathbf{R} and right stretch tensor \mathbf{U} or left stretch tensor \mathbf{V} . Thus, the deformation gradient tensor is decomposed as

$$\mathbf{F} = \mathbf{R} \cdot \mathbf{U} = \mathbf{V} \cdot \mathbf{R}. \quad (2.11)$$

The deformation tensor describes the local change in the distance due to deformation as the square of the differential line element. The deformation tensor in the reference configuration is defined using the right Cauchy-Green deformation tensor \mathbf{C} as

$$\mathbf{C} = \mathbf{F}^T \cdot \mathbf{F} = \mathbf{U}^2 \text{ with } dx^2 = d\mathbf{X} \cdot \mathbf{C} \cdot d\mathbf{X}, \quad (2.12)$$

analogously the deformation tensor in the current configuration is expressed with the left Cauchy-Green deformation tensor \mathbf{B} as

$$\mathbf{B} = \mathbf{F} \cdot \mathbf{F}^T = \mathbf{V}^2 \text{ with } d\mathbf{X}^2 = d\mathbf{x} \cdot \mathbf{B}^{-1} \cdot d\mathbf{x}. \quad (2.13)$$

The strain tensors are introduced as a difference in the squares of the line elements for the current and reference configurations. The most common choice of strain measurement is the Cauchy-Green-Lagrange strain tensor \mathbf{E} in the reference configuration

$$\mathbf{E} = \frac{1}{2}(\mathbf{C} - \mathbf{I}), \quad (2.14)$$

while the strain measures in the current configuration are expressed using the Euler-Almansi strain tensor as

$$\mathbf{A} = \frac{1}{2}(\mathbf{I} - \mathbf{B}^{-1}). \quad (2.15)$$

The tensors \mathbf{E} and \mathbf{A} can be transformed into one another using “push-forward” and “pull-back” mathematical operations. The relationship between \mathbf{E} and \mathbf{A} is defined with the mathematical operations as

$$\mathbf{A} = \mathbf{F}^{-T} \cdot \mathbf{E} \cdot \mathbf{F}^{-1}, \quad \mathbf{E} = \mathbf{F}^T \cdot \mathbf{A} \cdot \mathbf{F}. \quad (2.16)$$

A detailed explanation of the kinematics for the finite-strain deformation can be found in the literature [34].

2.2 Stress tensors

The kinematics of a deformable body has been described so far, but not how deformations are caused. The resulting stresses inside the body must be considered to represent the body’s behaviour due to external loads. External loads are divided into volume forces and surface forces. Volume forces such as gravity act on the entire body, and the surface loads act on the surface alone.

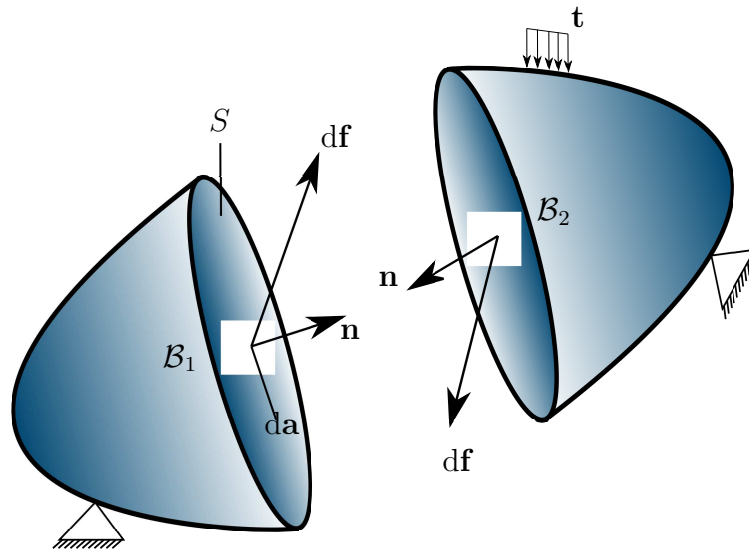


Figure 2.2: Section of a body subjected to an external load

Figure 2.2 shows an imaginary section along the surface to illustrate the quantities acting inside the body. This imaginary section divides the body into two parts \mathcal{B}_1 and \mathcal{B}_2 . The local force $d\mathbf{f}$ at the imaginary cross-section

is related to the corresponding partial surface da . Since the sectional forces are assumed to be continuously distributed over the cross-sectional surfaces, the traction vector \mathbf{t} is defined as a finite limit value of the quotient of the resulting load vector $\Delta\mathbf{f}$ and the infinitesimal area element Δa

$$\mathbf{t} = \lim_{\Delta a \rightarrow 0} \frac{\Delta\mathbf{f}}{\Delta a} = \frac{d\mathbf{f}}{da}. \quad (2.17)$$

The orientation of the surface element da is given by its normal vector \mathbf{n} resulting in a vector-valued area element. Based on the Cauchy stress theorem, a relationship between the traction vector \mathbf{t} and the normal vector \mathbf{n} is defined as

$$\mathbf{t} = \mathbf{T} \cdot \mathbf{n}. \quad (2.18)$$

In the equation (2.18), \mathbf{T} is the Cauchy stress formulated by linearly mapping the normal vector to the stress tensor. The Cauchy stress is defined in the deformed state of the current configuration. Alternatively, the stresses in the current configuration are calculated with the Kirchhoff stress tensor $\boldsymbol{\tau}$ based on the Cauchy stress tensor. The Kirchhoff stress tensor is often used in the numerical implementation of the viscoelastic behaviour

$$\boldsymbol{\tau} = J\mathbf{T}. \quad (2.19)$$

2.3 Balance principles

The balance equations describe universal laws of nature independent of the continuum properties and are valid for all materials. Balance equations are first given in integral form as global statements for the entire body. For sufficiently smooth fields of the quantities to be balanced, it is possible to choose local formulations as differential equations of an arbitrarily small fraction of the body. In continuum mechanics, the balance equations for mass, momentum, moment of momentum, energy, and entropy are considered [34, 120]. The following chapter discusses the necessary balance equations to evaluate mechanical behaviour. For details on the other balance equations, references are suggested for a general case of finite deformation [147, 63, 56].

The axiom for the balance of momentum is given as a temporal change in

the momentum \mathbf{l} equals the resultant forces \mathbf{f} acting on the body \mathcal{B}

$$\dot{\mathbf{l}} = \mathbf{f}. \quad (2.20)$$

In deriving the balance equation of momentum, the momentum density of a body is determined as the product of mass density ρ and its velocity $\mathbf{v} = \dot{\mathbf{x}}$. The forces \mathbf{f} acting on the body are classified into external contact and local external body forces $\partial\mathcal{B}$. The resulting forces are obtained by integrating the external contact force \mathbf{t} over the actual placement's surface $\partial\mathcal{B}$ and the external body force $\rho \mathbf{b}$ over the actual body volume. The external body force is typically due to the effects of gravitational pull. The balance of momentum is derived from the momentum and forces as

$$\frac{d}{dt} \int_{\mathcal{B}} \rho \dot{\mathbf{x}} \, dv = \int_{\partial\mathcal{B}} \mathbf{t} \, da + \int_{\mathcal{B}} \rho \mathbf{b} \, dv, \quad (2.21)$$

with ρ as the mass density. The global statement for the balance of momentum is derived with the help of the balance of mass $\dot{\rho} + \rho \operatorname{div} \dot{\mathbf{x}} = 0$ and by applying the divergence theorem to the surface integral of the equation (2.21) leading to momentum balance

$$\int_{\mathcal{B}} (\rho \ddot{\mathbf{x}} - \operatorname{div} \mathbf{T} - \rho \mathbf{b}) \, dv = \mathbf{0}. \quad (2.22)$$

Equation (2.22) must hold good for any given volume. Hence the expression has to agree with the local statement

$$\operatorname{div} \mathbf{T} + \rho (\mathbf{b} - \ddot{\mathbf{x}}) = \mathbf{0}. \quad (2.23)$$

Since quasi-static behaviour is assumed in the present work, the dependence of acceleration $\ddot{\mathbf{x}}$ and body forces acting on the body are not considered. Thus, the local statement for the balance of momentum is reduced to

$$\operatorname{div} \mathbf{T} = \mathbf{0}. \quad (2.24)$$

The introduced stress and deformation measures form the basis for the general characterisation of the material behaviour. They are used in the following to develop and implement a material model to represent the behaviour

of crosslinked polyurethane systems. Furthermore, assumptions regarding kinematics are essential for characterising inelastic material behaviour due to viscous effects.

To define a thermodynamically consistent material model, the material model must satisfy the balance of internal energy ϵ (first law of thermodynamics). The balance of energy describes the thermo-mechanical effects coupling the thermal and mechanical fields. The ageing of adhesives under the moisture influence is investigated in isothermal conditions; therefore, the thermal fields are neglected. The balance of energy for the coupled diffusion and mechanical effects is given as

$$\rho\dot{\epsilon} - \mathbf{T} : \mathbf{D} + \text{div}(R_m \mathbf{q}) = 0, \quad (2.25)$$

where R_m is the chemical potential and \mathbf{q} is the moisture flux. Taking into account the balance of energy (2.25), the entropy inequality is defined for an isothermal condition as

$$\rho\dot{\epsilon} - \mathbf{T} : \mathbf{D} + \text{div}(R_m \mathbf{q}) \geq 0. \quad (2.26)$$

The free energy function W is introduced in the entropy inequality in the form of the Legendre transformation for an isothermal condition as $W = \epsilon$ leading to the Clausius-Planck inequality [71, 138]

$$\rho\dot{W} - \mathbf{T} : \mathbf{D} + \text{div}(R_m \mathbf{q}) \geq 0. \quad (2.27)$$

3

Modelling coupled diffusion and finite-strain viscoelasticity

The hygroscopic property of the crosslinked polyurethane adhesives causes the moisture to diffuse from the atmosphere leading to the ageing of the material. A multi-physically coupled material model is proposed in this chapter to investigate the ageing process. The coupled material model is formulated by coupling a finite-strain viscoelastic model with a diffusion model. Here, the viscoelastic behaviour is modelled with a phenomenological viscoelastic model under large deformation and coupled with the Langmuir-type diffusion model. The Langmuir-type diffusion model is used because of the anomalous moisture diffusion typically seen in the polymers.

3.1 Modelling anomalous diffusion of moisture

Diffusion is the transport of molecules from a high-concentration system to a low-concentration system due to a larger concentration gradient. The mois-

ture diffusion in crosslinked polyurethane adhesives shows anomalous behaviour leading to mobile and immobile moisture concentrations [67]. The moisture molecules that are physically free to diffuse in spatial direction with time are referred to as mobile moisture concentration, and the molecules forming a reversible physical bond with the polymer chains are referred to as immobile moisture concentration [118, 134].

The moisture transport is generally modelled with Fick's second law of diffusion [38]. However, Fick's model does not consider the discontinuous behaviour on account of the relaxation of molecules after settling in pockets of free volume resulting in a non-Fickian behaviour [2, 30, 142]. In the other case of anomalous moisture diffusion, Fick's law does not distinguish between the mobile and the immobile moisture concentrations. Therefore, the Langmuir-type diffusion model [23] is used in this work and the diffusion equation is

$$\dot{m} = D \Delta m_f = D \operatorname{div} (\operatorname{grad} (m - m_b)), \quad (3.1)$$

where $(\dot{\bullet})$ is the material time derivative $d(\bullet)/dt$, D is the diffusion coefficient defining the concentration of moisture diffused through a unit area in a unit of time. m_f and m_b are mobile and immobile moisture concentrations and the total moisture concentration m is calculated as the algebraic sum of mobile and immobile concentrations $m = m_f + m_b$. $m = m_b + m_f = 0$ represents the dry state and $m = m_b + m_f = m_\infty(H)$ represents a saturation state, where $m_\infty(H)$ is the total moisture concentration at the saturation state for $H\%$ of humid climate condition.

The immobile moisture concentration of the Langmuir-type diffusion model is evaluated with the help of an evolution equation

$$\dot{m}_b = \alpha m - (\alpha + \beta) m_b. \quad (3.2)$$

The symbol α is a material parameter that amounts to the rate at which the mobile moisture becomes immobile, and β represents the rate at which the immobile moisture becomes mobile. The rate of change in immobile concentration is zero $\dot{m}_b = 0$ at equilibrium. As a result, the equilibrium equation is expressed as

$$\alpha m_f^\infty = \beta m_b^\infty, \quad (3.3)$$

m_f^∞ and m_b^∞ are the mobile and immobile moisture concentrations at the equilibrium state. Equation (3.3) holds to the entire body irrespective of spatial position. The mobile and the immobile concentrations can be calculated from the total moisture concentration $m_\infty = m_f^\infty + m_b^\infty$ at the equilibrium

state as

$$m_f^\infty = \frac{m_\infty}{1 + \alpha/\beta}, \quad m_b^\infty = \frac{\frac{\alpha}{\beta}m_\infty}{1 + \alpha/\beta}. \quad (3.4)$$

Both initial and boundary conditions are required to solve the diffusion problem. The boundary conditions are defined with the Dirichlet and Neumann boundary conditions, and the initial conditions are assigned to the entire spatial material domain Ω at time $t_0 = 0$

$$m(\mathbf{x}, t = 0) = m_0(\mathbf{x}), \quad m_b(\mathbf{x}, t = 0) = m_{b_0}(\mathbf{x}) \quad \forall \mathbf{x} \in \Omega. \quad (3.5)$$

The moisture concentration is specified on the Dirichlet boundaries $\partial\Omega_D$, and the moisture flux represents the Neumann boundary condition across the boundary $\partial\Omega_N$. The Dirichlet and the Neumann boundaries in the material domain Ω need to satisfy the conditions

$$\partial\Omega_N \cup \partial\Omega_D = \partial\Omega, \quad \partial\Omega_N \cap \partial\Omega_D = \emptyset. \quad (3.6)$$

The applied Dirichlet boundary conditions are

$$m(\mathbf{x}, t) = m_D \quad \forall \mathbf{x} \in \partial\Omega_D, \quad (3.7)$$

where m_D is the total moisture concentration measured for the saturated sample, and the Neumann boundary conditions are

$$\mathbf{q} \cdot \mathbf{n} = D(\text{grad } m_f) \cdot \mathbf{n} = q(\mathbf{x}, t) \quad \forall \mathbf{x} \in \partial\Omega_N, \quad (3.8)$$

where the moisture flux \mathbf{q} over the boundary $\partial\Omega_N$ is given by

$$\mathbf{q} = -D \frac{\partial m_f}{\partial \mathbf{x}} = -D(\text{grad } m_f), \quad (3.9)$$

and \mathbf{n} is the outward normal vector on the domain boundary.

3.1.1 Comparison of Langmuir and Fick's diffusion models

Langmuir-type diffusion is compared with Fick's diffusion to establish the need for a material model based on anomalous diffusion behaviour. Fick's

first Law describes the material flux \mathbf{q} as

$$\mathbf{q} = -D \text{grad } m, \quad (3.10)$$

where D is the diffusion coefficient and $\text{grad } m$ is the moisture concentration gradient. Fick's second law describes the balance of mass for the diffusive fluids, and the localised form of diffusion is

$$\dot{m} = -\text{div } \mathbf{q}. \quad (3.11)$$

Inserting equation (3.10) in Fick's second law of diffusion leads to

$$\dot{m} = D \text{div} (\text{grad } m). \quad (3.12)$$

The moisture concentration and flux are the Dirichlet and Neumann boundary conditions for Fick's diffusion model. Fick's diffusion model also follows the conditions for the Dirichlet $\partial\Omega_D$ and Neumann $\partial\Omega_N$ boundaries given in the equation (3.6) and the boundary conditions given in equations (3.7) and (3.8). The comparison of Fick's diffusion and Langmuir-type diffusion is conducted on a polyurethane adhesive of thickness 2.5 mm. The experimental investigation is carried-out at Lehrstuhl für Adhäsion und Interphasen in Polymeren (LAIP), Saarland University. The numerical simulation results of Fick and Langmuir-type diffusion models are compared with the moisture diffusion test data as shown in the figure (3.1). The parameters¹ of Fick's and Langmuir-type diffusion models are listed in Table 3.1.

Table 3.1: Parameters of Fick and Langmuir diffusion models

	D [mm ² s ⁻¹]	α [s ⁻¹]	β [s ⁻¹]
Langmuir-type diffusion	2.9e - 06	2.4e - 06	3.9e - 06
Fick diffusion	2.9e - 06	-	-

The classical evaluation of the diffusion behaviour is considered a function of the square root of time to follow classical Fick's law of diffusion considering linear mass uptake [31]. The investigation for moisture diffusion is carried out for one-dimensional moisture diffusion using gravimetric tests. Figure 3.1 shows the gravimetric test (Experimental) and the numerical investigation performed using Fick's and Langmuir-type diffusion models to investigate the

¹The material parameters of Fick's and Langmuir-type diffusion models are obtained through the curve fitting process. The details of the curve fitting are given in chapter 6.

moisture absorption in polyurethane adhesive. Fick's diffusion curve follows the experimental curve until the start of the second plateau of the moisture uptake at $\approx 410\sqrt{s}$. The numerical investigation performed with Langmuir-type diffusion shows a good fit with the experimental data.

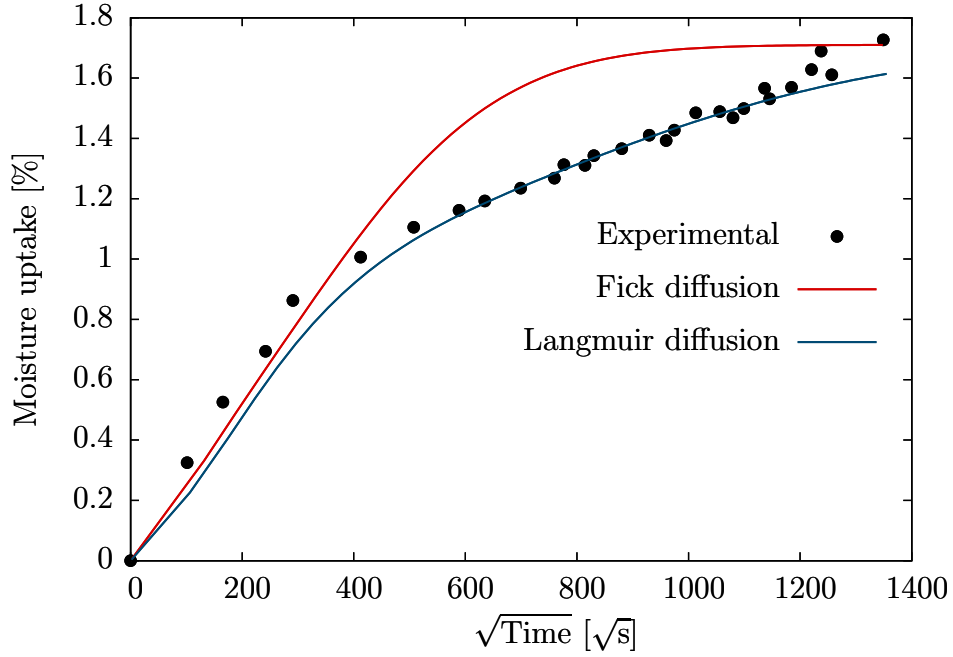


Figure 3.1: Comparison of Fick and Langmuir-type diffusion with the experimental test data. Gravimetric tests for moisture absorption (Experimental) are conducted at LAIP, Saarland University.

Since the results from the Langmuir-type diffusion model follows the experimental test data, the simulation data from the Langmuir-type diffusion model is further investigated to understand the anomalous diffusion. Figure 3.2 compares the simulation and test data, where the total, mobile and immobile moisture concentrations are obtained from the numerical simulation using the Langmuir-type diffusion model. From the plotted curve, it is evident that the moisture absorption is initially dominated by Fickian diffusion. Then the moisture absorption is followed by slower absorption due to the secondary absorption. The secondary absorption rate corresponds to immobile moisture concentration, and the slower absorption corresponds to mobile moisture. The total moisture concentration is calculated as the algebraic sum of mobile- and immobile concentrations. The second plateau is seen in the diffusion tests at time $\sqrt{t} = 410\sqrt{s}$ due to increased immobile concentration

with time. The mobile moisture reaches a maximum at $\sqrt{t} = 420\sqrt{s}$ and then transforms into immobile moisture until saturation.

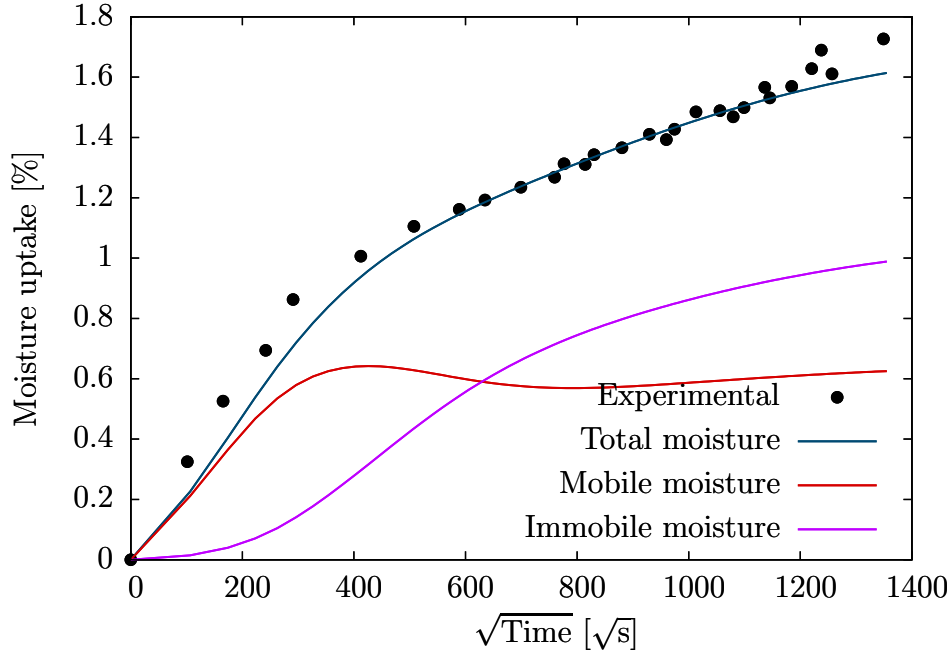


Figure 3.2: Moisture diffusion in the sample with Langmuir-type diffusion

3.2 Finite-strain viscoelasticity

This section discusses a one-dimensional viscoelastic model based on the rheological model as a foundation principle to derive constitutive equations for a viscoelastic material model under large deformations. The rheological model consists of a spring element connected in parallel with $j = 1, 2, \dots, n$ spring-dashpot elements (Maxwell elements) as shown in Figure 3.3. The spring element represents the material's elasticity, and a Maxwell element describes the rate-dependent behaviour. A Maxwell element approximates the relaxation of the viscoelastic material with discrete relaxation time. A discrete spectrum of relaxation time is considered by combining several Maxwell elements in parallel.

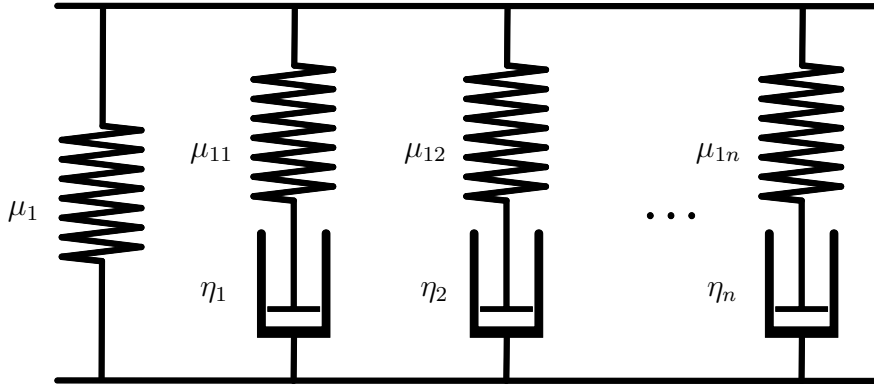


Figure 3.3: Rheological model of the viscoelasticity with n Maxwell elements.

Figure 3.4 shows the schematic description of the Maxwell element, where a Hooke element (spring) of stiffness μ_{1n} is connected in series with a Newton element (dashpot) with viscosity η_n .

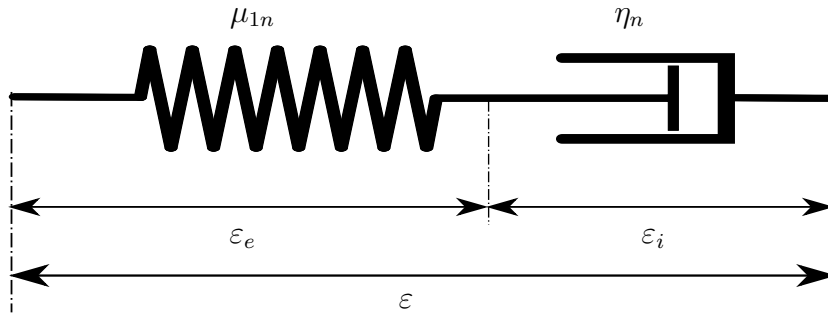


Figure 3.4: Maxwell element

The strain ε in the Maxwell element is computed as a sum of strains of the spring ε_e and the dashpot ε_i , whereas the stresses in both elements are equal

$$\varepsilon = \varepsilon_e + \varepsilon_i, \quad \sigma = \sigma_e = \sigma_i. \quad (3.13)$$

The finite-strain viscoelastic model is developed based on the rheological model shown in Figure 3.3. An essential step in implementing the material model is to multiplicatively decompose the deformation gradient \mathbf{F} into elastic and inelastic parts [88, 87]. The multiplicative decomposition of the deformation gradient introduces a fictitious intermediate configuration to represent a relaxed local state. Therefore, each Maxwell element must have a

fictitious intermediate configuration.

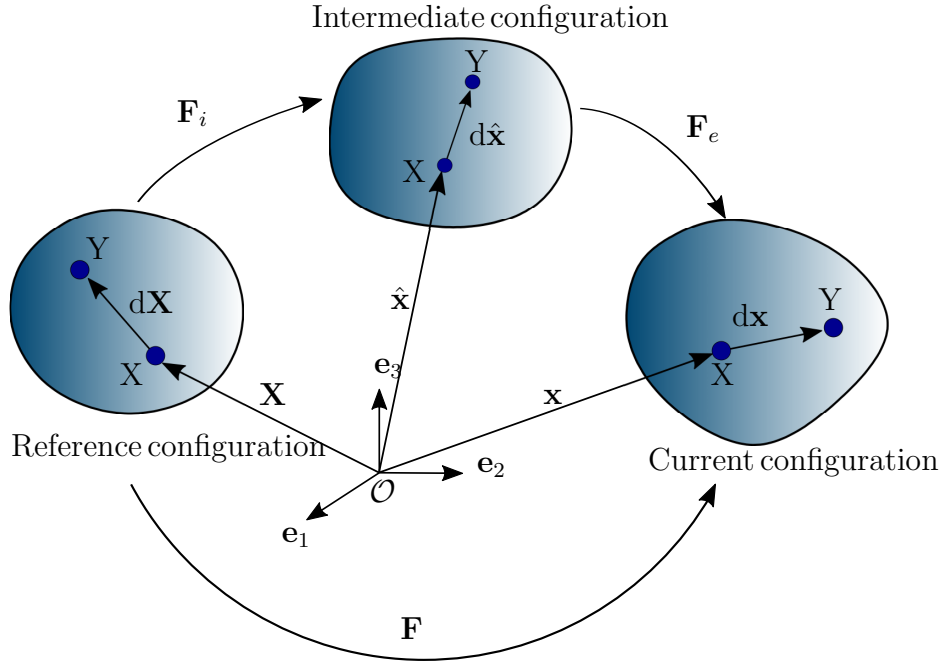


Figure 3.5: Multiplicative decomposition of the deformation gradient based on a fictitious intermediate configuration

Figure 3.5 shows the schematic representation of the multiplicative decomposition of deformation tensor into elastic \mathbf{F}_e and inelastic \mathbf{F}_i parts [48, 89, 92, 122, 141]. The decomposition of the deformation gradient is [91]

$$\mathbf{F} = \mathbf{F}_e \cdot \mathbf{F}_i. \quad (3.14)$$

The line elements of reference, intermediate and current configurations are defined with $d\mathbf{X}$, $d\hat{\mathbf{x}}$ and $d\mathbf{x}$. The line element of a configuration can be transformed into another configuration using the deformation gradient \mathbf{F} and the decomposed components of the deformation gradients \mathbf{F}_e and \mathbf{F}_i . The transformation relations of the line elements are

$$\begin{aligned} d\mathbf{x} &= \mathbf{F} \cdot d\mathbf{X}, \\ d\hat{\mathbf{x}} &= \mathbf{F}_i \cdot d\mathbf{X}, \\ d\mathbf{x} &= \mathbf{F}_e \cdot d\hat{\mathbf{x}}. \end{aligned} \quad (3.15)$$

The strain tensor $\mathbf{\Gamma}$ of the intermediate configuration is calculated with the

“push-forward” and the “pull-back” mathematical relationships [141, 89, 122, 92, 48]. The strain tensor $\mathbf{\Gamma}$ is determined from the push-forward transformation of the Green-Lagrangian strain tensor \mathbf{E} with the inelastic deformation gradient \mathbf{F}_i as

$$\mathbf{\Gamma} = \mathbf{F}_i^{-T} \cdot \mathbf{E} \cdot \mathbf{F}_i^{-1} \quad (3.16)$$

or from the pull-back transformation of the Almansi strain tensor \mathbf{A} with the elastic part \mathbf{F}_e of the deformation gradient as

$$\mathbf{\Gamma} = \mathbf{F}_e^T \cdot \mathbf{A} \cdot \mathbf{F}_e. \quad (3.17)$$

The strain tensor $\mathbf{\Gamma}$ of the intermediate configuration can be additionally split into elastic part $\mathbf{\Gamma}_e$ of the Green-Lagrange type of the strain tensor and the inelastic part $\mathbf{\Gamma}_i$ of the Almansi type of the strain tensor

$$\mathbf{\Gamma} = \mathbf{\Gamma}_e + \mathbf{\Gamma}_i, \quad (3.18)$$

and the elastic $\mathbf{\Gamma}_e$ and the inelastic $\mathbf{\Gamma}_i$ parts are

$$\mathbf{\Gamma}_e = \frac{1}{2} (\mathbf{F}_e^T \cdot \mathbf{F}_e - \mathbf{I}) \quad \text{und} \quad \mathbf{\Gamma}_i = \frac{1}{2} (\mathbf{I} - \mathbf{F}_i^{-T} \cdot \mathbf{F}_i^{-1}). \quad (3.19)$$

The deformation measures of the j^{th} Maxwell element defined at the intermediate configuration are the right elastic Cauchy-Green deformation tensor \mathbf{C}_e^j and the inverse of the left inelastic Cauchy-Green deformation tensor $(\mathbf{B}_i^j)^{-1}$

$$\mathbf{C}_e^j = \mathbf{F}_e^T \cdot \mathbf{F}_e, \quad (\mathbf{B}_i^j)^{-1} = (\mathbf{F}_i \cdot \mathbf{F}_i^T)^{-1}. \quad (3.20)$$

The inelastic right Cauchy-Green deformation tensor \mathbf{C}_i^j in the reference configuration and the elastic left Cauchy-Green deformation tensor \mathbf{B}_e^j in the current configuration of the j^{th} Maxwell element are given by

$$\mathbf{C}_i := \mathbf{F}_i^T \cdot \mathbf{F}_i, \quad \mathbf{B}_e := \mathbf{F}_e \cdot \mathbf{F}_e^T. \quad (3.21)$$

The elastic left Cauchy-Green deformation tensor \mathbf{B}_e^j can be expressed in terms of the inelastic right Cauchy-Green deformation tensor \mathbf{C}_i^j with the

deformation gradient \mathbf{F} in the intermediate configuration as

$$\mathbf{B}_e^j = \mathbf{F} \cdot (\mathbf{C}_i^j)^{-1} \cdot \mathbf{F}^T. \quad (3.22)$$

3.2.1 Kinematic split

A nearly incompressible material behaviour motivates the multiplicative decomposition of the deformation gradient tensor into its isochoric and volumetric components. This decomposition of the deformation gradient \mathbf{F} is

$$\mathbf{F} = \mathbf{F}_{\text{vol}} \cdot \mathbf{F}_{\text{iso}}, \quad (3.23)$$

where \mathbf{F}_{vol} and \mathbf{F}_{iso} are the volumetric and isochoric components respectively. The deformation gradient components are calculated as [39]

$$\mathbf{F}_{\text{vol}} = J^{1/3} \mathbf{I}, \quad \mathbf{F}_{\text{iso}} = J^{-1/3} \mathbf{F}. \quad (3.24)$$

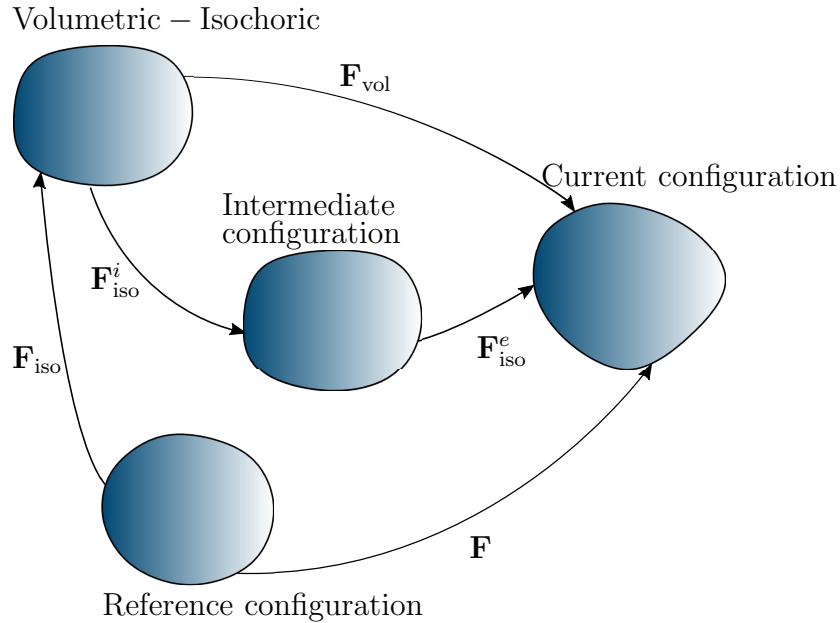


Figure 3.6: Representation of decomposed volumetric and isochoric components of deformation gradient

The elastic and inelastic components deformation gradient of equation (3.14) are enforced onto the isochoric component of the deformation gradient as represented in Figure 3.6, thus leading to

$$\mathbf{F}_{\text{iso}}^e = (\det \mathbf{F}_e)^{1/3} \mathbf{F}_e, \quad \text{and} \quad \mathbf{F}_{\text{iso}}^i = (\det \mathbf{F}_i)^{1/3} \mathbf{F}_i. \quad (3.25)$$

Consequently, the associated left Cauchy-Green deformation tensors \mathbf{B} and \mathbf{B}_e^j of j^{th} Maxwell element are formulated

$$\bar{\mathbf{B}} = J^{-2/3} \mathbf{B}, \quad \text{and} \quad \bar{\mathbf{B}}_e^j = J^{-2/3} \mathbf{B}_e^j \quad (3.26)$$

I_1 and I_3 are the first and third invariants of the Cauchy-Green deformation tensor. These invariants are calculated as follows

$$I_1 = \text{tr}(\mathbf{B}); \quad I_3 = \det(\mathbf{C}) = \det(\mathbf{B}) = J^2, \quad (3.27)$$

and the modified counterparts of the invariants are calculated as

$$\bar{I}_1 = J^{-2/3} I_1; \quad \bar{I}_3 = \det(\bar{\mathbf{C}}) = \det(\bar{\mathbf{B}}). \quad (3.28)$$

This work does not use second invariant-based material models like the Mooney-Rivlin model [105, 123]. Therefore calculation of the second invariant is not discussed.

3.3 Modelling the coupled formulation

Adhesives absorb moisture from the surrounding atmosphere because of their hygroscopic property. The moisture diffused in the material leads to a decay in the material's properties. The ageing under the influence of moisture concentration can be modelled with a coupled material model. There are well-established theories to model environmental effects like temperature [73, 74] or humidity [46, 119, 130] on the mechanical behaviour of polymers. In these theories, Fick's law of diffusion is used to evaluate the effect of humidity on viscoelastic behaviour. In this work, a finite-strain viscoelastic model is coupled with the Langmuir-type diffusion model to consider anomalous moisture

diffusion. The influence of the moisture concentration is superimposed over the mechanical behaviour by considering the moisture-dependent stiffness. The moisture-dependent stiffness parameters are formulated based on the theories proposed by Goldschmidt et al. [46] and Sharma et al. [130]

3.3.1 Constitutive theory

The constitutive equations required to describe the mechanical behaviour of the material under the influence of the additional physical conditions must establish a free energy function constituting both the mechanical and external factors. To this end, the effects of the moisture influence on the mechanical behaviour are considered under isothermal conditions. The moisture transport into the material leads to stiffness and swelling deformation decay. Here, ageing due to decay in the stiffness is accounted to establish free energy function, and the swelling deformation is not considered due to an assumption that the swelling deformation due to moisture diffusion is negligible. Thus the free energy of the coupled viscoelastic and diffusion behaviours is formulated as the sum of mechanical and diffusion parts, W_{mech} and W_m

$$W = W_{\text{mech}} \left(J, \bar{\mathbf{I}}_1^{\mathbf{B}}, \bar{\mathbf{I}}_1^{\mathbf{B}^e}, m \right) + W_m(m, m_b). \quad (3.29)$$

In contradiction to a purely incompressible formulation of the viscoelastic materials [59, 122], we employ a nearly incompressible behaviour because of small volumetric strains. Therefore, an uncoupled response is considered in the free energy function [55, 132]. The mechanical part is dependent on the moisture concentration and the free energy function is formulated as a moisture concentration dependent function [46]. A further assumption is based on the additive decomposition of the nearly incompressible viscoelastic free energy into volume-changing part W_{vol} and isochoric part (shape-changing) consisting of equilibrium part W_{eq} and the rate-dependent part of the non-equilibrium part W_{neq}^j represented by $j = 1, 2, \dots, n$ Maxwell elements as shown in Figure 3.3 [55]

$$W_{\text{mech}} \left(J, \bar{\mathbf{I}}_1^{\mathbf{B}}, \bar{\mathbf{I}}_1^{\mathbf{B}^e}, m \right) = W_{\text{vol}}(J, m) + W_{\text{eq}} \left(\bar{\mathbf{I}}_1^{\mathbf{B}}, m \right) + \sum_{j=1}^n W_{\text{neq}}^j \left(\bar{\mathbf{I}}_1^{\mathbf{B}^e}, m \right). \quad (3.30)$$

The mechanical components of the free energy defined in the equations (3.30) are substituted into the equation (3.29), leading to

$$\begin{aligned}
W = & W_{\text{vol}}(J, m) + W_{\text{eq}}\left(\bar{\mathbf{I}}_1^{\mathbf{B}}, m\right) \\
& + \sum_{j=1}^n W_{\text{neq}}^j\left(\bar{\mathbf{I}}_1^{\mathbf{B}^j}, m\right) + W_m(m, m_b).
\end{aligned} \tag{3.31}$$

The mechanical free energy is coupled with the moisture concentration by considering the material parameters as a function of moisture concentration. The equilibrium part of the free energy function is motivated by a polynomial function of the isochoric first invariant of the left Cauchy-Green deformation tensor $\bar{\mathbf{I}}_1^{\mathbf{B}}$ using the Yeoh model [157, 158]

$$W_{\text{eq}}\left(\bar{\mathbf{I}}_1^{\mathbf{B}}, m\right) = c_{10}(m)\left(\bar{\mathbf{I}}_1^{\mathbf{B}} - 3\right) + c_{20}(m)\left(\bar{\mathbf{I}}_1^{\mathbf{B}} - 3\right)^2 + c_{30}(m)\left(\bar{\mathbf{I}}_1^{\mathbf{B}} - 3\right)^3, \tag{3.32}$$

where $c_{10}(m)$, $c_{20}(m)$ and $c_{30}(m)$ are the moisture dependent material parameters. A general quadratic form is considered in current formulation [63, 22, 111, 112, 113] for the volumetric part of free energy density function

$$W_{\text{vol}}(J, m) = \frac{1}{G(m)}(J - 1)^2, \tag{3.33}$$

where $G(m)$ is the moisture-dependent compression modulus. The total non-equilibrium free energy of the Maxwell elements is computed as the sum of $j = 1, 2, \dots, n$ energies of the individual Maxwell elements

$$\sum_{j=1}^n W_{\text{neq}}^j\left(\bar{\mathbf{I}}_1^{\mathbf{B}^j}, m\right) = \sum_{j=1}^n W_{\text{neq}}^j\left(\bar{\mathbf{I}}_1^{\mathbf{B}^j}, m\right) = \sum_{j=1}^n c_{10j}(m)\left(\bar{\mathbf{I}}_1^{\mathbf{B}^j} - 3\right). \tag{3.34}$$

The constitutive quantities \mathcal{R} and the process variable \mathcal{S} are needed to model a material behaviour with an assumption that the constitutive quantities \mathcal{R} are dependent on the process variable \mathcal{S} . The process variables \mathcal{S} are

$$\mathcal{S} = \{\mathbf{B}, \mathbf{B}_e^j, m, \text{grad}m\}, \tag{3.35}$$

and the constitutive quantities \mathcal{R} are

$$\mathcal{R} = \{W, \mathbf{T}, \mathbf{q}\}. \tag{3.36}$$

The physical ageing of the adhesives is investigated under the influence of moisture concentration at an isothermal condition with no chemical ageing. The Clausius-Planck inequality is followed the equation (2.27) due the isothermal condition. The Clausius-Planck inequality is

$$\rho \dot{W} - \mathbf{T} : \mathbf{D} + \operatorname{div}(R_m \mathbf{q}) \geq 0, \quad (3.37)$$

where R_m is the chemical potential and \mathbf{q} is the moisture flux. The material time derivative of the free energy function is derived with the process variable to evaluate dissipation as

$$\begin{aligned} \dot{W} = & \frac{\partial W_{\text{vol}}(J, m)}{\partial \bar{\mathbf{B}}} : \dot{\bar{\mathbf{B}}} + \frac{\partial W_{\text{eq}}(\bar{\mathbf{I}}_1^{\bar{\mathbf{B}}}, m)}{\partial \bar{\mathbf{B}}} : \dot{\bar{\mathbf{B}}} + \\ & \sum_{j=1}^n \frac{\partial W_{\text{neq}}^j(\bar{\mathbf{I}}_1^{\bar{\mathbf{B}}_e^j}, m)}{\partial \bar{\mathbf{B}}_e^j} : \dot{\bar{\mathbf{B}}_e^j} + \frac{\partial W_m(m, m_b)}{\partial m} : \dot{m}. \end{aligned} \quad (3.38)$$

From the established relationship between the deformation tensors \mathbf{B} and \mathbf{B}_e^j with the deformation velocity \mathbf{D} , the time derivatives of the deformation tensors are formulated as

$$\dot{\mathbf{B}} = 2\mathbf{D} \cdot \mathbf{B} \quad \text{and} \quad \dot{\mathbf{B}}_e^j = 2\mathbf{D} \cdot \mathbf{B}_e^j - 2\mathbf{F}_e^j \cdot \overset{\Delta}{\Gamma}_i^j \cdot (\mathbf{F}_e^j)^T, \quad (3.39)$$

where the inelastic deformation rate of the intermediate configuration $\overset{\Delta}{\Gamma}_i^j$ is an outcome of applying the product rule over $\dot{\mathbf{B}}_e^j$. After inserting the material time derivative of free energy (3.38) and the time derivatives of the deformation tensor leads to the Clausius-Planck inequality as

$$\begin{aligned} & \left(-2\rho \mathbf{B} \cdot \frac{\partial W_{\text{vol}}}{\partial \mathbf{B}} - 2\rho \mathbf{B} \cdot \frac{\partial W_{\text{eq}}}{\partial \mathbf{B}} - \sum_{j=1}^n 2\rho \bar{\mathbf{B}}_e^j \cdot \frac{\partial W_{\text{neq}}}{\partial \bar{\mathbf{B}}_e^j} + \mathbf{T} \right) : \mathbf{D} \\ & + \sum_{j=1}^n 2\rho \frac{\partial W_{\text{neq}}}{\partial \bar{\mathbf{B}}_e^j} : \left(\mathbf{F}_e^j \cdot \overset{\Delta}{\Gamma}_i^j \cdot (\mathbf{F}_e^j)^T \right) + \left(-\rho \frac{\partial W_m(m, m_b)}{\partial m} + R_m \right) \cdot \dot{m} \\ & - \operatorname{grad} R_m \cdot \mathbf{q} \geq 0. \end{aligned} \quad (3.40)$$

The entropy inequality condition in equation (3.40) depends linearly on the independent variables \mathbf{D} , \dot{m} . The entropy inequality is evaluated based on Coleman and Noll [28] leading to constitutive relation for the Cauchy stress

$$\mathbf{T} = 2\rho \mathbf{B} \cdot \frac{\partial W_{\text{vol}}(J, m)}{\partial \mathbf{B}} + 2\rho \mathbf{B} \cdot \frac{\partial W_{\text{eq}}(\bar{\mathbf{I}}_1^{\bar{\mathbf{B}}}, m)}{\partial \mathbf{B}} + \sum_{j=1}^n 2\rho \bar{\mathbf{B}}_e^j \cdot \frac{\partial W_{\text{neq}}^j(\bar{\mathbf{I}}_1^{\bar{\mathbf{B}}_e^j}, m)}{\partial \bar{\mathbf{B}}_e^j}, \quad (3.41)$$

the first term corresponds to the volumetric stress component analogous to the hydrostatic component, and the other two terms corresponds to the equilibrium and non-equilibrium parts. Applying the chain rule to the volumetric stress component with the relationship $\partial J/\partial \mathbf{B} = J\mathbf{B}^{-1}$ and free energy of the volumetric part and the isochoric parts of the equilibrium and the non-equilibrium parts are assumed to be $W_{(\bullet)} = \rho W_{(\bullet)}$ [55] leads to

$$\mathbf{T} = JW'_{\text{vol}}(J, m)\mathbf{I} + 2\mathbf{B} \cdot \frac{\partial W_{\text{eq}}(\mathbf{I}_1^{\mathbf{B}}, m)}{\partial \mathbf{B}} + \sum_{j=1}^n 2\bar{\mathbf{B}}_e^j \cdot \frac{\partial W_{\text{neq}}^j(\mathbf{I}_1^{\mathbf{B}_e^j}, m)}{\partial \bar{\mathbf{B}}_e^j}, \quad (3.42)$$

where $W'_{\text{vol}} = \partial W_{\text{vol}}/\partial J$ is the hydrostatic pressure component [132]. The third term of the equation (3.40) leads to the definition of the chemical potential

$$R_m = \rho \frac{\partial W_m(m, m_b)}{\partial m}, \quad (3.43)$$

and the dissipation inequality is simplified to

$$\sum_{j=1}^n 2\rho \frac{\partial W_{\text{neq}}^j(\mathbf{I}_1^{\mathbf{B}_e^j}, m)}{\partial \bar{\mathbf{B}}_e^j} : \left(\mathbf{F}_e^j \cdot \overset{\Delta}{\Gamma}_i^j \cdot (\mathbf{F}_e^j)^T \right) - \text{grad} R_m \cdot \mathbf{q} \geq 0. \quad (3.44)$$

The first term of the dissipation inequality of equation (3.44) is used to derive the evolution equation of the right Cauchy-Green deformation. After some mathematical calculations and using the kinematic relations of finite deformation discussed in section 3.2 leads to [56, 90, 128]

$$\dot{\bar{\mathbf{C}}}_i^j = \frac{4}{r_j} \left[\bar{\mathbf{C}} - \frac{1}{3} \text{tr} \left(\bar{\mathbf{C}} \cdot (\bar{\mathbf{C}}_i^j)^{-1} \right) \bar{\mathbf{C}}_i^j \right] \quad (3.45)$$

where r_j is the relaxation time associated with the dashpot of the j^{th} Maxwell element. The relaxation times are the material constants computed as

$$r_j = \frac{\mu_{10n}}{\eta_n}. \quad (3.46)$$

The second term is characterised by the diffusive flux to ensure the positivity of the simplified dissipation inequality

$$\mathbf{q} = -D(\text{grad} R_m), \quad (3.47)$$

where D is the diffusion coefficient. Free energy of the moisture diffusion $W_m(m, m_b)$ is considered as

$$W_m(m, m_b) = \frac{1}{2} (m - m_b)^2, \quad (3.48)$$

where m_b is the immobile moisture concentration and the chemical potential of diffusive free energy is derived from the equations (3.43) and (3.48)

$$R_m = \frac{\partial W_m(m, m_b)}{\partial m} = m - m_b. \quad (3.49)$$

From equations (3.47), (3.49) and the balance of mass [16, 56, 63, 85] leads to the diffusion equation

$$\frac{dm}{dt} = D \operatorname{div} (\operatorname{grad} (m - m_b)). \quad (3.50)$$

The evaluation of the diffusion equation is discussed earlier in section 3.1.

3.3.2 Influence of moisture on viscoelastic properties

The material softens under the moisture influence, causing the material's stiffness to decay without applying any external mechanical loads on the material [53, 68, 139]. Interpolating material parameters evaluate the dependency of the material parameters on the moisture at the extreme states of the material, i.e., dry and saturated states. The interpolation of parameters is followed by [130]

$$\mu(m) = f(m)\mu^{\text{dry}} + (1 - f(m))\mu^{\text{sat}}. \quad (3.51)$$

$\mu(m)$ is the interpolated stiffness parameters of the viscoelastic material model. μ^{dry} and μ^{sat} are the viscoelastic parameters of dry and saturated material. In contrast, the relaxation times of the coupled material model are kept constant analogous to the thermo-viscoelastic behaviour proposed by Johlitz et al. [47, 73] as this assumption gives the advantage to fit the loading rates used in the experiments with the relaxation times of the material model. $f(m)$ is a decay function to interpolate the material parameters at the integration points.

The decay function $f(m) : [0, 1] \rightarrow [1, 0]$ plays a crucial role in coupling the viscoelastic behaviour with the moisture diffusion. To be precise, it determines the decay in the viscoelastic material parameters under the influence of the local moisture concentration. Therefore, the decay function should satisfy certain conditions as follows

- $f(m)$ has to be a monotonically decay function;
- for the local moisture concentration interval $0 \leq m \leq m_\infty(H)$, the value of the decay function must lie between the interval $1 \leq f(m) \lesssim 0$;
- $f(m = 0) = 1$ defines the dry state and $f(m = m_\infty(H)) \approx 0$ defines the saturated state of the material at $H\%$ humid climatic condition.

The material parameters of the aged samples were used to identify the interpolation function. Goldschmidt et al. [46] investigated the ageing of polyurethane adhesives under the influence of moisture by considering a power law to consider the decay in stiffness parameters. However, the current work uses an exponential function as the power law function decays more slowly and is not differentiable at zero. An exponential decay function is advantageous in calculating physically admissible stiffness parameters under the moisture influence. The order and coefficients of the exponential decay function are identified by fitting the experimental data with the curve.

3.3.3 Governing equation

The Langmuir-type diffusion discussed in section 3.1 is coupled with the finite-strain viscoelastic behaviour to analyse the ageing process. The coupled material model considers moisture-dependent stiffness parameters due to the decay of stresses \mathbf{T} . As a result, the balance of momentum follows

$$\operatorname{div}(\mathbf{T}(\bar{\mathbf{B}}, \bar{\mathbf{B}}_e^j, J, m)) = \mathbf{0}. \quad (3.52)$$

The constitutive equation of Cauchy stress $\mathbf{T}(\bar{\mathbf{B}}, \bar{\mathbf{B}}_e^j, J, m)$ is defined in equation (3.42). The moisture diffusion is modelled with the Langmuir-type diffusion model as outlined in section 3.1. The governing equation to model anomalous moisture diffusion is

$$\dot{m} = D \Delta m_f = D \operatorname{div}(\operatorname{grad}(m - m_b)), \quad (3.53)$$

where the immobile moisture concentration is evaluated with

$$\dot{m}_b = \alpha m - (\alpha + \beta) m_b. \quad (3.54)$$

3.3.4 Boundary conditions

The field variables of the coupled system of equations are the displacement field variable \mathbf{u} and the moisture concentration field m , respectively. It is necessary to define the boundary conditions to solve the coupled equations discussed in section 3.3.3. Accordingly, the surface $\partial\Omega$ is decomposed according to the field variables displacement \mathbf{u} and moisture concentration m

$$\partial\Omega = \partial\Omega_{\mathbf{u}}^D \cup \partial\Omega_{\mathbf{t}}^N \text{ and } \partial\Omega = \partial\Omega_m^D \cup \partial\Omega_{\mathbf{q}}^N \quad (3.55)$$

with $\partial\Omega_{\mathbf{u}}^D \cap \partial\Omega_{\mathbf{t}}^N = \emptyset$ and $\partial\Omega_m^D \cap \partial\Omega_{\mathbf{q}}^N = \emptyset$. The Dirichlet and Neumann boundary conditions concerning the mechanical problem are postulated to relate to the displacement and traction field

$$\mathbf{u}(\mathbf{x}, t) = \mathbf{u}_D(\mathbf{x}, t) \text{ on } \partial\Omega_{\mathbf{u}}^D \text{ and } \mathbf{T} \cdot \mathbf{n} = \mathbf{t} \text{ on } \partial\Omega_{\mathbf{t}}^N, \quad (3.56)$$

where \mathbf{t} is the traction on the surface $\partial\Omega_{\mathbf{t}}^N$ with the normal vector \mathbf{n} . The Dirichlet and Neumann boundary conditions are postulated for the moisture diffusion problem, as discussed in section 3.1. The Dirichlet boundary conditions are given as

$$m(\mathbf{x}, t) = m_D \forall \mathbf{x} \in \partial\Omega_m^D \quad (3.57)$$

and the Neumann boundary conditions are given as

$$\mathbf{q} \cdot \mathbf{n} = D(\text{grad } m_f) \cdot \mathbf{n} = q(\mathbf{x}, t) \forall \mathbf{x} \in \partial\Omega_{\mathbf{q}}^N. \quad (3.58)$$

4

Phase-field modelling of fracture

Modelling of crack propagation is an existing challenge in polymer materials [49, 152]. In this context, the crack propagation is well understood within the framework of theoretical continuum mechanics [81]. The energy balance at the crack propagation boundary is described based on Griffith's criterion. Griffith's theory states that a crack propagates when the energy release rate at the crack propagation zone is higher than the surface energy built up. The conventional method in modelling crack separates the material into a broken and intact material by an interface. However, such a method requires a priori knowledge of the exact position of the interface and is complex to model in three-dimensional systems. Therefore, the phase-field method is developed to have a decisive advantage over sharp interface models since the explicit interface tracking becomes redundant [108].

A distinction is made between physical and mechanical approaches in modelling the phase-field material models. The physical model approaches are based on the Ginzburg-Landau phase transformation. In contrast, the mechanical approaches are based on Griffith's failure theory. A review of the different approaches in modelling phase-field ductile fracture is detailed by Ambati et al. [4]. These models use order parameters to distinguish broken and intact material by minimising the system's free energy [78]. Phase-field

fracture models describe crack propagation in homogeneous materials under different loads [19, 82, 103], including plastic effects [4, 62, 35, 3] and multi-physics problems [100, 102, 136]. Based on Griffith's theory, a model with position-dependent crack resistance was presented by Hossain et al. [65] for studies of fracture strength in materials.

4.1 Fundamentals of fracture

This section summarises the failure modes based on fracture mechanics. Well-documented literature is recommended for the detailed introduction to fracture mechanics [110, 115]. In macroscopic point of view, the crack is propagated in the material by forming a new surface at the interface region. The opposite surfaces of the crack are called crack flanks and the crack end is called crack tip. The deformation of a crack is divided into three independent modes, as shown in Figure 4.1. Mode I is critical in most engineering applications caused due to the orthogonal opening of two crack flanks under a tensile load. The Mode II failure is due to the sliding of crack flanks against each other in the crack plane under shear load. Mode III is generated by loads transverse to the crack flanks and causes lateral shear.

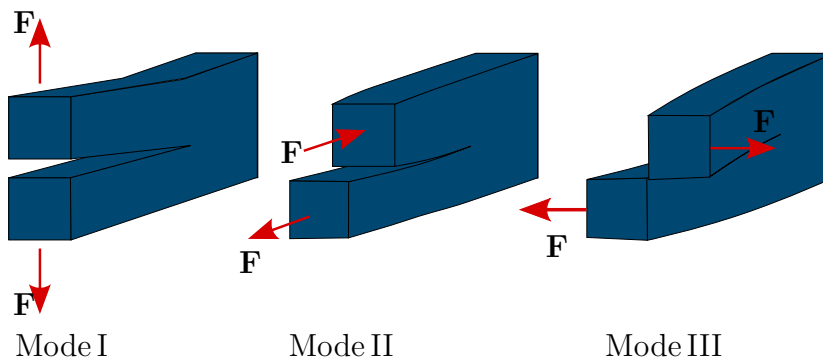


Figure 4.1: The three basic types of failures in fracture mechanics [52]

The motivation of the current work is to investigate the tear strength of the adhesive samples aged under the moisture influence. Tear tests to investigate fracture toughness on the adhesive samples are prepared based on the DIN ISO 34-1 standard. The angular sample is chosen to examine the tear strength of adhesive samples under tensile loading conditions.

4.2 Griffiths's theory of failure

Griffith was the first to study the energy balance in the case of crack propagation [51]. Griffith's studies state that the energy released during crack propagation and the energy required to form a new surface must be balanced. Griffith's energy balance considers a crack propagation ΔA in a two-dimensional body with unit depth. The energy release rate E_c is defined as the differential of the potential energy to the infinitesimally small crack propagation

$$E_c = \lim_{\Delta A \rightarrow 0} -\frac{\Delta \Pi}{\Delta A} = -\frac{\partial \Pi}{\partial A}. \quad (4.1)$$

In a purely elastic case, the internal energy Π is called as the strain energy E . The crack propagates when the critical energy release rate E_c exceeds the material-specific crack resistance, and the fracture criterion is followed by

$$E - E_c \leq 0. \quad (4.2)$$

Griffith's criterion for fracture [51] is established in linear fracture mechanics that is equivalent to the stress intensity criterion for crack propagation [69]. The crack surface energy Γ proportional to the crack area A results in

$$E_c = \frac{\partial \Gamma}{\partial A}. \quad (4.3)$$

4.3 Modelling phase-field fracture model

The fracture in the polyurethane adhesives is modelled using a finite-strain phase-field theory without considering the influence of the moisture on the fracture behaviour at an isothermal condition. The basic idea behind the variational formulation of the phase-field fracture model is to minimise the total free energy by obeying a kinematically admissible displacement field. The total free energy W of the coupled formulation takes the form

$$W \left(\bar{\mathbf{I}}_1^{\mathbf{B}}, \bar{\mathbf{I}}_1^{\mathbf{B}^e}, J, \phi \right) = W_b \left(\bar{\mathbf{I}}_1^{\mathbf{B}}, \bar{\mathbf{I}}_1^{\mathbf{B}^e}, J, \phi \right) + W_s(\phi). \quad (4.4)$$

The first term $W_b(\bar{\mathbf{I}}_1^{\mathbf{B}}, \bar{\mathbf{I}}_1^{\mathbf{B}^j}, J, \phi)$ is the bulk energy and the second term $W_s(\phi)$ is the surface energy of a propagating crack. The associated field variables are the displacement $\mathbf{u}(\mathbf{x}, t)$ and the phase-field variable $\phi(\mathbf{x}, t)$. The solid domain $\Omega \subset \mathbb{R}^3$ in the reference configuration of the material body is defined in three dimensions in space. These field variables are also studied in the temporal domain in the range of time $T \subset \mathbb{R}$. Consequently, the time-dependent phase-field variable $\phi(\mathbf{x}, t)$ is introduced in a spatial domain

$$\phi = \begin{cases} \Omega \times T \rightarrow [0, 1] \\ (\mathbf{x}, t) \rightarrow \phi(\mathbf{x}, t), \end{cases} \quad (4.5)$$

and the corresponding displacement field $\mathbf{u}(\mathbf{x}, t)$ in time for the applied increment of load in the spatial domain is defined as

$$\mathbf{u} = \begin{cases} \Omega \times T \rightarrow \mathbb{R}^3 \\ (\mathbf{x}, t) \rightarrow \mathbf{u}(\mathbf{x}, t), \end{cases} \quad (4.6)$$

and calculated using the equation (2.4). Based on a well-known Griffith energy balance, the surface energy is

$$W_s(\phi) = \int_{\Gamma} E_c d\Gamma, \quad (4.7)$$

where E_c is the critical energy release rate. The solution to this problem is not possible with the existing mathematical relationships since the crack area Γ is an unknown entity. Therefore, the crack area Γ is regularised using the crack surface density function $\gamma(\phi, \text{grad } \phi)$ leading to the volumetric integral of the surface energy density functional

$$W_s(\phi) = \int_{\Omega} E_c \gamma(\phi, \text{grad } \phi) dV. \quad (4.8)$$

4.3.1 Regularization of the crack surface density function

The primary concern of the phase-field fracture model is to regularise the crack surface by a diffusive smeared crack within the localised band of a finite length controlled by the length-scale parameter ℓ_f . This section summarises the regularisation of the crack surface by considering a 1D crack problem of

the constant cross-sectional area of Γ . The sharp crack on the cross-section is indicated with a variable $\phi(\mathbf{x}) \in [0, 1]$, in which the material is characterised by indicating $\phi(\mathbf{x}) = 0$ as the broken state and $\phi(\mathbf{x}) = 1$ as the intact state. The phase-field crack (4.5) is approximated using an exponential function

$$\phi(\mathbf{x}) = 1 - \exp\left(-\frac{|\mathbf{x}|}{\ell_f}\right), \quad (4.9)$$

as illustrated by the diffusive crack topology shown in Figure 4.2_b.

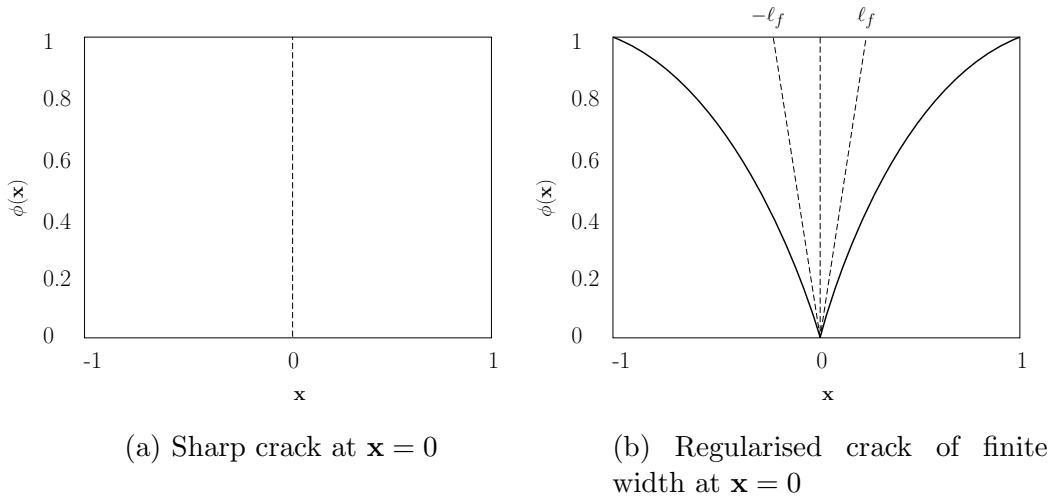


Figure 4.2: Modelling sharp crack at $\mathbf{x} = 0$ (left) and a regularised diffusive crack (right) obtained from the minimisation of the crack topology, which is controlled by the length scale parameter ℓ_f .

The length-scale parameter ℓ_f governs the width of the diffusive crack, and the value of the exponential function (4.9) equates to the values phase-field variable defined in equation (4.5) for $\ell_f \rightarrow 0$. The exponential function (4.9) is a monotonically decreasing function and implies that the equation (4.9) is a solution for the ordinary differential equation [24]

$$\phi''(\mathbf{x}) - \frac{1}{\ell_f^2} (1 - \phi(\mathbf{x})) = 0 \quad \text{in } \Omega, \quad (4.10)$$

where $(\bullet)'$ and $(\bullet)''$ are the first and second order derivatives, $\partial(\bullet)/\partial\mathbf{x}$ and $\partial^2(\bullet)/\partial\mathbf{x}^2$. The derivatives of the exponential function are

$$\begin{aligned}\phi'(\mathbf{x}) &= -\frac{\operatorname{sgn}(\mathbf{x})}{\ell_f} e^{-\frac{|\mathbf{x}|}{\ell_f}} \\ \phi''(\mathbf{x}) &= \left[\frac{\operatorname{sgn}(\mathbf{x})}{\ell_f} \right]^2 e^{-\frac{|\mathbf{x}|}{\ell_f}} = \frac{1}{\ell_f^2} e^{-\frac{|\mathbf{x}|}{\ell_f}} = \frac{1}{\ell_f^2} \phi(\mathbf{x}).\end{aligned}\quad (4.11)$$

The differential equation (4.10) applied with the boundary condition \mathcal{F} results in the Euler Lagrange equation of the variation principle [103, 19]

$$\phi = \arg \left\{ \inf_{\phi \in \mathcal{F}} \Pi(\phi) \right\} \quad \text{with } \mathcal{F} = \{\phi(0) = 0, \phi(\pm\infty) = 1\}, \quad (4.12)$$

and the function $\Pi(\phi)$ is expressed as

$$\Pi(\phi) = \int_{-\infty}^{\infty} \frac{1}{2} [(1 - \phi)^2 + \ell_f^2 (\phi')^2] dV. \quad (4.13)$$

$\Pi(\phi)$ is a simple construct of the integral for the Galerkin-type weak form of equation (4.10) [103]. The exponential function (4.9) is substituted in equation (4.13) and integrated over the volume to build relationship between Π and the crack surface Γ as

$$\Pi(\phi) = \ell_f \Gamma(\phi). \quad (4.14)$$

The crack surface density is introduced with the regularised crack functional $\gamma(\phi, \operatorname{grad} \phi)$ by evaluating the equations (4.13) and (4.14)

$$\begin{aligned}\Gamma(\phi) &= \frac{1}{\ell_f} \Pi(\phi) = \int_{\Omega} \left[\frac{1}{2\ell_f} (1 - \phi)^2 + \frac{\ell_f}{2} |\operatorname{grad} \phi|^2 \right] dV \\ &= \int_{\Omega} \gamma(\phi, \operatorname{grad} \phi) dV.\end{aligned}\quad (4.15)$$

4.3.2 Degradation of the bulk energy

The bulk energy is the stored mechanical energy and degrades as the crack propagates. The degradation in the mechanical energy is formulated by multiplying the free energy $W_0 \left(\bar{\mathbf{I}}_1^{\mathbf{B}}, \bar{\mathbf{I}}_1^{\mathbf{B}^e}, J \right)$ of the intact material with the degra-

gradation function $g(\phi)$

$$W_b \left(\bar{\mathbb{I}}_1^{\bar{\mathbf{B}}}, \bar{\mathbb{I}}_1^{\bar{\mathbf{B}}^e}, J, \phi \right) = g(\phi) W_0 \left(\bar{\mathbb{I}}_1^{\bar{\mathbf{B}}}, \bar{\mathbb{I}}_1^{\bar{\mathbf{B}}^e}, J \right). \quad (4.16)$$

The degradation of the bulk energy defined in the equation (4.16) needs to satisfy the necessary conditions of the intact and broken material for the value of the phase-field variable $\phi \in [0, 1]$

$$\begin{aligned} W_b \left(\bar{\mathbb{I}}_1^{\bar{\mathbf{B}}}, \bar{\mathbb{I}}_1^{\bar{\mathbf{B}}^e}, J, \phi = 1 \right) &= W_0 \left(\bar{\mathbb{I}}_1^{\bar{\mathbf{B}}}, \bar{\mathbb{I}}_1^{\bar{\mathbf{B}}^e}, J \right), \quad W_b \left(\bar{\mathbb{I}}_1^{\bar{\mathbf{B}}}, \bar{\mathbb{I}}_1^{\bar{\mathbf{B}}^e}, J, \phi = 0 \right) = 0, \\ \partial W_b \left(\bar{\mathbb{I}}_1^{\bar{\mathbf{B}}}, \bar{\mathbb{I}}_1^{\bar{\mathbf{B}}^e}, J, \phi \right) &< 1 \quad \text{and} \quad \partial W_b \left(\bar{\mathbb{I}}_1^{\bar{\mathbf{B}}}, \bar{\mathbb{I}}_1^{\bar{\mathbf{B}}^e}, J, \phi = 0 \right) = 0. \end{aligned} \quad (4.17)$$

The equations (4.8), (4.15) and (4.16) are substituted in the equation (4.4) and integrated over the volume to derive the free energy density [19, 40]

$$\begin{aligned} W \left(\bar{\mathbb{I}}_1^{\bar{\mathbf{B}}}, \bar{\mathbb{I}}_1^{\bar{\mathbf{B}}^e}, J, \phi \right) &= \int_{\Omega} g(\phi) W_0 \left(\bar{\mathbb{I}}_1^{\bar{\mathbf{B}}}, \bar{\mathbb{I}}_1^{\bar{\mathbf{B}}^e}, J \right) dV + \\ &\int_{\Omega} E_c \left[\frac{1}{2\ell_f} (1 - \phi)^2 + \frac{\ell_f}{2} |\text{grad } \phi|^2 \right] dV. \end{aligned} \quad (4.18)$$

4.3.3 Degradation function

The energy degradation function $g(\phi)$ plays a vital role in interpolating stresses due to changes in unbroken to broken states at the transition zone. The degradation function influences changes in material parameters between intact and broken states. This function also establishes the coupling between the viscoelastic energy and the evolution equation for damage. The chosen degradation function $g(\phi)$ must satisfy the following conditions

- $g(\phi = 1) = 1$ defining the intact material and $g(\phi = 0) = 0$ defining the broken material;
- $g'(\phi) = \partial g(\phi) / \partial \phi < 1$ as $g(\phi)$ is a monotonically decreasing function, and the derivative must be continuously differentiable;
- $g'(0) = 0$ controls the contribution of the stored material energy by eliminating the viscoelastic energy function W_0 when $g(\phi = 0) = 0$ in the evolution of the phase-field crack functional, see equation (4.40b).

A classical second-order degradation function is considered in the degradation of the bulk energy. This function takes into account for an additional regularization parameter ζ [18, 60, 84]

$$g(\phi) = (1 - \zeta)\phi^2 + \zeta. \quad (4.19)$$

The regularisation parameter $\zeta > 0$ is employed to regularise the bulk energy to guarantee a converged solution. The parameter $\zeta > 0$ must be small to avoid overestimating mechanical energy and underestimating the crack energy of the phase-field evolution equation [17, 18, 21].

4.4 Thermodynamic consistency

The work performed on the body can be partitioned into a mechanical contribution and a contribution by the micro force system characterised by the micro stress vector and the internal and external micro forces that lead to the tearing of the material. As a result, the virtual power takes the form

$$\dot{\mathcal{E}} = \mathcal{P}_{\text{mech}} + \mathcal{P}_{\text{mic}}, \quad (4.20)$$

where $\dot{\mathcal{E}}$ corresponds to the total power, $\mathcal{P}_{\text{mech}}$ denotes the mechanical power and \mathcal{P}_{mic} denotes the power of the micro force system. The virtual power of the system for the considered generalised virtual velocity $\mathcal{V} = \{\dot{\mathbf{u}}, \dot{\phi}\}$ is

$$\begin{aligned} & \int_{\Omega} \mathbf{T} : \text{grad} \dot{\mathbf{u}} \, dV + \int_{\Omega} \boldsymbol{\omega} \cdot \text{grad} \dot{\phi} \, dV + \int_{\Omega} \varsigma \dot{\phi} \, dV = \\ & \int_{\partial\Omega} \mathbf{t} \cdot \dot{\mathbf{u}} \, dA + \int_{\Omega} \mathbf{b} \cdot \dot{\mathbf{u}} \, dV + \int_{\partial\Omega} \chi \dot{\phi} \, dA + \int_{\Omega} \Upsilon \dot{\phi} \, dV, \end{aligned} \quad (4.21)$$

where \mathbf{T} is the Cauchy stress tensor, $\mathbf{t} = \mathbf{T} \cdot \mathbf{n}$ is traction, and \mathbf{b} is the external body force acting on the system. The components of the micro force system are the microscopic stress $\boldsymbol{\omega}$ power-conjugate to $\text{grad} \dot{\phi}$, microscopic internal force ς , external traction χ and the external microscopic force Υ are the power-conjugate to $\dot{\phi}$.

By applying the virtual velocity $\mathcal{V} = (\dot{\mathbf{u}}, 0)$ over the equation (4.21) leads to

the balance equation of momentum

$$\operatorname{div} \mathbf{T} + \mathbf{b} = 0. \quad (4.22)$$

By considering the virtual velocity $\mathcal{V} = (0, \dot{\phi})$ leads to the phase-field equation

$$\operatorname{div} \boldsymbol{\omega} - \varsigma + \Upsilon = 0 \quad (4.23)$$

after applying the divergence theorem, the microscopic traction is computed as $\chi = \boldsymbol{\omega} \cdot \mathbf{n}$.

4.4.1 Material theory

The entropy inequality (Clausius-Duhem inequality) is required to formulate a thermodynamically consistent material law. The details of the thermodynamic evaluation of phase-field damage are complex due to the many terms involved. However, constitutive equations need to postulate to a material model and build relations between the kinematics and the balance equations. By assuming the Clausius-Duhem inequality as a condition for a non-negative entropy, the following inequality is obtained for an isothermal condition based on the micro force system [42, 43, 54]

$$\mathbf{T} : \mathbf{D} + \boldsymbol{\omega} \cdot \operatorname{grad} \dot{\phi} + \varsigma \dot{\phi} - \dot{W} \geq 0, \quad (4.24)$$

where \dot{W} denotes the rate of the free energy function. The free energy density of the phase-field damage model is given by the sum of the mechanical and the regularised fracture energy

$$W \left(J, \bar{\mathbf{I}}_1^{\mathbf{B}}, \bar{\mathbf{I}}_1^{\mathbf{B}^e}, \phi, \operatorname{grad} \phi \right) = W_b \left(J, \bar{\mathbf{I}}_1^{\mathbf{B}}, \bar{\mathbf{I}}_1^{\mathbf{B}^e}, \phi \right) + W_\phi(\phi, \operatorname{grad} \phi), \quad (4.25)$$

where the mechanical free energy function W_b corresponds to the nearly incompressible viscoelasticity under large deformations. The free energy function of the finite-strain viscoelasticity is formulated as the algebraic sum of the volume-changing part W_{vol} and the isochoric parts consisting of the equilibrium W_{eq} and the non-equilibrium W_{neq}^j components [55]. The non-equilibrium represents the overstresses due to rate-dependent properties represented by $j = 1, 2, \dots, n$ Maxwell elements. The mechanical free energy is a function of the damage variable as discussed in chapter 4.3.2, and the free

energy function is formulated as

$$W_{\text{mech}} \left(J, \bar{\mathbf{I}}_1^{\mathbf{B}}, \bar{\mathbf{I}}_1^{\mathbf{B}_e^j}, \phi \right) = W_{\text{vol}}(J, \phi) + W_{\text{eq}} \left(\bar{\mathbf{I}}_1^{\mathbf{B}}, \phi \right) + \sum_{j=1}^n W_{\text{neq}}^j \left(\bar{\mathbf{I}}_1^{\mathbf{B}_e^j}, \phi \right). \quad (4.26)$$

As a result of inserting the equation (4.26) in equation (4.25), the energy function is expressed as

$$\begin{aligned} W \left(J, \bar{\mathbf{I}}_1^{\mathbf{B}}, \bar{\mathbf{I}}_1^{\mathbf{B}_e^j}, \phi, \text{grad} \phi \right) = & W_{\text{vol}}(J, \phi) + W_{\text{eq}} \left(\bar{\mathbf{I}}_1^{\mathbf{B}}, \phi \right) \\ & + \sum_{j=1}^n W_{\text{neq}}^j \left(\bar{\mathbf{I}}_1^{\mathbf{B}_e^j}, \phi \right) + W_{\phi}(\phi, \text{grad} \phi). \end{aligned} \quad (4.27)$$

The process variables to evaluate the inequality are (4.24)

$$\mathcal{S} = \{ \mathbf{B}, \mathbf{B}_e^j, \phi, \text{grad} \phi \}. \quad (4.28)$$

The time derivative of the free energy function \dot{W} derived with the process variables to express Clausius-Duhem inequality yields

$$\begin{aligned} \dot{W} = & \frac{\partial W_{\text{vol}}(J, \phi)}{\partial \mathbf{B}} : \dot{\mathbf{B}} + \frac{\partial W_{\text{eq}}(\bar{\mathbf{I}}_1^{\mathbf{B}}, \phi)}{\partial \mathbf{B}} : \dot{\mathbf{B}} + \sum_{j=1}^n \frac{\partial W_{\text{neq}}^j(\bar{\mathbf{I}}_1^{\mathbf{B}_e^j}, \phi)}{\partial \mathbf{B}_e^j} : \dot{\mathbf{B}}_e^j \\ & + \frac{\partial W}{\partial \phi} : \dot{\phi} + \frac{\partial W}{\partial \text{grad} \phi} : \text{grad} \dot{\phi}, \end{aligned} \quad (4.29)$$

and the equation (4.29) is applied to the inequality (4.24) leading to the simplified form

$$\begin{aligned} & \left(-2\rho \mathbf{B} \cdot \frac{\partial W_{\text{vol}}}{\partial \mathbf{B}} - 2\rho \mathbf{B} \cdot \frac{\partial W_{\text{eq}}}{\partial \mathbf{B}} - \sum_{j=1}^n 2\rho \bar{\mathbf{B}}_e^j \cdot \frac{\partial W_{\text{neq}}}{\partial \bar{\mathbf{B}}_e^j} + \mathbf{T} \right) : \mathbf{D} \\ & + \sum_{j=1}^n 2\rho \frac{\partial W_{\text{neq}}}{\partial \bar{\mathbf{B}}_e^j} : \left(\mathbf{F}_e^j \cdot \overset{\Delta}{\Gamma}_i^j \cdot (\mathbf{F}_e^j)^T \right) + \left(\varsigma - \frac{\partial W}{\partial \phi} \right) \cdot \dot{\phi} \\ & + \left(\omega - \frac{\partial W}{\partial \text{grad} \phi} \right) \cdot \text{grad} \dot{\phi} \geq 0. \end{aligned} \quad (4.30)$$

Based on the argumentation of Coleman & Noll, the first term of the inequality leads to the constitutive equation for the stress tensor by introducing an assumption $W_{(\bullet)} = \rho W_{(\bullet)}$ [55] for the free energy of the volumetric part and

the isochoric parts of the equilibrium and the non-equilibrium parts

$$\mathbf{T} = 2\mathbf{B} \cdot \frac{\partial W_{\text{vol}}}{\partial \mathbf{B}} + 2\mathbf{B} \cdot \frac{\partial W_{\text{eq}}}{\partial \mathbf{B}} + \sum_{j=1}^n 2\bar{\mathbf{B}}_e^j \cdot \frac{\partial W_{\text{neq}}}{\partial \bar{\mathbf{B}}_e^j}. \quad (4.31)$$

The remaining inequality function leads to the residual dissipation equations concerning the evolution equations for the inelastic deformation rates of n Maxwell elements [128, 90]

$$\sum_{j=1}^n 2\rho \frac{\partial W_{\text{neq}}}{\partial \bar{\mathbf{B}}_e^j} : \left(\mathbf{F}_e^j \cdot \overset{\Delta}{\Gamma}_i^j \cdot (\mathbf{F}_e^j)^T \right) \geq 0, \quad (4.32)$$

further applying the inequality condition over the group of terms leads to

$$\left(\varsigma - \frac{\partial W}{\partial \phi} \right) \cdot \dot{\phi} + \left(\omega - \frac{\partial W}{\partial \text{grad} \phi} \right) \cdot \text{grad} \dot{\phi} \geq 0 \quad (4.33)$$

and the consequent constitutive equations of the microscopic phase-field equation follows

$$\omega = \frac{\partial W_\phi(\phi, \text{grad} \phi)}{\partial \phi}, \quad \varsigma = \frac{\partial W_\phi(\phi, \text{grad} \phi)}{\partial \text{grad} \phi}. \quad (4.34)$$

Finally, the constitutive equations (4.34) are substituted in the equation (4.23) to obtain the phase-field equation

$$\text{div} \left(\frac{\partial W_\phi(\phi, \text{grad} \phi)}{\partial \text{grad} \phi} \right) - \frac{\partial W_\phi(\phi, \text{grad} \phi)}{\partial \phi} = 0. \quad (4.35)$$

Based on the micro force balance law, Gurtin [54] proposed the general form of evolution for the damage order parameter ϕ consistent with the equation (4.34) takes the form

$$\dot{\phi} = -M \left(W - E_c \left(\ell_f \text{div} \phi - \frac{1}{\ell_f} (1 - \phi) \right) \right), \quad (4.36)$$

where $M > 0$ is a scalar mobility parameter. An assumption of a constant mobility parameter leads to the regularised crack surface density function discussed in section 4.3.1

4.5 Governing balance equations

The weak form of the free energy function is derived by applying the variational principle to the total potential energy and is derived as the partial derivative of the total free energy with the field variables (\mathbf{u}, ϕ)

$$\delta W = \left(\frac{\partial W}{\partial \mathbf{u}} \right) : \delta \mathbf{u} + \left(\frac{\partial W}{\partial \phi} \right) : \delta \phi. \quad (4.37)$$

Furthermore, the continuum domain Ω is integrated over the total volume dV leading to the weak form of the coupled formulation for the admissible test functions of phase-field $\delta \phi$ and displacement field $\delta \mathbf{u}$

$$\begin{aligned} \delta W = & \int_{\Omega} \{g(\phi) \mathbf{T} : \text{grad}^s \delta \mathbf{u} + g'(\phi) \delta \phi W_0\} dV + \\ & \int_{\Omega} \left\{ E_c \left[-\frac{1}{\ell_f} (1 - \phi) \delta \phi + \ell_f \text{grad} \phi \text{grad} \delta \phi \right] \right\} dV, \end{aligned} \quad (4.38)$$

$\text{grad}^s \delta \mathbf{u} = \frac{1}{2} [\text{grad} \delta \mathbf{u} + (\text{grad} \delta \mathbf{u})^T]$ is involved due to symmetric stress tensor. After substituting the degradation function defined in the equation (4.19) and the derivative of degradation function $\partial g(\phi)/\partial \phi$ in the coupled form given in equation (4.38) follows:

$$\begin{aligned} \delta W = & \int_{\Omega} \{[(1 - \zeta)\phi^2 + \zeta] \mathbf{T} : \text{grad}^s \delta \mathbf{u}\} dV + \\ & \int_{\Omega} \left\{ 2(1 - \zeta) \phi \delta \phi W_0 + E_c \left[-\frac{1}{\ell_f} (1 - \phi) \delta \phi + \ell_f \text{grad} \phi \text{grad} \delta \phi \right] \right\} dV. \end{aligned} \quad (4.39)$$

The strong form of the coupled formulation gives the local statement for the phase-field method and is derived by applying the divergence principle to equation (4.39)

$$\text{div} \left([(1 - \zeta)\phi^2 + \zeta] \mathbf{T} \right) = \mathbf{0} \quad (4.40a)$$

$$\underbrace{2(1 - \zeta) \phi W_0}_{\text{driving force}} + \underbrace{E_c \left[-\frac{1}{\ell_f} (1 - \phi) + \ell_f \text{div} \phi \right]}_{\text{resistance to crack}} = 0. \quad (4.40b)$$

Equation (4.40a) refers to the balance of momentum describing the viscoelastic response, and equation (4.40b) is the phase-field evolution of the diffusive crack. The first term of the phase-field evolution is responsible for driving the crack, and the second term refers to the geometric resistance to the propagation of the crack. W_0 is the energy stored in material domain with $W_0 = \max_{0 < \phi < t} W_0(\mathbf{x}, \phi)$ to avoid an irreversibility in the crack propagation [100].

The time derivative of the phase-field variable needs to follow $\dot{\phi} \leq 1$ to avoid crack irreversibility.

4.5.1 Boundary conditions

The necessary boundary conditions have to be postulated for the displacement field variable \mathbf{u} and the phase-field damage variable ϕ to solve the phase-field damage formulation. To this end, the surface $\partial\Omega$ is decomposed to the primary fields, the displacement and damage fields

$$\partial\Omega = \partial\Omega_{\mathbf{u}}^D \cup \partial\Omega_{\mathbf{t}}^N \quad \text{and} \quad \partial\Omega = \partial\Omega_{\phi}^D \cup \partial\Omega_{\nabla\phi}^N \quad (4.41)$$

with $\partial\Omega_{\mathbf{u}}^D \cap \partial\Omega_{\mathbf{u}}^N = \emptyset$ and $\partial\Omega_{\phi}^D \cap \partial\Omega_{\nabla\phi}^N = \emptyset$. The prescribed displacement \mathbf{u} and traction \mathbf{t} of the mechanical problem on the boundaries are postulated with the Dirichlet and Neumann boundary conditions

$$\mathbf{u}(\mathbf{x}, t) = \mathbf{u}_D(\mathbf{x}, t) \quad \text{on} \quad \partial\Omega_{\mathbf{u}}^D \quad \text{and} \quad \mathbf{T} \cdot \mathbf{n} = \mathbf{t} \quad \text{on} \quad \partial\Omega_{\mathbf{t}}^N. \quad (4.42)$$

For the phase-field damage, the cracked region is constrained by the Dirichlet and the Neumann boundary conditions on the crack surface with

$$\phi(\mathbf{x}, t) = 0 \quad \text{at} \quad \mathbf{x} \in \partial\Omega_{\phi}^D \quad \text{and} \quad \nabla\phi \cdot \mathbf{n} = 0 \quad \text{on} \quad \partial\Omega_{\nabla\phi}^N. \quad (4.43)$$

4.6 Mesh sensitivity study

It is a well-established fact that the numerical solution obtained from the finite element method depends on the size of the finite element mesh, especially in the case of damage evolution. In the phase-field approach, the

propagation of a crack is treated in terms of the diffusive order parameter. Initial studies with locally refined finite element meshes produce good results with smaller errors in the force-displacement comparison of the test and the simulation results. However, a refined mesh representing a sharp crack is computationally expensive. Therefore, a mesh sensitivity study is performed to ensure a convergent solution with a computationally less expensive mesh size, i.e., using a coarser mesh size in finite element analysis. The mesh sensitivity study is conducted on a V-shaped notch specimen consistent with the angular specimen described in DIN ISO 34-1. This specimen is applied with the tensile load boundary conditions (see Figure 4.3).

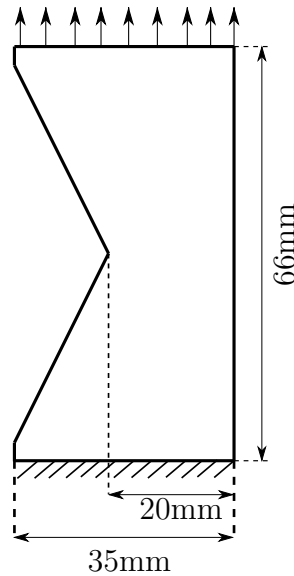


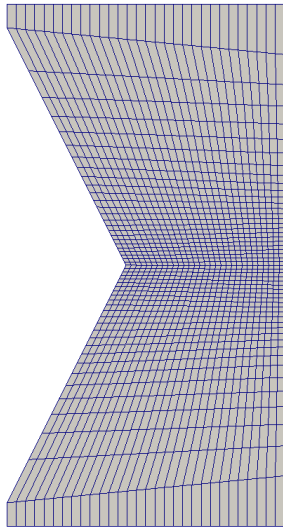
Figure 4.3: V-shaped notch sample of thickness 2mm applied with tensile boundary conditions

Miehe et al. [103] proposed criteria of the mesh size for 2D elements, which is adapted for 3D elements. According to the proposed criteria, the initial crack length ℓ_f mm, and the mesh size h mm need to satisfy the condition

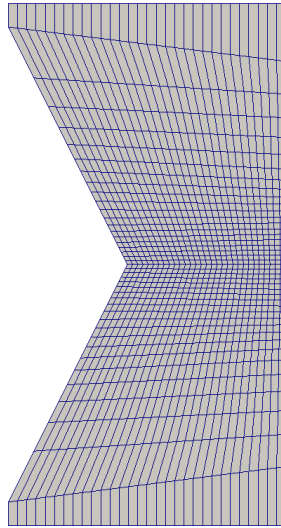
$$h \ll \frac{\ell_f}{2}. \quad (4.44)$$

In this current study for the mesh sensitivity, the V-notched sample is discretised with 8-node hexahedral elements with a refined mesh at the transition zone. The sensitivity study is conducted for a length-scale parameter $\ell_f = 9\text{mm}$. Here six different mesh sizes h mm are used to demonstrate

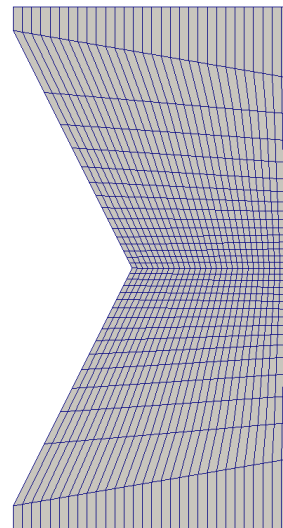
the sensitivity of the mesh in crack propagation. Figure 4.4 shows the six different meshes refined locally at the V-shaped notch.



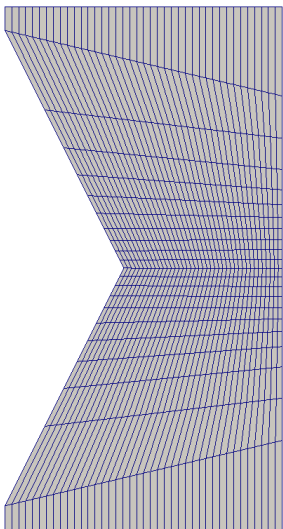
(a) Mesh 1:
 $h = 0.502\text{mm}$



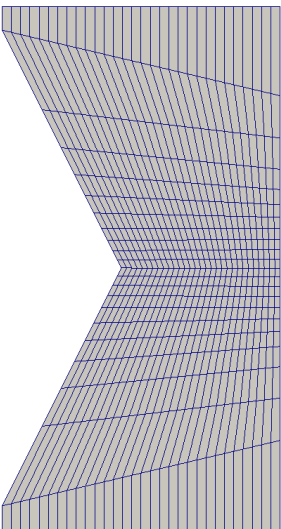
(b) Mesh 2:
 $h = 1.230\text{mm}$



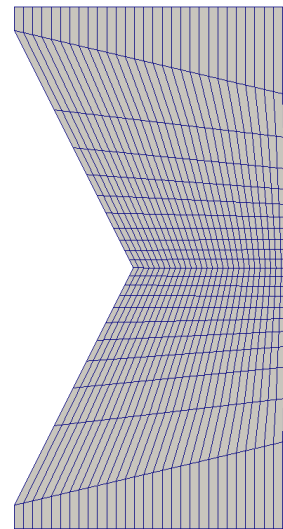
(c) Mesh 3:
 $h = 1.490\text{mm}$



(d) Mesh 4:
 $h = 2.028\text{mm}$



(e) Mesh 5:
 $h = 2.734\text{mm}$



(f) Mesh 6:
 $h = 3.751\text{mm}$

Figure 4.4: Meshes with different mesh lengths are considered to study the mesh sensitivity with locally refined meshes at the transition zone

The discretised finite element model with different mesh sizes is defined with

the finite strain viscoelastic material properties and the critical energy release rate as the phase-field damage material parameter (see Table 4.1).

Table 4.1: Finite-strain viscoelastic material parameters and phase-field damage parameters to perform the mesh sensitivity study

Material parameters of finite-strain viscoelastic model			
		Relaxation times [s]	Stiffness parameters
Equilibrium	c_{10} [MPa]		9.886
	c_{20} [MPa]		-1.414
	c_{30} [MPa]		3.214
	D [MPa]		0.306
Non-equilibrium	c_{101} [MPa]	0.5	4.886
	c_{102} [MPa]	10	0.886
	c_{103} [MPa]	100	0.055
	c_{104} [MPa]	1000	0.005
Energy release rate	E_c [N/mm ²]		4.12

The load-displacement curve is shown in figure 4.5 for different mesh lengths. It can be depicted from the curves that the initial slope of the individual curves is approximately the same. However, the deviation in the peak forces to failure is $\leq 15\%$ with a change in mesh size. The maximum force required to initiate a crack in the sample decreases for smaller mesh lengths h mm. This decrease in peak force is due to the approximation of steep gradients at locally refined meshes. However, the locally refined mesh increases computational efforts and costs. The value of the phase-field order variable reaches a minimum with the crack propagation at the notch. However, the material also degrades the viscoelastic properties globally. As a result, the numerical results lead to a singularity at the phase-field variable $\phi = 0.17$ for $h = 1.23$ mm. The phase-field model computes the crack propagation to $0.21 \leq \phi \leq 0.31$ for other mesh sizes. In this work, a mesh length of $h = 1.23$ mm is adopted to compromise with the accuracy of the numerical

results to reduce computational efforts.

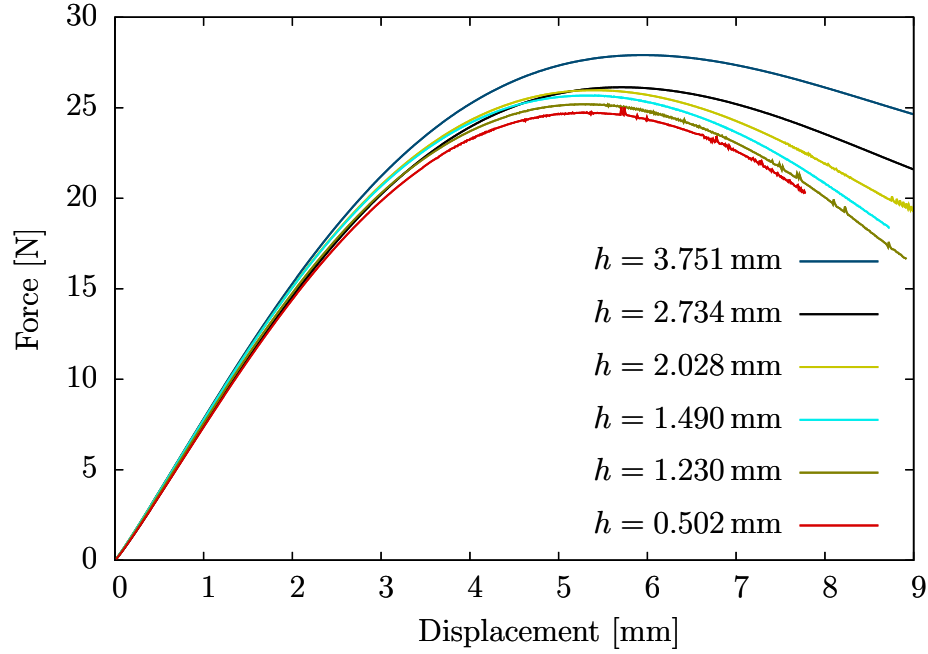


Figure 4.5: Computational results of single edge V-shaped notch sample with different mesh length

Computational results of the crack propagation in the V-shaped notched specimen with a mesh size of $h = 1.2301$ mm are shown in the figures 4.6a -4.6f until fracture at time $t = 990$ s. It is realised that the material tends to degrade its stiffness at the transition region and globally with a maximum value of the phase-field variable $\phi \approx 0.75$ close to the faces applied with displacement and fixed boundary condition.

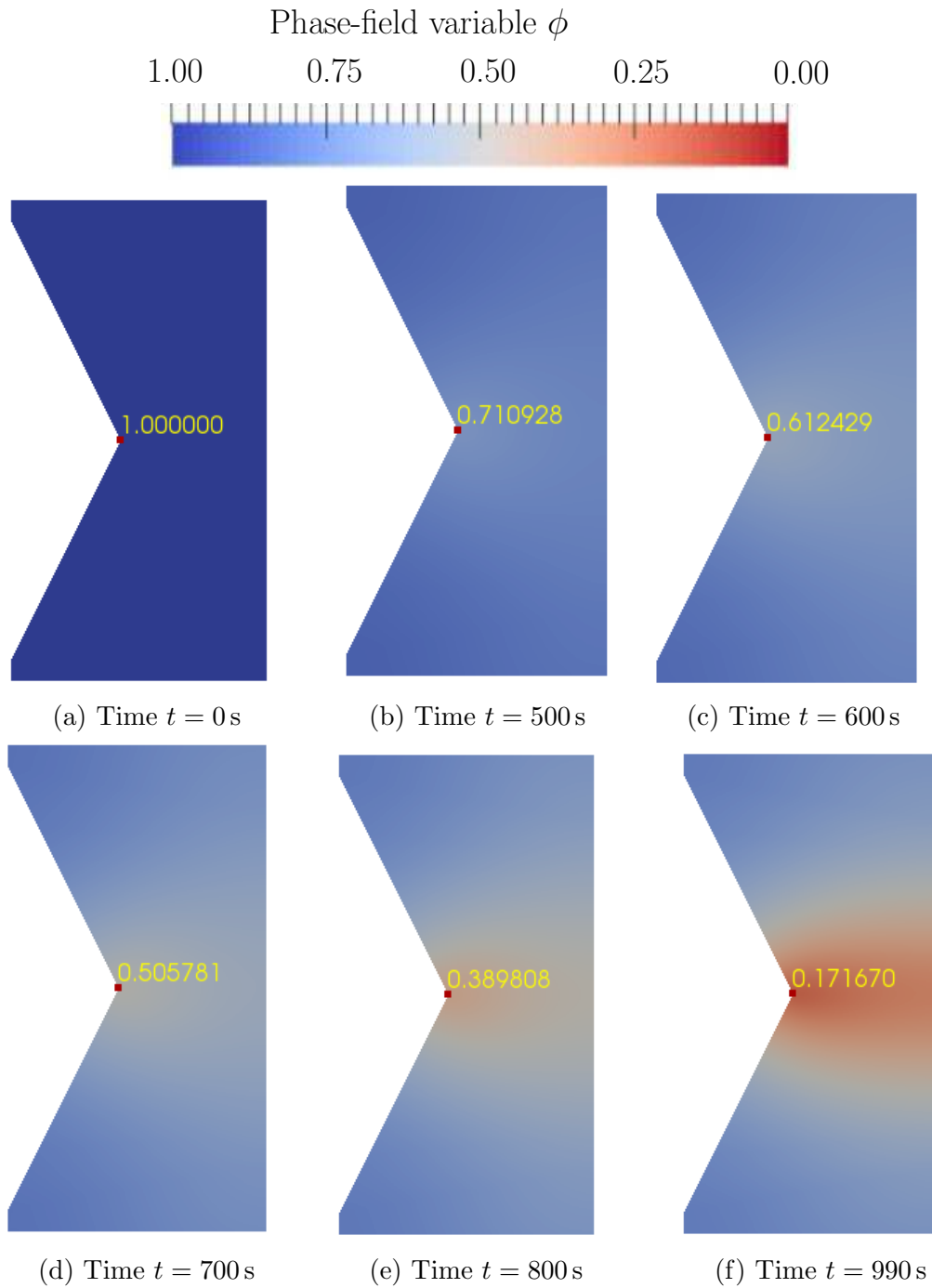


Figure 4.6: Meshes with different mesh lengths are considered to study the mesh sensitivity with locally refined meshes at the transition zone

5

Numerical implementation

The moisture diffusion and mechanical behaviours have been described in chapters 3 and 4 using the initial boundary value problem of a coupled system of equations. The solution of this system is generally not possible analytically. For this reason, the finite element method is used to approximate the solution. However, the finite element method can not solve with the strong form of the differential equation. Hence, the so-called weak form is derived as the integral over the solution domain. This weak formulation is a primary requirement in the application of approximation methods. Integral principles in the basis of continuum mechanics are based on [12]

- the principle of virtual work,
- the principle of virtual forces,
- and the principle of minimisation of the total potential.

The following chapter describes the numerical implementation of the weak forms and the solution strategies used to solve the defined partial differential equations. For the numerical implementation, the open-source finite element library deal. II is used to solve the coupled system of equations [11, 7].

5.1 Coupled diffusion and viscoelasticity

The governing partial differential equations for the coupled system of equations are defined in Chapter 3 to model the ageing behaviour of adhesives under the moisture influence

$$\operatorname{div}(\mathbf{T}(\bar{\mathbf{B}}, \bar{\mathbf{B}}_e^j, J, m)) = \mathbf{0}, \quad (5.1a)$$

$$\dot{m} - D \operatorname{div}(\operatorname{grad}(m - m_b)) = 0, \quad (5.1b)$$

where the immobile moisture concentration m_b distributed in the spatial domain of the material is evaluated with the evolution equation (3.2). The weak form of the governing equations is derived to solve the coupled problem using the finite element method.

To this end, the weak form of the diffusion equation is derived by multiplying equation (5.1b) with an arbitrary test function δm and integrating over the material volume

$$\int_{\Omega} \delta m \dot{m} dV = \int_{\Omega} \delta m D \operatorname{div}(\operatorname{grad}(m - m_b)) dV. \quad (5.2)$$

Applying the divergence theorem on equation (5.2) leads to

$$\int_{\Omega} \delta m \dot{m} dV = \int_{\Omega} [\operatorname{div}(\delta m D \operatorname{grad}(m - m_b)) - \operatorname{grad} \delta m \cdot D \operatorname{grad}(m - m_b)] dV. \quad (5.3)$$

The first term of the right side is transformed into a surface integral using the divergence theorem. This transformation results in an expression for the flux on the boundary

$$\int_{\Omega} \operatorname{div}(\delta m D \operatorname{grad}(m - m_b)) dV = \int_{\partial\Omega} \delta m D \operatorname{grad}(m - m_b) \cdot \mathbf{n} dA = \int_{\partial\Omega} \delta m \mathbf{q} dA. \quad (5.4)$$

Combing equations (5.4) and (5.3) and considering the flux-free boundary conditions leads to the weak form of the diffusion equation as

$$\int_{\Omega} \delta m \dot{m} dV + \int_{\Omega} [\operatorname{grad} \delta m \cdot D \operatorname{grad}(m - m_b)] dV = 0. \quad (5.5)$$

The diffusion is a long time process for the material to reach from the initial to the steady state. Therefore, the mathematical equation must consider a larger time step to solve the problem with less computational effort. Both the explicit and implicit time derivatives have temporal truncation errors for larger time steps [95]. Therefore a second order time derivative proposed by Crank-Nicolson [32] is used to solve the diffusion problem. The time discretisation of the weak form using the Crank-Nicolson method leads to the residual $r_m(m)$

$$r_m(m) = \int_{\Omega} \delta m \frac{m^{t+1} - m^t}{\Delta t} dV + \int_{\Omega} \left[\text{grad} \delta m \cdot D \frac{1}{2} \text{grad} (m^{t+1} - m_b^{t+1}) \right] dV - \int_{\Omega} \left[\text{grad} \delta m \cdot D \frac{1}{2} \text{grad} (m^t - m_b^t) \right] dV = 0, \quad (5.6)$$

where $(\bullet)^{t+1}$ and $(\bullet)^t$ are the values of the field variables calculated at current time $t+1$ s and previous time t s steps. The evolution equation (3.2) is solved locally using the Crank-Nicolson method to evaluate the immobile moisture concentration as

$$\frac{m_b^{t+1} - m_b^t}{\Delta t} = \frac{1}{2} [\alpha (m^{t+1} - m^t)] - \frac{1}{2} [(\alpha + \beta) (m_b^{t+1} - m_b^t)]. \quad (5.7)$$

Based on the virtual displacements principle, an infinitesimally small and kinematically admissible test function is chosen as a virtual displacement $\delta \mathbf{u}$ to derive the weak formulation of the momentum balance equation (5.1a) as

$$\int_{\Omega} \delta \mathbf{u} \cdot \text{div} \mathbf{T} (\bar{\mathbf{B}}, \bar{\mathbf{B}}_e^j, J, m) dV = \mathbf{0}. \quad (5.8)$$

The divergence theorem is applied on equation (5.8) to derive the residual $r_{\mathbf{u}}(\mathbf{u})$ of the momentum balance

$$r_{\mathbf{u}}(\mathbf{u}) = \int_{\Omega} \mathbf{T} (\bar{\mathbf{B}}, \bar{\mathbf{B}}_e^j, J, m) : \text{grad}^s \delta \mathbf{u} dV - \int_{\partial \Omega} \mathbf{t} \cdot \delta \mathbf{u} dA = \mathbf{0}, \quad (5.9)$$

where the Cauchy stress tensor is calculated using the equation (3.42)¹ by considering the moisture-dependent stiffness parameters².

¹Detailed explanation in derivation and evaluation of the Cauchy stress tensor is given in the section A.1

²Interpolation of the stiffness properties concerning the finite-strain viscoelastic ma-

5.1.1 Linearisation

The weak form of the balance of momentum shown in the equation (5.9) yields the static equilibrium in the form of a non-linear differential vector equation. The differential equation is treated to consider the geometrical non-linearity because of the large deformations. The linearised approximation of the non-linear governing equations is solved with Newton's method using

$$\mathbf{R}(\boldsymbol{\Xi} + \Delta\boldsymbol{\Xi}) \approx \mathbf{R}(\boldsymbol{\Xi}) + D_{\Delta\boldsymbol{\Xi}}\mathbf{R}(\boldsymbol{\Xi}) \cdot d\boldsymbol{\Xi} = 0, \quad (5.10)$$

where $D_{\Delta\boldsymbol{\Xi}}(\bullet)$ represents the directional derivative, also known as the spatial tangent tensor, that describes the change in the residuals $\mathbf{R}(\boldsymbol{\Xi})$ in the direction of the unknown vector $\boldsymbol{\Xi}$. The component of the directional derivative \mathbf{K}^{mm} known as the diffusive matrix is

$$\mathbf{K}^{mm} = \int_{\Omega} \text{grad } \delta m \text{ grad } \delta m \, dV, \quad (5.11)$$

and the direction derivative component \mathbf{K}^{uu} in the direction $\Delta\mathbf{u}$ is

$$\begin{aligned} \mathbf{K}^{uu} = D_{\Delta\mathbf{u}}\mathbf{r}(\mathbf{u}) &= \int_{\Omega} D_{\Delta\mathbf{u}}(\mathbf{T}(\bar{\mathbf{B}}, \bar{\mathbf{B}}_e^j, J, m)) : \text{grad}^s \delta\mathbf{u} \, dV \\ &+ \int_{\Omega} \mathbf{T}(\bar{\mathbf{B}}, \bar{\mathbf{B}}_e^j, J, m) : [\text{Grad } \delta\mathbf{u} \cdot D_{\Delta\mathbf{u}}\mathbf{F}^{-1}] \, dV, \end{aligned} \quad (5.12)$$

the directional derivative \mathbf{K}^{uu} is simplified to

$$\begin{aligned} \mathbf{K}^{uu} = D_{\Delta\mathbf{u}}\mathbf{r}(\mathbf{u}) &= \int_{\Omega} \text{grad}^s \Delta\mathbf{u} : \overset{4}{\boldsymbol{\kappa}}(\bar{\mathbf{B}}, \bar{\mathbf{B}}_e^j, J, m) : \text{grad}^s \delta\mathbf{u} \, dV \\ &+ \int_{\Omega} \text{grad } \delta\mathbf{u} : [\text{grad } \Delta\mathbf{u} \cdot \mathbf{T}(\bar{\mathbf{B}}, \bar{\mathbf{B}}_e^j, J, m)] \, dV. \end{aligned} \quad (5.13)$$

Here, the tangent $\overset{4}{\boldsymbol{\kappa}}$ is calculated as the sum of the volumetric $\overset{4}{\boldsymbol{\kappa}}_{\text{vol}}$ and isochoric components composing of the equilibrium $\overset{4}{\boldsymbol{\kappa}}_{\text{eq}}(\bar{\mathbf{B}}, m)$ and $j =$

terial model is discussed in the chapter 3.3.2. The interpolated stiffness parameters are calculated at every integration point to consider the influence of the inhomogeneous moisture distribution on the stiffness properties.

$1, 2, \dots, n$ non-equilibrium $\kappa_{\text{neq}}^4(\bar{\mathbf{B}}_e^j, m)$ parts of the viscoelastic model. The equation (A.6) in the Appendix defines the tangent matrices. $\bar{\mathbf{B}}_e^j$ of the j^{th} non-equilibrium part is calculated from the evolution equation of the inelastic right Cauchy-Green deformation tensor $\bar{\mathbf{C}}_i^j$ (see chapter 3.3). This evolution equation is solved with the implicit Euler method in time combined with the local Newton method in space at every integration point [72].

5.1.2 Finite element implementation

The diffusive flux over the Neumann boundary is neglected because of the symmetric boundary conditions, and the mechanical problem is considered with the traction-free Neumann boundary conditions. To this end, the weak forms of the coupled system of equations follow:

$$\begin{aligned} \mathbf{r}_{\mathbf{u}}(\mathbf{u}) &= \int_{\Omega} \mathbf{T}(\bar{\mathbf{B}}, \bar{\mathbf{B}}_e^j, J, m) : \text{grad}^s \delta \mathbf{u} \, dV = \mathbf{0} \\ \mathbf{r}_m(m) &= \int_{\Omega} \delta m \frac{m^{t+1} - m^t}{\Delta t} \, dV + \int_{\Omega} \left[\text{grad} \delta m \cdot D \frac{1}{2} \text{grad} (m^{t+1} - m_b^{t+1}) \right] \, dV \\ &\quad - \int_{\Omega} \left[\text{grad} \delta m \cdot D \frac{1}{2} \text{grad} (m^t - m_b^t) \right] \, dV = 0. \end{aligned} \quad (5.14)$$

The Finite-Element-Method is based on the approximation of the displacement \mathbf{u} and the moisture concentration m . The approximation of the primary variables follows

$$\mathbf{u} = \sum_{i=1}^{n_{\text{ele}}} \mathbf{N}_i^{\mathbf{u}} \mathbf{u}_i, \quad m = \sum_{i=1}^{n_{\text{ele}}} N_i^m m_i, \quad (5.15)$$

where n_{ele} is a set of degrees of freedom of an element and $\mathbf{N}_i^{\mathbf{u}}$ and N_i^m are the shape functions of the displacement field \mathbf{u} and the moisture concentration

$$\mathbf{N}_i^{\mathbf{u}} = \begin{bmatrix} N_i & 0 & 0 \\ 0 & N_i & 0 \\ 0 & 0 & N_i \end{bmatrix}, \quad (5.16)$$

where, $N_i = N_1, N_2, \dots, N_{n_{\text{ele}}}$ denotes the respective shape function values of an element at the quadrature points associated with the respective nodes. The virtual quantities of the primary variables and their derivatives are dis-

cretised as

$$\begin{aligned}\delta \mathbf{u} &= \sum_{i=1}^{n_{\text{ele}}} \mathbf{N}_i^{\delta \mathbf{u}} \delta \mathbf{u}_i, & \delta m &= \sum_{i=1}^{n_{\text{ele}}} N_i^m \delta m_i, \\ \text{grad}^s \delta \mathbf{u} &= \sum_{i=1}^{n_{\text{ele}}} \mathbf{S}_i^{\mathbf{u}} \delta \mathbf{u}_i, & \text{grad} \delta m &= \sum_{i=1}^{n_{\text{ele}}} \mathbf{S}_i^m \delta m_i.\end{aligned}\quad (5.17)$$

Here, the strain-displacement matrix \mathbf{S} is introduced as the derivative of the shape function

$$\mathbf{S}_i^{\mathbf{u}} = \begin{bmatrix} N_{i,x} & 0 & 0 \\ 0 & N_{i,y} & 0 \\ 0 & 0 & N_{i,z} \\ N_{i,y} & N_{i,x} & 0 \\ 0 & N_{i,z} & N_{i,y} \\ N_{i,z} & 0 & N_{i,x} \end{bmatrix}, \quad \mathbf{S}_i^m = \begin{bmatrix} N_{i,x} \\ N_{i,y} \\ N_{i,z} \end{bmatrix} \quad \text{with} \quad \begin{bmatrix} N_{i,x} \\ N_{i,y} \\ N_{i,z} \end{bmatrix} = \begin{bmatrix} \frac{\partial N_i}{\partial x} \\ \frac{\partial N_i}{\partial y} \\ \frac{\partial N_i}{\partial z} \end{bmatrix}. \quad (5.18)$$

Inserting the approximated field variables and their derivatives in the residuals of the coupled system of equations leads to

$$\begin{aligned}\mathbf{r}_{\mathbf{u}}(\mathbf{u}) &= \int_{\Omega} \mathbf{T}(\bar{\mathbf{B}}, \bar{\mathbf{B}}_e^j, J, m) : (\mathbf{S}_i^{\mathbf{u}})^{\text{T}} dV = \mathbf{0} \\ r_m(m) &= \int_{\Omega} N_i^m \frac{m^{t+1} - m^t}{\Delta t} dV + \int_{\Omega} \left[\mathbf{S}_i^m \cdot D \frac{1}{2} \text{grad} (m^{t+1} - m_b^{t+1}) \right] dV \\ &\quad - \int_{\Omega} \left[\mathbf{S}_i^m \cdot D \frac{1}{2} \text{grad} (m^t - m_b^t) \right] dV = 0.\end{aligned}\quad (5.19)$$

The displacement \mathbf{u} and moisture concentration fields m of the coupled system of equations are solved with the Newton-Raphson method using equation (5.10). The linearisation is followed by

$$\underbrace{\begin{bmatrix} \mathbf{K}^{\mathbf{u}\mathbf{u}} & \mathbf{K}^{\mathbf{u}m} \\ \mathbf{K}^{m\mathbf{u}} & \mathbf{K}^{mm} \end{bmatrix}}_{\mathbf{D}_{\Delta \Xi} \mathbf{R}(\Xi)} \underbrace{\begin{bmatrix} d\mathbf{u} \\ dm \end{bmatrix}}_{d\Xi} = \underbrace{\begin{bmatrix} -\mathbf{r}_{\mathbf{u}}(\mathbf{u}) \\ -r_m(m) \end{bmatrix}}_{\mathbf{R}(\Xi)}. \quad (5.20)$$

The monolithic solution may encounter convergence problems because of the rearrangement of the stress field with a change in moisture concentration. Therefore, the displacement \mathbf{u} and diffusion m fields of the coupled problem

are solved individually as a coupled staggering field to find a stable implicit solution. In this method, the governing equation for moisture diffusion is solved in the first step then the effects of moisture on the stiffness properties are superimposed to investigate the viscoelastic behaviour. To this end, the elements of the tangent matrix \mathbf{K}^{um} and \mathbf{K}^{mu} are set to "null". As a result of this approach, the system of equations is solved as follows

$$\begin{bmatrix} \mathbf{K}^{uu} & 0 \\ 0 & \mathbf{K}^{mm} \end{bmatrix} \begin{bmatrix} d\mathbf{u} \\ dm \end{bmatrix} = \begin{bmatrix} -\mathbf{r}_u(\mathbf{u}) \\ -r_m(m) \end{bmatrix}. \quad (5.21)$$

The tangent matrix of the displacement and moisture concentration fields are expressed as

$$\begin{aligned} D_{\Delta u} \mathbf{r}_u(\mathbf{u}) &= \mathbf{K}^{uu} = \int_{\Omega} \left[\mathbf{S}_i^u : \overset{4}{\boldsymbol{\kappa}} : \mathbf{S}_j^u + \mathbf{S}_i^u : [\mathbf{S}_j^u \cdot \mathbf{T}] \right] dV \\ D_{\Delta m} r_m(m) &= \mathbf{K}^{mm} = \int_{\Omega} \mathbf{S}_i^m \mathbf{S}_j^m dV. \end{aligned} \quad (5.22)$$

Analytical integration of these integrals are complex and even impossible in some cases. Therefore, a numerical quadrature scheme based on the Gauss quadrature approximates the corresponding integrals. This method replaces integrals with the weighted sum of the integral evaluated at the integration points. The integral function then takes the form

$$\int_{\Omega} f(\mathbf{x}) dV = \sum_{q=1}^{\text{gp}} w_q f(\mathbf{x}_q). \quad (5.23)$$

gp is the number of integration points, w_q are the weight factors, and the function values are calculated at the corresponding integration points \mathbf{x}_q . The coupled system of equations and the evolution equations are solved at the integration points. Using the staggered approach, the Gauss quadrature is applied to solve the coupled system. The implementation of the coupled diffusion and viscoelasticity in deal.II is explained with the help of the Algorithms 1 and 2.

The implementation of the Langmuir-type diffusion model in deal.II is explained with algorithm 1. The geometry is imported as input data to generate the finite element mesh, and the boundary faces are defined to apply Dirichlet and Neumann boundary conditions (see equation (3.7) and (3.8)).

Algorithm 1: Implementation of Langmuir-type diffusion

Given : Three-dimensional geometry parameters (length, width and thickness) and material parameters D, β, α

Return: Solution values $m_f, m_b, m = m_f + m_b$ on each cell

- 1 Set initial values of solution variables $m = m_b = 0$
- 2 **foreach** *time loop with time step $\Delta t = 1s$* **do**
- 3 **Assemble system of equations**
- 4 **foreach** *cell $k \in \Omega$* **do**
- 5 extract function values of total moisture concentration m
- 6 extract function values of immobile moisture concentration m_b
- 7 extract gradients of function values for free moisture concentration $\text{grad } m^t$
- 8 **foreach** *quadrature points q on each cell k* **do**
- 9 extract shape values at the total and immobile moisture concentration degrees of freedom per cell
- 10 extract gradient of shape values at the total and immobile moisture concentration degrees of freedom per cell
- 11 extract weight factors w_q
- 12 update the immobile moisture concentration with $m_b^{t+1} = m_b^t + \Delta m_b$
- 13 compute left-hand side A
- 14 compute right-hand side B
- 15 **end**
- 16 **end**
- 17 Apply Dirichlet boundary conditions
- 18 Apply Neumann boundary conditions
- 19 Solve the system of equations
- 20 Solve the evolution equation to identify immobile moisture concentration m_b & $\Delta m_b = m_b^{t+1} - m_b^t$
- 21 Update total moisture concentration $m = m_f + m_b$
- 22 Distribute results to destination vectors
- 23 **end**

Then the material parameters are defined to specify the diffusion behaviour of a specific material. The number of degrees of freedom (DOF) is determined for the defined mesh to initialise the solution vectors and matrices of appropriate size. Once the model is set up, the time increment is initiated with the time step size of Δt s. A control flow statement is programmed to implement and assemble the residual $r_m(m)$ and the diffusivity matrix \mathbf{K}^{mm} . The assembled system of matrices is solved with a preconditioned generalised

minimal residual method [126] with Jacobi preconditioning. Output of the simulation results at each time step is distributed to the destination solution vectors and is saved to the visualisation data with inbuilt output drivers of deal.II.

Algorithm 2: Implementation of finite-strain viscoelasticity model

Given : Geometry and material parameters of finite-strain viscoelastic material model

Return: Computation of residual and tangent matrix

```

1 foreach cell  $K \in \Omega$  do
2   extract local values and gradients of the vector
3   extract local values of total absolute moisture concentration  $m$ 
4     foreach quadrature point  $q\_point$  on each cell  $K$  do do
5       compute total moisture concentration  $m$  at quadrature points
6       extract displacement gradient  $\text{grad } \mathbf{u}$ 
7       compute deformation gradient tensor  $\mathbf{F} = \mathbf{I} + \text{grad } \mathbf{u}$ 
8       compute  $\bar{\mathbf{C}}_i^j$  of  $j^{\text{th}}$  Maxwell element using evolution equation
9         (3.45)
10      compute  $\bar{\mathbf{B}}_e^j = \mathbf{F} \cdot (\bar{\mathbf{C}}_i^j)^{-1} \cdot \mathbf{F}^T$  of  $j^{\text{th}}$  Maxwell element
11      interpolate the mechanical properties as the function of
12        moisture concentration
13      evaluate  $\mathbf{T}_{\text{eq}}$  and  $\kappa_{\text{eq}}^{\text{iso}}$  with  $W_{\text{eq}}$ 
14      evaluate  $\mathbf{T}_{\text{vol}}$  and  $\kappa_{\text{eq}}$  with  $W_{\text{vol}}$ 
15      evaluate  $\mathbf{T}_{\text{neq}}^j$  and  $\kappa_{\text{neq}}^j$  with  $W_{\text{neq}}^j$ 
16      compute the sum of equilibrium and non-equilibrium
17        Kirchhoff stress and tangent tensors
18      Assemble residual and tangent matrices computed at every
19        degree of freedom for all cells.
20    end
21  end

```

After solving the diffusion problem, the influence of the moisture concentration is superimposed over the finite-strain viscoelastic model. Algorithm 2 explains implementing the finite-strain viscoelastic material model. The first step in implementing the viscoelastic material model requires extract-

ing the local displacement vector values and their gradients to compute the deformation gradient and the Cauchy-Green deformation tensors.

The inelastic deformation tensor $\bar{\mathbf{C}}_i^j$ of j^{th} Maxwell element is computed with the evolution equation using the implicit Euler method in time combined with the local Newton method in space. Then $\bar{\mathbf{B}}_e^j$ of j^{th} Maxwell element is computed with the mathematical relationship $\bar{\mathbf{B}}_e^j = \mathbf{F} \cdot (\bar{\mathbf{C}}_i^j)^{-1} \cdot \mathbf{F}^T$. The stress and tangent tensors are calculated for the equilibrium and non-equilibrium parts of the viscoelastic model to build the residual and the tangent matrices. These matrices are assembled to solve the problem using the finite element method. The displacement boundary conditions are applied as the Dirichlet boundary conditions to introduce tensile loading conditions. The finite element model is solved using Newton's method with pseudo time increment until the residual norm reaches the convergence tolerance. The solution vectors are assigned to the destination output vectors and written to the visualisation and output files for post-processing.

5.2 Modelling phase-field damage model

An analytical solution to the strong form of the partial differential equation is often impossible. For this reason, the finite element method is chosen as an approximate method to solve the coupled formulation defined in equations (4.40a) and (4.40b).

5.2.1 Finite element implementation

In order to develop a numerical scheme of the coupled system, it is convenient to express the partial differential equations in weak forms.

$$\begin{aligned} \mathbf{r}_i^{\mathbf{u}} &= \int_{\Omega} \{ [(1 - \zeta)\phi^2 + \zeta] \mathbf{T} : \text{grad}^s \delta \mathbf{u} \} dV = \mathbf{0} \\ \mathbf{r}_i^{\phi} &= \int_{\Omega} \left\{ 2(1 - \zeta)\phi \delta\phi W + E_c \left[-\frac{1}{\ell_f} (1 - \phi) \delta\phi + \ell_f \text{grad}\phi \text{grad}\delta\phi \right] \right\} dV = 0. \end{aligned} \quad (5.24)$$

In the context of the finite element method, the approximation of the primary variables displacement \mathbf{u} and phase-field variable ϕ follows

$$\mathbf{u} = \sum_{i=1}^{\text{n}_{\text{ele}}} \mathbf{N}_i^{\mathbf{u}} \mathbf{u}_i \quad \phi = \sum_{i=1}^{\text{n}_{\text{ele}}} N_i^{\phi} \phi_i, \quad (5.25)$$

where N_i^{ϕ} is the shape function concerning the phase-field variable and $\mathbf{N}_i^{\mathbf{u}}$ is the displacement shape function used to interpolate between the quantities at the quadrature points as given by:

$$\mathbf{N}_i^{\mathbf{u}} = \begin{bmatrix} N_i & 0 & 0 \\ 0 & N_i & 0 \\ 0 & 0 & N_i \end{bmatrix}. \quad (5.26)$$

In equation (5.26) N_i is the value of the shape function of the displacement field $\mathbf{u}_i = (u_x, u_y, u_z)^T$ at the quadrature points associated with the respective nodes. The gradient of the phase-field variable ϕ_i follow

$$\text{grad} \phi = \sum_{i=1}^{\text{n}_{\text{ele}}} \mathbf{S}_i^{\phi} \phi_i. \quad (5.27)$$

Herein, the \mathbf{S} matrix is introduced as

$$\mathbf{S}_i^{\mathbf{u}} = \begin{bmatrix} N_{i,x} & 0 & 0 \\ 0 & N_{i,y} & 0 \\ 0 & 0 & N_{i,z} \\ N_{i,y} & N_{i,x} & 0 \\ 0 & N_{i,z} & N_{i,y} \\ N_{i,z} & 0 & N_{i,x} \end{bmatrix} \quad \mathbf{S}_i^{\phi} = \begin{bmatrix} N_{i,x} \\ N_{i,y} \\ N_{i,z} \end{bmatrix}, \quad (5.28)$$

where, $N_{i,x}$, $N_{i,y}$ and $N_{i,z}$ are the derivatives of the shape functions evaluated as $\partial N_i / \partial x$, $\partial N_i / \partial y$ and $\partial N_i / \partial z$. In the same way, virtual quantities of the displacement and phase-field variables are approximated as

$$\begin{aligned} \delta \mathbf{u} &= \sum_{i=1}^{\text{n}_{\text{ele}}} \mathbf{N}_i^{\mathbf{u}} \delta \mathbf{u}_i & \delta \phi &= \sum_{i=1}^{\text{n}_{\text{ele}}} N_i^{\phi} \delta \phi_i \\ \text{grad}^s \delta \mathbf{u} &= \sum_{i=1}^{\text{n}_{\text{ele}}} \mathbf{S}_i^{\delta \mathbf{u}} \delta \mathbf{u}_i & \text{grad} \delta \phi &= \sum_{i=1}^{\text{n}_{\text{ele}}} \mathbf{S}_i^{\phi} \delta \phi_i. \end{aligned} \quad (5.29)$$

The finite element formulation to solve the coupled system of equations with an incremental method follows:

$$\begin{bmatrix} \mathbf{K}^{\mathbf{u}\mathbf{u}} & \mathbf{K}^{\mathbf{u}\phi} \\ \mathbf{K}^{\phi\mathbf{u}} & \mathbf{K}^{\phi\phi} \end{bmatrix} \begin{bmatrix} d\mathbf{u} \\ d\phi \end{bmatrix} = \begin{bmatrix} -\mathbf{r}_{\mathbf{u}}(\mathbf{u}_i) \\ -r_{\phi}(\phi_i) \end{bmatrix}. \quad (5.30)$$

Since the primary variables defined in the equation (5.25) hold for the arbitrary values $\delta\mathbf{u}$ and $\delta\phi$, the residuals of the coupled system of equations defined in equation (5.24) are expressed in term of the virtual quantities given with equation 5.29 as

$$\begin{aligned} \mathbf{r}_i^{\mathbf{u}} &= \int_{\Omega} \{ [(1-\zeta)\phi^2 + \zeta] \mathbf{T} : (\mathbf{S}_i^{\mathbf{u}})^{\mathbf{T}} \} dV = \mathbf{0}, \\ r_i^{\phi} &= \int_{\Omega} \left\{ 2(1-\zeta)\phi N_i W + E_c \left[-\frac{1}{\ell_f} (1-\phi) N_i + \ell_f (\mathbf{S}_i^{\phi})^{\mathbf{T}} \mathbf{S}_j^{\phi} \right] \right\} dV = 0, \end{aligned} \quad (5.31)$$

the elements of the tangent matrix are

$$\begin{aligned} \mathbf{K}_{i,j}^{\mathbf{u}\mathbf{u}} &= \frac{\partial \mathbf{r}_i^{\mathbf{u}}}{\partial \mathbf{u}_j} = \int_{\Omega} ((1-\zeta)\phi^2 + \zeta) \left(\mathbf{S}_i^{\mathbf{u}} : \overset{4}{\boldsymbol{\kappa}} : \mathbf{S}_j^{\mathbf{u}} + \mathbf{S}_i^{\mathbf{u}} : [\mathbf{T} \cdot \mathbf{S}_j^{\mathbf{u}}] \right) dV, \\ \mathbf{K}_{i,j}^{\mathbf{u}\phi} &= \frac{\partial \mathbf{r}_i^{\mathbf{u}}}{\partial \phi_j} = \int_{\Omega} 2(1-\zeta)\phi \mathbf{S}_i^{\mathbf{u}} : \mathbf{T}^{\mathbf{T}} \mathbf{N}_j^{\mathbf{u}} dV, \\ \mathbf{K}_{i,j}^{\phi\mathbf{u}} &= \frac{\partial r_i^{\phi}}{\partial \mathbf{u}_j} = \int_{\Omega} 2(1-\zeta)\phi \mathbf{N}_i^{\mathbf{u}} \mathbf{T}^{\mathbf{T}} : \mathbf{S}_j^{\mathbf{u}} dV, \\ \mathbf{K}_{i,j}^{\phi\phi} &= \frac{\partial r_i^{\phi}}{\partial \phi_j} = \int_{\Omega} \left\{ (1-\zeta) W N_i^{\phi} N_j^{\phi} + E_c \left[\frac{1}{\ell_f} N_i^{\phi} N_j^{\phi} + \ell_f (\mathbf{S}_i^{\phi})^{\mathbf{T}} : \mathbf{S}_j^{\phi} \right] \right\} dV. \end{aligned} \quad (5.32)$$

The coupled system for the displacement field \mathbf{u} and the phase-field ϕ are solved simultaneously using a monolithic approach. Newton's method is the basis to solve the coupled equations system using equation (5.30) with a pseudo-time step increment until the system of equations reaches predefined convergence tolerance.

Algorithm 3 describes implementing the finite-strain phase-field damage model. The finite element mesh of the three-dimensional geometry is imported as an input file. The material parameters concerning the stiffness and damage parameters are initialised. The local values and gradients of the displacement and phase-field variables are extracted to implement the coupled material model. The deformation gradient \mathbf{F} is calculated to evaluate the deformation tensors.

Algorithm 3: Implementation of finite-strain phase-field damage model

Given : Geometry and material parameters of the material model

Return: Computation of residual and tangent matrix

```

1 foreach cell  $K \in \Omega$  do
2   extract local values and gradients of phase-field and displacement
   field variables
3   foreach quadrature point on each cell  $K$  do do
4     extract displacement gradient  $\text{grad } \mathbf{u}$ 
5     compute deformation gradient tensor  $\mathbf{F} = \mathbf{I} + \text{grad } \mathbf{u}$ 
6     compute  $\bar{\mathbf{C}}_i^j$  of  $j^{\text{th}}$  Maxwell element with the evolution
   equation
7     compute  $\bar{\mathbf{B}}_e^j = \mathbf{F} \cdot (\bar{\mathbf{C}}_i^j)^{-1} \cdot \mathbf{F}^T$  of  $j^{\text{th}}$  Maxwell element
8     evaluate  $\mathbf{T}_{\text{eq}}$  and  $\kappa_{\text{eq}}^4$  with  $W_{\text{eq}}$ 
9     evaluate  $\mathbf{T}_{\text{vol}}$  and  $\kappa_{\text{vol}}^4$  with  $W_{\text{vol}}$ 
10    evaluate  $\mathbf{T}_{\text{neq}}^j$  and  $\kappa_{\text{neq}}^j$  with  $W_{\text{neq}}^j$ 
11    compute free energies of equilibrium and non-equilibrium
   parts and critical fracture energy
12    compute the sum of equilibrium and non-equilibrium
   Kirchhoff stress, free energy and tangent tensors
13    check whether the total free energy density is greater than the
   previous time step
14    assemble left and right-hand sides of matrices at every degree
   of freedom for all cells
15  end
16  update applied boundary conditions
17  solve the system of equations
18  update field variables
19  distribute results to the destination vectors
20  output results to visualisations and data files for post-processing
21 end

```

The free energy density, Cauchy stress and tangent tensors are evaluated to implement the coupled equations for the phase-field damage model as discussed in chapter 4. The FE-Model is applied with displacement boundary condition as the tensile load boundary condition, and the phase-field fracture boundary condition is applied to prepare the finite element model. The prepared finite element model is solved using Newton's method with the pre-conditioned direct generalised minimal residual method [126]. The solution

vectors are written to visualisation data with the output drivers for post-processing. The force, time and displacement data for every time step are written to the destination output file to validate simulation results with the experimental results.

5.3 Implementation in deal.II

Deal.II is an open-source FEM library developed in C++ used to implement the material models [11, 7]. Deal.II is used in the current project because of the flexibility to implement and incorporate changes in the code. Deal.II provides a wide variety of inbuilt packages to import finite element meshes, solution schemes to solve and visualisation drivers to output solution data. A particular problem is implemented by defining classes and functions to import or create the mesh, setting up the degrees of freedom, defining boundary conditions, and solving for the results to visualise with inbuilt output drivers.

Figure 5.1 shows the class hierarchy of the program implemented to solve the coupled system of equations in deal.II. The standard parent class "main ()" is defined to initialise tensors and vectors in the essential classes and header files. The main function inherits the derived class to run the program.

- **set_runtime_parameters()**: The parameters of the material model are initialised with an input file by defining parameter.h header file that includes a built-in header file *parameter_handler.h*. This function is also used to import the data of finite element mesh by reading the data.UNV input file with the built-in header file *grid_in.h*.
- **setup_system()**: The number of degrees of freedom is determined in this class. The necessary vectors and matrices are set up with the appropriate sizes to describe the system tangent, solution, and residual vectors required to define a boundary value problem.
- **setup_point_history()**: The point history subclass is set up to store the information on the elastic and inelastic deformation tensors and the material parameters at the integration points.
- **determine_mesh_dependent_parameters()**: This function is specially defined for the phase-field fracture model to identify the minimum di-

ameter of the finite element mesh. This enables locating the position of the initial crack in the geometry without modelling the crack explicitly. A conditional statement is initialised to verify that the mesh size h is always less than the length-scale parameter ℓ_f .

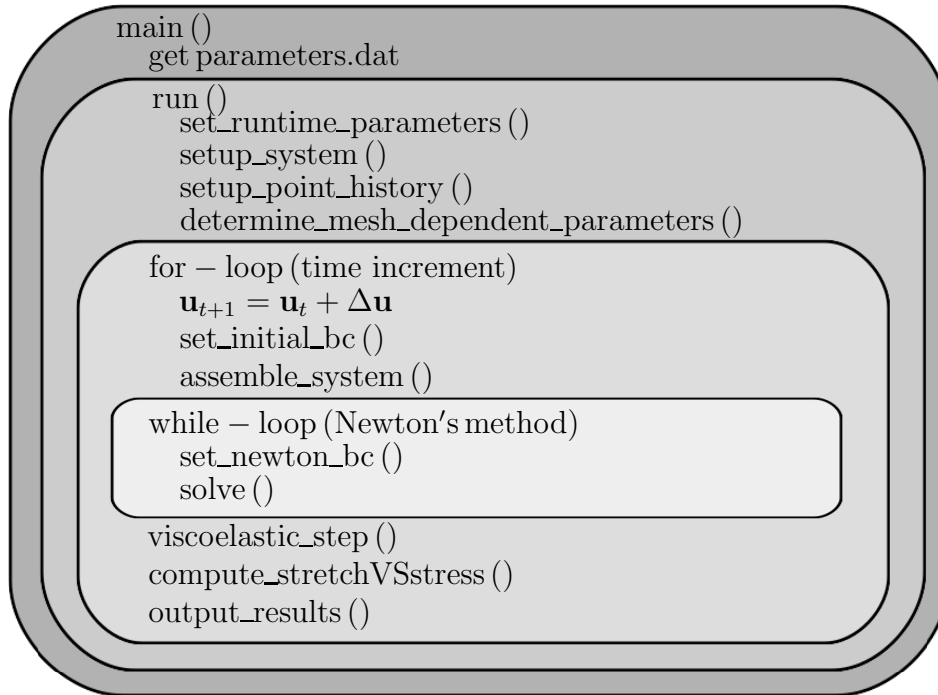


Figure 5.1: Class hierarchy in the implementation of the coupled formulation.

Once the finite element model is built, the load increment with time on the geometry is defined with a control flow statement (for-loop), and the system of equations is solved using Newton's iterative method with a pseudo-time step increment until the tolerance is reached.

- **set_initial_bc()**: This function is used to define boundary conditions to prepare the finite element model that represents the experimental setup.
- **assemble_system()**: The tangent and residuals at the individual degrees of freedom are computed, and the system of matrices is assembled to obtain a global system required for the problem to solve.
- **set_newton_bc()**: Non-linear problems are traditionally solved with the help of Newton's iterative method in several pseudo-time steps until the

tolerance is reached. The set of applied boundary conditions is set to the null value so that there is no increment of load in the pseudo-time step resulting in the overestimation of the simulation results.

- **solve()**: deal.II provides a wide variety of solvers programmed within the finite element library. This work uses a generalised minimal residual method (GMRES) solver [126] with the block diagonal preconditioner to solve the coupled system of equations.
- **viscoelastic_step()**: This header file is implemented to compute the deformation tensor at integration points with the evolution equation.
- **compute_stretchVSstress()**: The stresses at each quadrature point are computed with the constitutive equation described in Chapter 3.
- **output_results()**: To analyse the simulation results, it is necessary to have suitable visualisation data. Deal.II visualisation drivers enable output data in numerous formats (eps, povray, Gnuplot, SVG, vtk, vtu,...) for post-processing.

A list of functions presented in this work to implement the coupled material model can be found in the tutorial [114] of deal.II independent of the problem.

6

Identification of moisture diffusion parameters

This chapter investigates moisture diffusion in polyurethane adhesives with experiments and numerical simulations. The experimental investigation of moisture diffusion is conducted at Fraunhofer-Institut für Fertigungstechnik und Angewandte Materialforschung on two commercially available crosslinked polyurethane adhesives, and the material-specific parameters are identified from curve fitting process.

The goal of identifying parameters is to fit experimental and simulation data curves with minimum deviation by adjusting the material parameters. The curve fitting algorithms are classified into gradient-free and gradient methods. This work employs a gradient-free algorithm to identify optimum parameters since the gradient-based methods lead to local minima that may not be a unique solution and depends on the start value. To this end, the simplest gradient-free method proposed by Nelder and Mead [109] is chosen to optimise material parameters. This method is one of the known and simplest gradient-free methods in non-linear optimisation, and the Matlab optimisation toolbox is used to identify optimal material parameters.

The algorithm is based on an iteration of a simplex in n -dimensional parameter space. A simplex is a convex envelope spanned by $n + 1$ points for the iteration step. In the first step, the $n + 1$ points for the parameters concerning the material model are chosen to search for the optimal set of parameters that can converge with a minimum error. Then the Nelder-Mead algorithm is employed with a simplex of $n + 1$ points on the objective function to minima. The minimisation of the objective function f_{min} follows

$$f_{min}(p_1, p_2, p_3, \dots, p_m) = \min \left\{ \frac{1}{n} \sum_{i=1}^n \left(\frac{C_{sim,i}(t) - C_{exp,i}(t)}{C_{sim,i}(t) + C_{exp,i}(t)} \right)^2 \right\}, \quad (6.1)$$

where, $p_1, p_2, p_3, \dots, p_m$ are the material parameters of the concerning material model. $C_{sim,i}(t)$ and $C_{exp,i}(t)$ are the simulation and experimental data of n values for n points in time t s.

6.1 Gravimetric investigation

The measurement of moisture absorption was carried out using dynamic vapor absorption based on the gravimetric method. A sample of the adhesive is prepared, and the reference weight of the sample is measured to analyse the moisture diffusion. Then, the sample is placed in the climate chamber at a given humid atmosphere and temperature until the steady state. During the measurement, the increase or decrease in the weight of the sample relative to the reference is measured continuously to calculate the moisture diffusion. Two commercially available adhesives (adhesive-A and adhesive-B) are used to investigate the moisture absorption and desorption at an isothermal condition of 60° C. The continuous increase or decrease in the weight of the sample is used to calculate moisture mass uptake or release

$$\text{Mass uptake (or) release (\%)} = M_t (\%) = \frac{w_t - w_0}{w_0} \%, \quad (6.2)$$

where w_t is the weight of the sample measured at time t s and w_0 is the reference weight of the sample measured just before the moisture uptake or release by the sample.

6.1.1 Moisture diffusion in adhesive-A

A thin sample of thickness 0.833 mm is used to investigate moisture absorption at different relative humid atmospheric conditions varying between 10% to 98% relative humidity at 60° C. Table 6.1 shows the equilibrium moisture content $m_{\infty}(H)\%$ at the saturation state attained by the sample for $H\%$ relative humid atmosphere conducted at 60° C.

Table 6.1: Equilibrium moisture content absorbed by adhesive-A

$H\%$	10%	20%	30%	40%	50%
$m_{\infty}(H)\%$	0.11%	0.24%	0.34%	0.49%	0.69%
$H\%$	60%	70%	80%	95%	98%
$m_{\infty}(H)\%$	0.84%	0.95%	1.09%	1.38%	1.70%

Moisture absorption isotherm is determined from the moisture equilibrium content at every relative humid ($H\%$) condition. Moisture absorption is

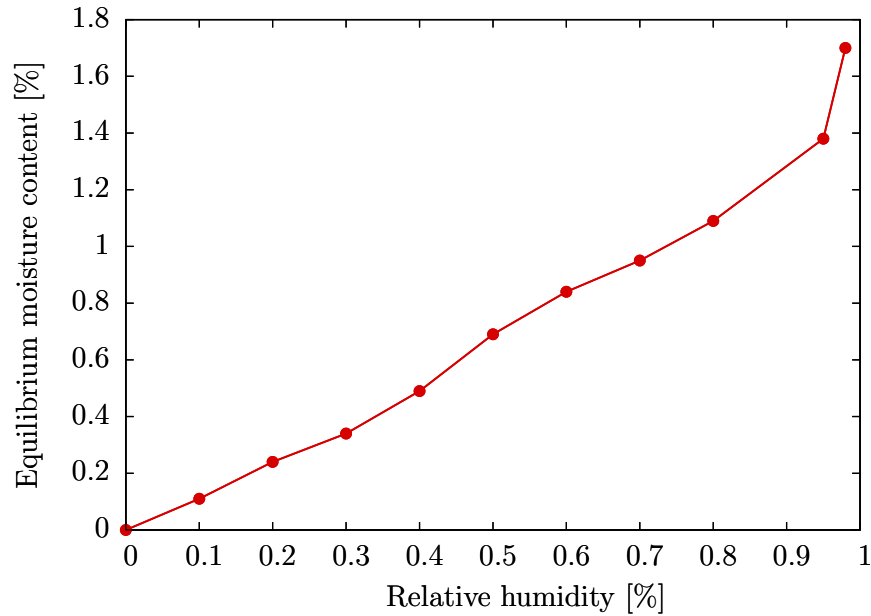


Figure 6.1: Isotherm of moisture diffusion in the crosslinked polyurethane adhesive-A at an isothermal condition 60° C

conducted for different relative humid climates varying between 0% to 98% at 60° C. Moisture absorption isotherm is non-linear, and equilibrium moisture content ranges between 0% and 1.70%, as shown in Figure 6.1.

Further, moisture desorption by the adhesive-A is investigated on the aged samples by placing the aged samples in a dry atmosphere. The decrease in the sample's weight is measured continuously to calculate the moisture release. Table 6.2 shows the equilibrium moisture content released $m_{-\infty}(H)\%$ by the sample aged at $H\%$ relative humid atmosphere conducted at 60° C.

Table 6.2: Equilibrium moisture content released by adhesive-A

$H\%$	10%	20%	30%	40%	50%
$m_{-\infty}(H)\%$	0.11%	0.24%	0.34%	0.49%	0.69%
$H\%$	60%	70%	80%	95%	98%
$m_{-\infty}(H)\%$	0.84%	0.95%	1.09%	1.38%	1.70%

Moisture desorption isotherms of the adhesive-A vary between 0% and 1.70%. The equilibrium moisture content listed in Tables 6.1 and 6.2 for absorption and desorption is identical because of no chemical reaction between moisture and the adhesive. Figure 6.2a-6.2b show the changes in the mass of the adhesive-A samples under different humid atmospheres, and the mass increases or decreases for the higher humidity atmosphere of the respective absorption or desorption tests. The time required for the adhesive-A sample to attain equilibrium is the same for different ambient humid conditions. As a result of this behaviour, parameters of the Langmuir-type diffusion model can be identified to analyse both the absorption and the desorption behaviours.

6.1.2 Moisture diffusion in adhesive-B

Thin samples of adhesive-B with a thickness of 0.15 mm are used to investigate moisture diffusion. These thin samples are placed in a climate chamber with humid air at an isothermal condition to record moisture absorption. Then, the periodic increase in weight of the sample is measured to quantify diffusion behaviour with the equation (6.2). These tests are conducted at

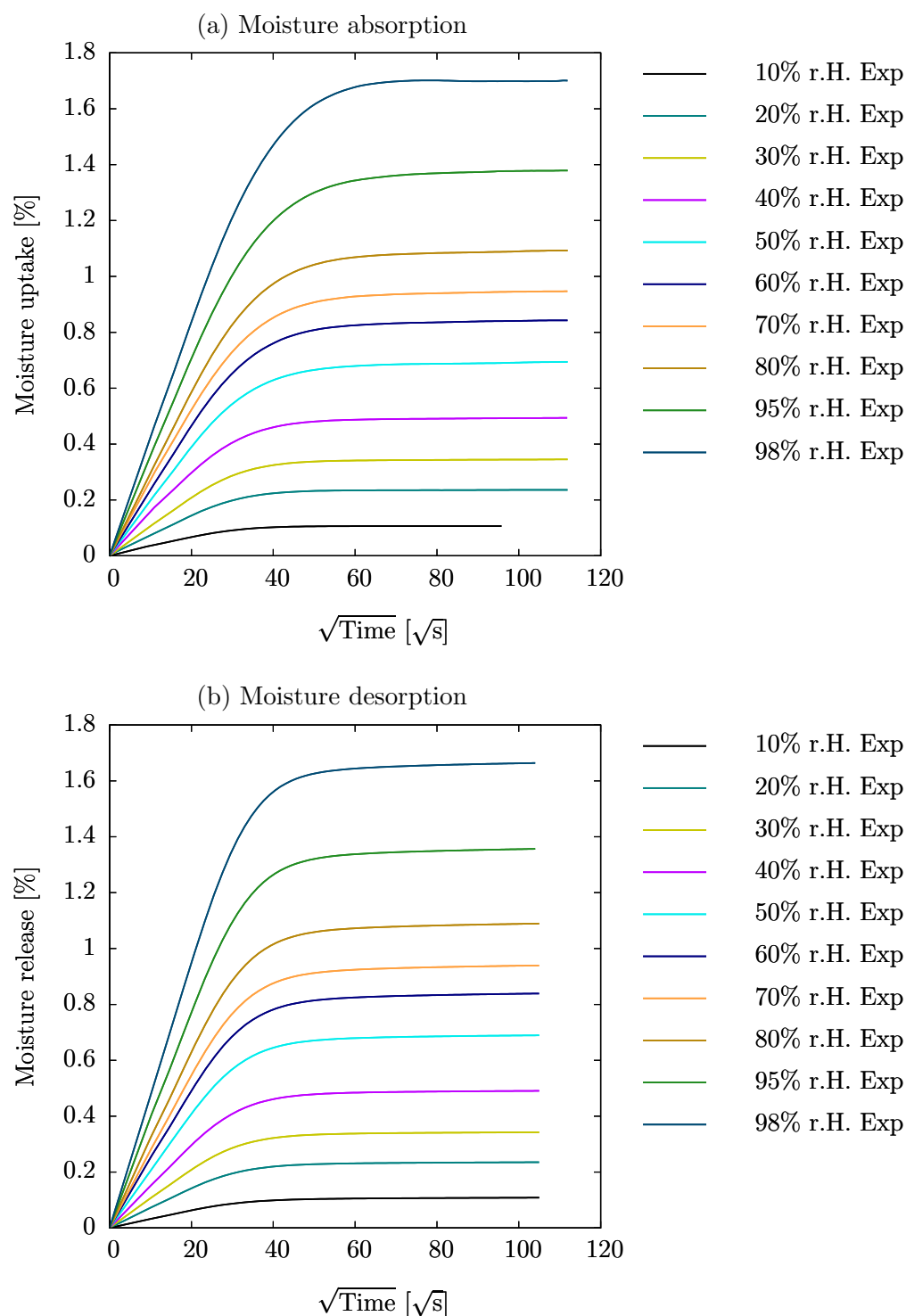


Figure 6.2: Experimental observation of moisture (a) uptake and (b) release by the adhesive-A sample under different ambient conditions at 60°C

different ambient conditions with the relative humidity varying between 0% to 95% at an isothermal condition of 60°C. Table 6.3 lists the equilibrium moisture content $m_\infty(H)\%$ diffused in the sample.

Table 6.3: Equilibrium moisture content absorbed by adhesive-B

$H\%$	10%	30%	50%	80%	95%
$m_\infty(H)\%$	0.97%	1.16%	1.33%	1.56%	1.71%

The moisture equilibrium content $m_\infty(H)\%$ at every relative humid ($H\%$) condition determines the moisture absorption isotherm. Moisture absorption is conducted for different relative humid climates varying between 0% to 95% at 60° C. Absorption isotherms is non-linear, and ranges between 0% and 1.71% are shown in Figure 6.3.

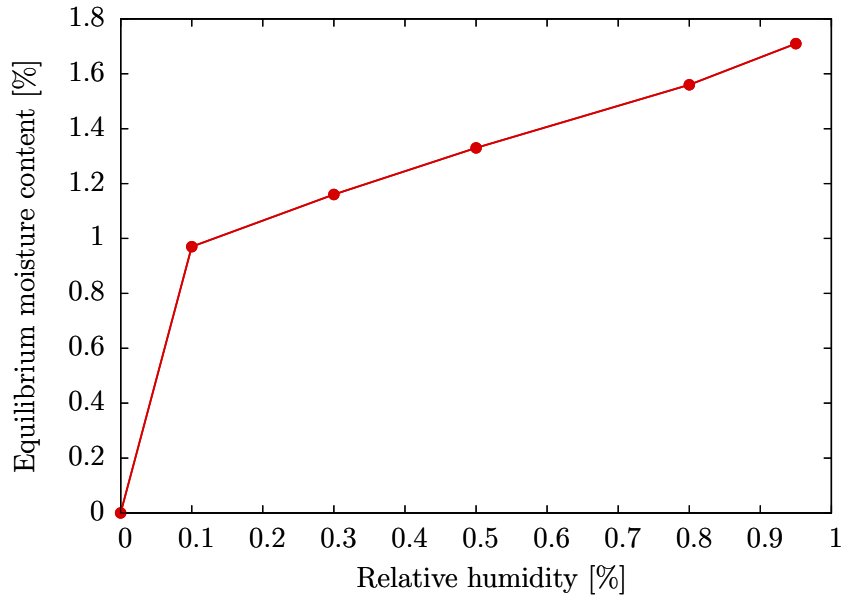


Figure 6.3: Isotherm of moisture diffusion in the crosslinked polyurethane adhesive-B at an isothermal condition 60° C

Further, the moisture desorption by the sample is investigated by placing the samples aged at different humid conditions in a climate chamber with a dry atmosphere. The continuous change in the sample's weight due to the moisture release is recorded to calculate the moisture content released by

the samples. The equilibrium moisture content $m_{-\infty}(H)\%$ released by the samples at $H\%$ humid atmosphere is listed in Table 6.4. The mass released

Table 6.4: Equilibrium moisture content released by adhesive-B

$H\%$	10%	30%	50%	80%	95%
$m_{-\infty}(H)\%$	0.97%	1.16%	1.33%	1.56%	1.71%

by the samples is identical to the moisture absorbed, showing no chemical ageing under the influence of moisture. Figure 6.4a-6.4b shows the changes in the mass of the adhesive-B samples under different humid atmospheres. The time required for the adhesive-B sample to attain equilibrium at 10% humid climatic conditions is larger than the other ambient conditions. Although the equilibrium moisture content is the same in absorption and desorption behaviours, the kinetics of desorption show that the material holds the diffused moisture for a longer time than the time required for the material to saturate, as shown in the Figures 6.4a and 6.4b.

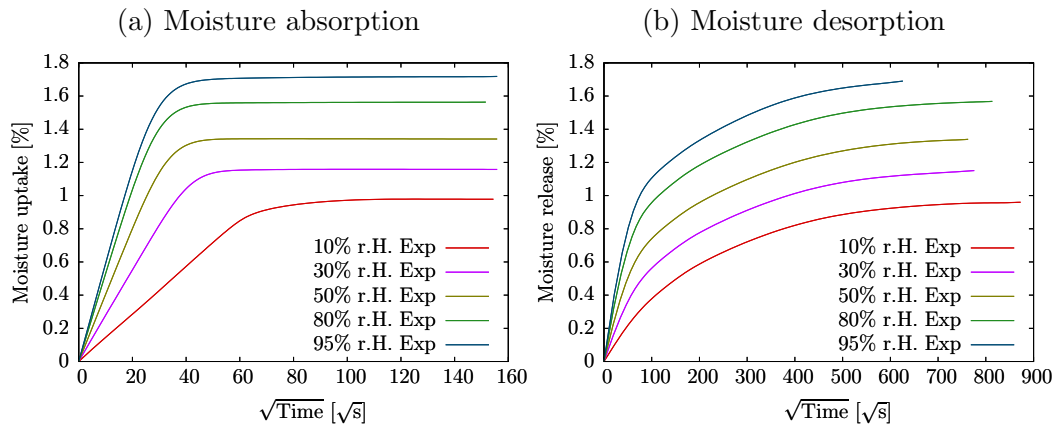


Figure 6.4: Experimental observation of moisture (a) uptake and (b) release by the adhesive-B sample under different ambient conditions at 60°C

Diffusion is generally expressed in terms of the concentration gradient. Hence, unique material properties can be identified irrespective of the boundary value problem. However, moisture absorption and desorption curves are dependent on the boundary value problem in adhesive-B. Higher desorption curves may be because of the moisture condensation in the capillaries of the material, causing the sample to dry at larger times. The other reason for the

higher desorption curve could be because of the slower desorption rate of the impurities added to the material causing the chemical potential to drive the diffusion. Therefore the diffusion parameters are identified individually for the moisture absorption and desorption.

6.2 Langmuir-type diffusion parameters

The Langmuir-type diffusion model is used to investigate anomalous moisture diffusion instead of the traditional Fick's diffusion model¹. The primary aspect of the numerical investigation is to identify the parameters intended to simulate the material behaviour under the applied boundary conditions. To this end, the Nelder-Mead optimisation algorithm [109] is used to identify the diffusion parameters of adhesive-A and adhesive-B.

6.2.1 Diffusion parameters for adhesive-A

The 0.833 mm thick sample is spatially discretised and applied with the boundary conditions for the numerical simulation. The moisture is dif-

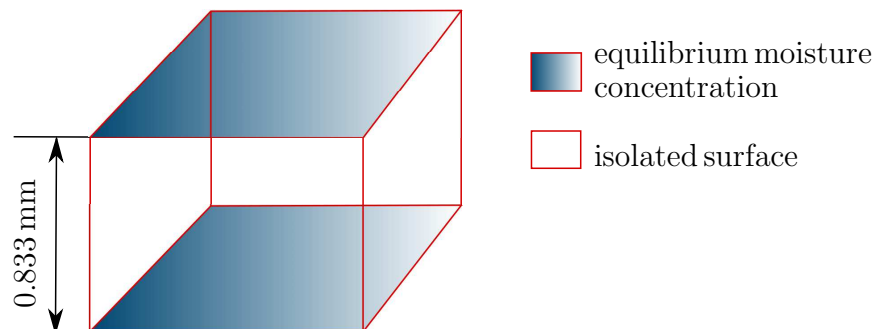


Figure 6.5: Boundary conditions applied to investigate the moisture diffusion.

fused through two surfaces keeping other surfaces insulated to assume one-

¹Fick's diffusion model does not consider the immobile and mobile moisture concentrations. Therefore, the Langmuir-type diffusion model is considered to analyse moisture diffusion. For further details on selecting the Langmuir-type diffusion model, see the chapter 3.1.

dimensional diffusion. Figure 6.5 shows the applied diffusion boundary conditions, where the boundaries along thickness are applied with the equilibrium moisture concentration (see Table 6.1) as the Dirichlet boundary condition and the isolated surfaces are applied with the moisture flux free Neumann boundary conditions to solve the diffusion problem.

In parameter identification, an initial set of arbitrary diffusion parameters D , α , β is initialised to prepare the finite element model. The prepared FE-model is solved for the sample saturated at 98% using a preconditioned direct generalised minimal residual method [126] with the optimization algorithm. The optimization algorithm identifies the optimized diffusion parameters and the diffusion parameters are listed in Table 6.5.

Table 6.5: Identified Langmuir-type diffusion parameters for adhesive-A

D [$\text{mm}^2 \text{s}^{-1}$]	7.925e – 05
α [s^{-1}]	2.727e – 05
β [s^{-1}]	2.247e – 03

The mobile m_f , immobile m_b and total moisture m concentration are obtained as the solution output from the numerical analysis. The experimental and simulation data are compared to validate the material parameters. Figure 6.6 compares the experimental and simulation data measured for the sample saturated under 98% relative humid atmosphere. The comparison curve illustrates that the total moisture concentration calculated from the numerical analysis coincides with the test data. The mobile and immobile moisture concentrations² from the numerical analysis are plotted in blue and green curves. The moisture diffusion follows Fickian behaviour until $18\sqrt{\text{s}}$ where the total and mobile moisture concentrations follow the curve overlapping with the test results. Later increment in the curve is followed by a secondary absorption curve characterised as the immobile moisture concentration.

²Gravimetric experiment can not characterise the diffused moisture into mobile and immobile moisture concentrations. Huácuja-Sanchez et al. [67] have investigated the water diffusion in the polyurethane adhesives, concluding with FT-IR measurements that the moisture concentration diffused in the sample exits in two phases. It is necessary to investigate moisture diffusion with more sophisticated experimental methods like ^2H NMR spectra [140], to measure mobile, immobile moisture concentration and the total moisture concentration.

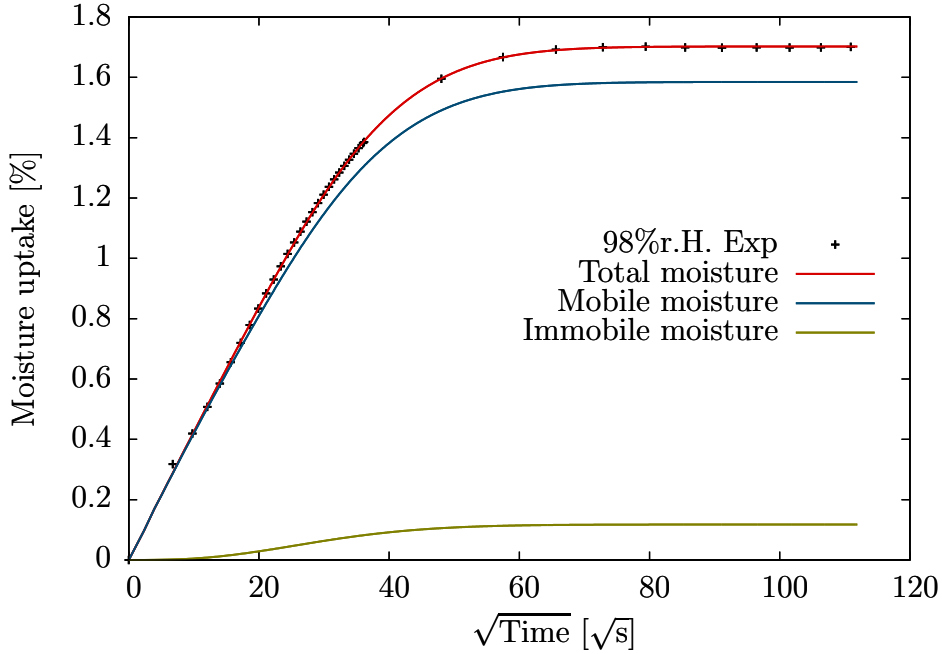


Figure 6.6: Comparison between experimental (Exp) and simulation data of moisture absorption at 60°C with 98% relative humidity in air

The thin sample is investigated for both absorption and desorption of moisture simultaneously with the diffusion parameters listed in Table 6.5. Equilibrium moisture concentration $m_{\infty}(H)\%$ absorbed by the sample saturated at 98% relative humidity listed in Table 6.1 is applied as the boundary condition. Figure 6.7 shows the local moisture distribution along the thickness of the sample at various time intervals until the saturation state is reached. The blue contour in the visualisation plots defines the dry region, and the red contour defines the maximum total moisture concentration with $m = 1.7\%$. Time $t = 0$ s is referred to as a dry sample with the equilibrium moisture concentration applied as the Dirichlet boundary conditions on the boundaries. The moisture diffuses in the sample until the saturation is reached at time $t = 4,925$ s.

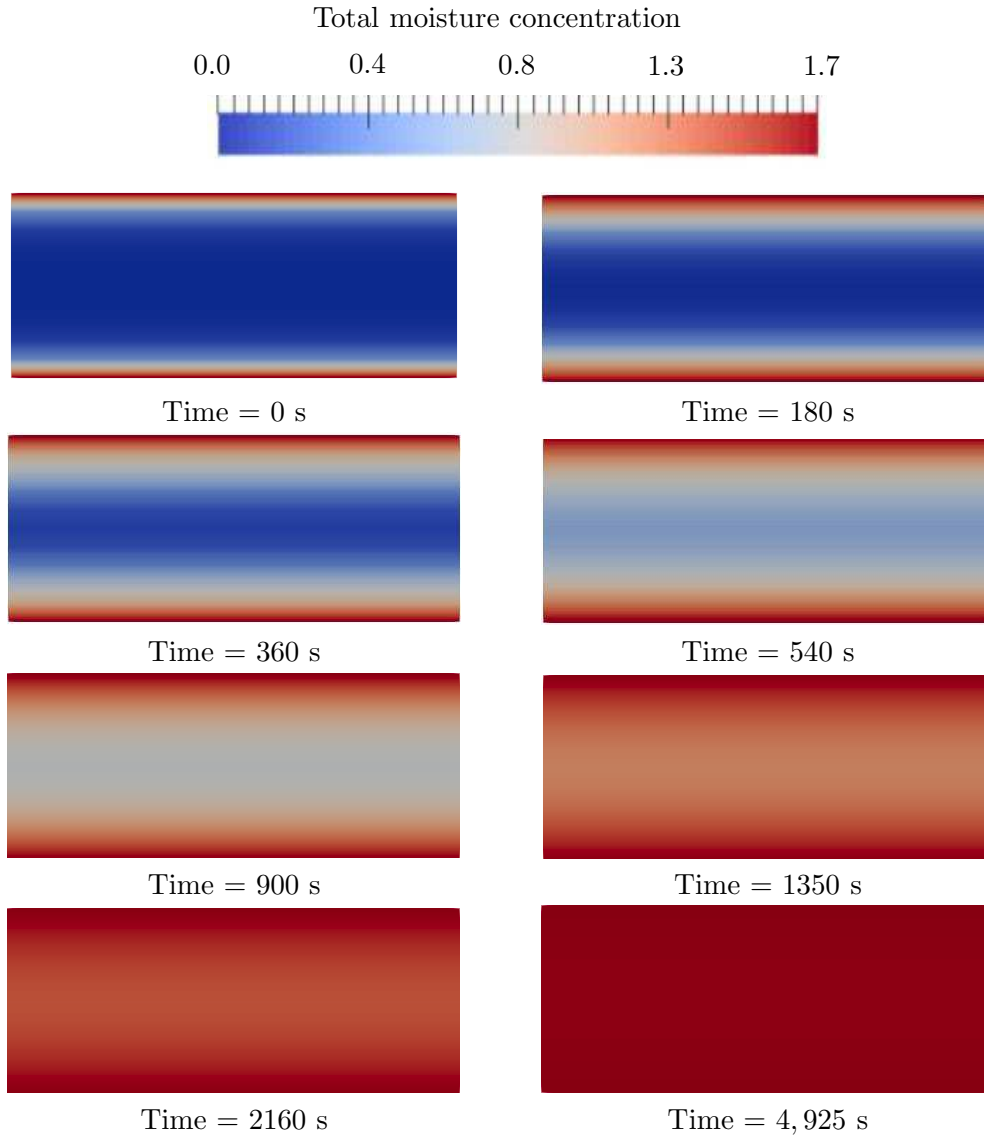


Figure 6.7: Moisture distribution in the sample at different times from the initial state to the state of saturation

Once the sample in the climate chamber reaches equilibrium, the boundary conditions are switched from humid to dry air to record desorption kinetics. These experimental details are incorporated into the finite element model by switching boundary conditions to a dry atmosphere. The top and bottom surfaces of the saturated sample are defined with 0% relative humidity on the surface, and other surfaces are isolated to restrict interaction with surround-

ings, as shown in Figure 6.5. The optimum diffusion material parameters identified for the sample saturated at 98% r.H. listed in Table 6.5 are used in the finite element simulation of the moisture desorption. In Figure 6.8, the

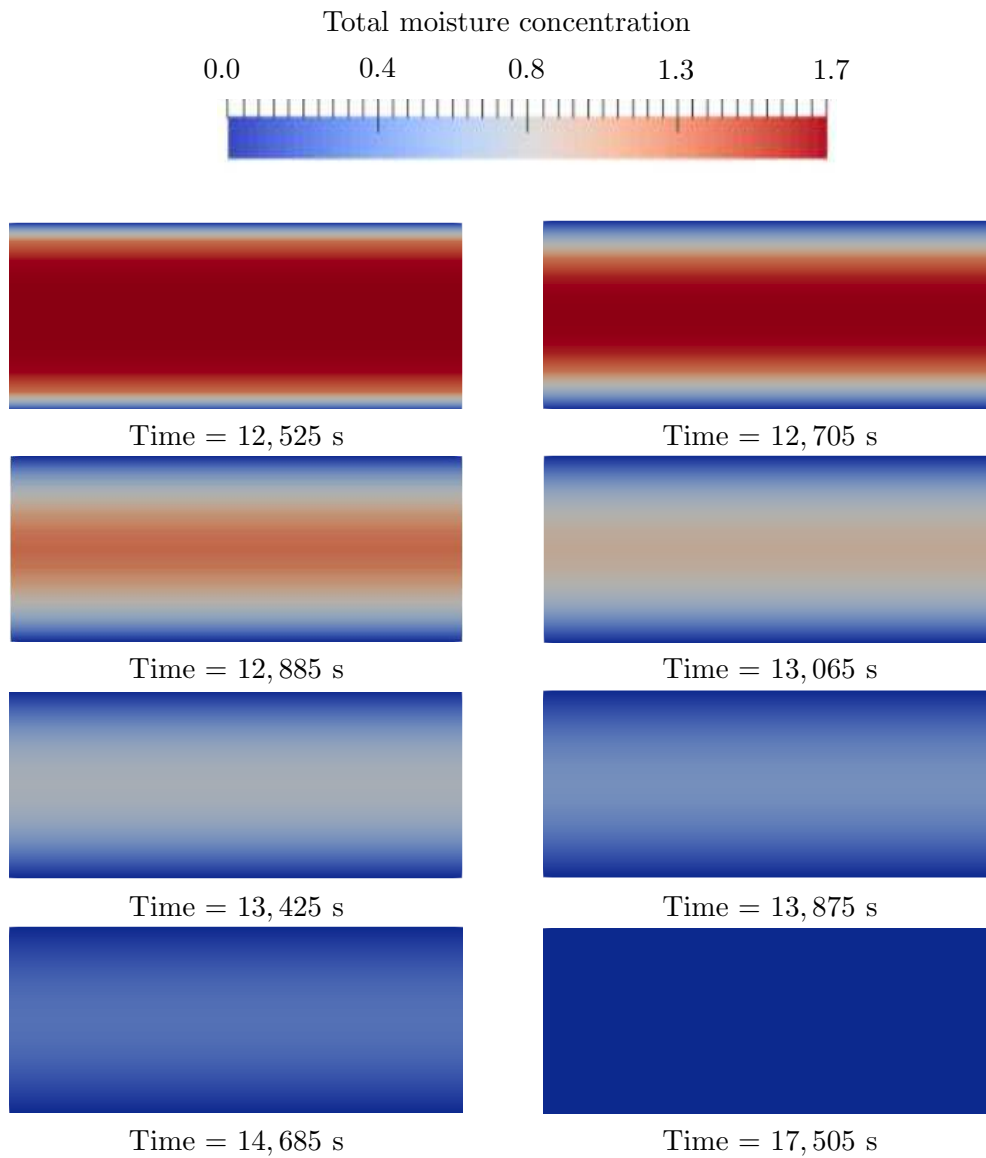


Figure 6.8: Moisture distribution in the sample at different times from the saturation to the dry state.

sample at time $t = 12,525$ s is referred to saturated sample, where the boundary condition is shifted from humid to dry air condition. Due to the shift in the boundary conditions, the sample releases moisture from the boundaries

to the surroundings with time increment until the sample becomes dry at time $t = 17,505$ s.

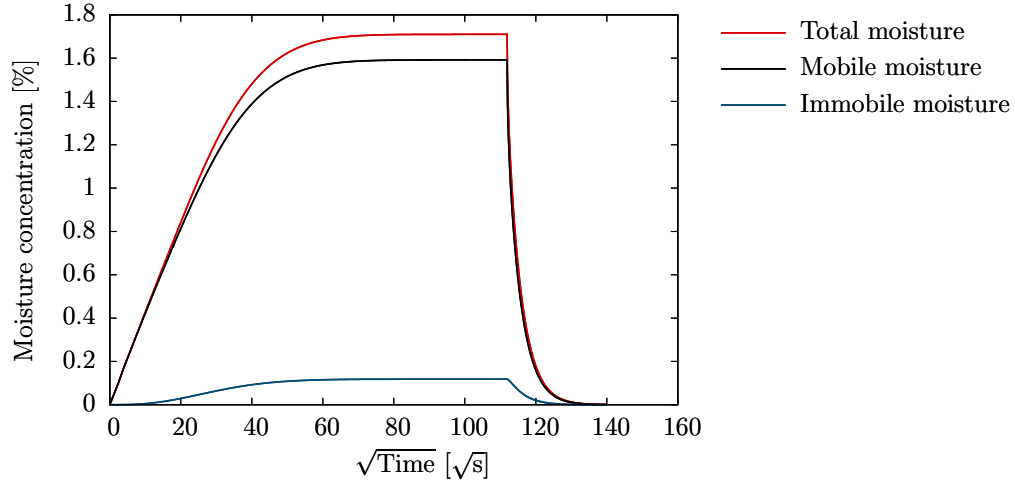


Figure 6.9: Moisture absorption and desorption behaviour in a crosslinked polyurethane adhesives at 60°C with 98% of humid air

Figure 6.9 shows the classic evaluation of moisture transport, where the global moisture concentration is plotted against the square root of time. The sample applied with the absorption boundary conditions reaches saturation at $\sqrt{t} = 86.1 \sqrt{s}$. The moisture concentration at the boundaries is switched from absorption to desorption boundary conditions at time $\sqrt{t} = 111.92 \sqrt{s}$ to investigate moisture release by the sample and the sample is dried at time $\sqrt{t} = 140.07 \sqrt{s}$. The results from the numerical simulation shows that the time required for the sample to reach saturation state is observed to be same³ for the sample to become dry from the saturation state as similar to the diffusion tests performed on the material.

The total moisture concentration is significantly influenced by the immobile moisture concentration leading to the second plateau in the moisture diffusion curves of the polyurethane adhesives as discussed in chapter 3.1.1. Figure 6.9 shows that the influence of the immobile moisture concentration is not large on the total moisture concentration in adhesive-A. Therefore, simple Fick's

³The boundary conditions are shifted from humid to dry state at time $t_{D(0)} = 12,525$ s. This sample becomes dry at time $t_{D(\infty)} = 17,505$ s. The difference between the start time for desorption and the time when the sample is dried $t_{D(0)} - t_{D(\infty)} = 4,980$ s is approximately equal to the time required for the sample to reach saturation $t_{A(\infty)} = 4,925$ s.

law of diffusion can be used to analyse the moisture diffusion in a 0.833 mm thick adhesive-A sample.

A thin sample of 0.833 mm thickness is spatially discretised into a finite element mesh to investigate moisture diffusion at different relative humid conditions. The boundaries of the finite element mesh are applied with the equilibrium moisture content $m_{\infty}(H)\%$ for the selected relative humidity $H\%$ listed in Table 6.1 as boundary conditions. The prepared finite element model is defined with the diffusion parameters listed in Table 6.5.

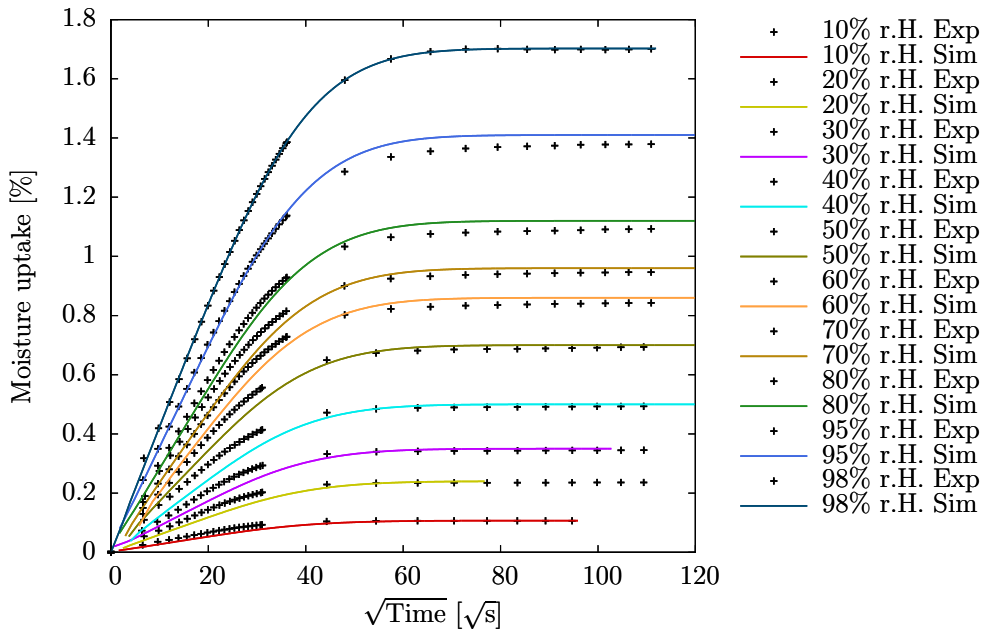


Figure 6.10: Experiment (Exp) and simulation (Sim) comparison of moisture uptake by adhesive-A at different relative humid conditions (r.H.)

The moisture diffusion is evaluated by plotting the moisture uptake against the square root of time. Figure 6.10 shows the comparison between the experimental and the simulation results carried out to understand absorption behaviour with the identified diffusion parameters⁴. These curves show good agreement between the simulation and test results of moisture absorption.

Desorption behaviour by the adhesive-A samples is investigated on the samples saturated at different humid atmospheric conditions varying between 0%

⁴Moisture absorption by the sample saturated at 98% r.H. shown in the Figure 6.10 has already been discussed in the identification of the parameters for adhesive-A sample, see Figure 6.6 on page 76

r.H. to 98% r.H. under an isothermal condition of 60°C. The thin sample of 0.833mm thickness is spatially discretised to define the equilibrium moisture content $m_{-\infty}(H)\%$ listed in Table 6.2 measured for $H\%$ humid condition as the boundary conditions. The diffusion parameters listed in Table 6.5 are used to analyse moisture release by the adhesive-A samples.

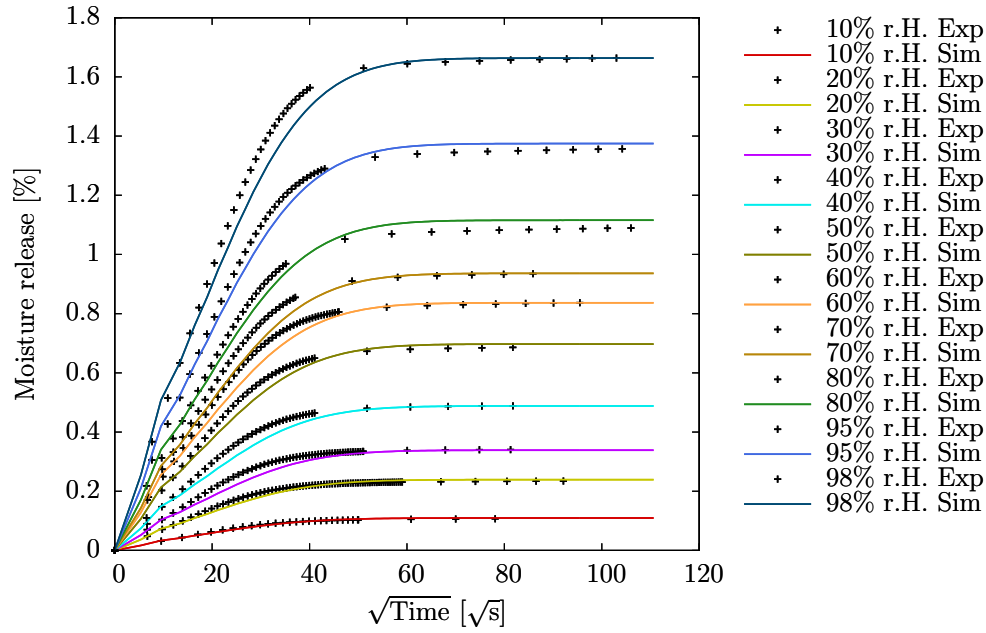


Figure 6.11: Comparison of the experiment (Exp) and the simulation (Sim) of the moisture released by adhesive-A at different relative humid conditions (r.H.)

The simulation results are validated by comparing with the desorption curves measured in gravimetric tests. Figure 6.11 shows the comparison between experimental and simulation results of the moisture release. These curves are in a good agreement validating the diffusion parameters to investigate the moisture desorption.

6.2.2 Diffusion parameters for adhesive-B

A finite element simulation of a 0.15 mm thick adhesive-B sample is investigated to identify material parameters. The sample is spatially discretised

to apply the equilibrium moisture content of 95% relative humidity as listed in Table 6.3 as the Dirichlet boundary conditions. The other surfaces are isolated to assume a good approximation of one-dimensional diffusion. The optimisation algorithm is employed to identify material parameters. The optimum parameters are identified by minimising the error between the simulation and experimental results, as summarised in Table 6.6.

Table 6.6: Parameters of Langmuir-type diffusion identified for adhesive-B

D [$\text{mm}^2 \text{s}^{-1}$]	$6.03\text{e} - 06$
α [s^{-1}]	$6.95\text{e} - 01$
β [s^{-1}]	$8.16\text{e} - 00$

The numerical analysis is performed for different humid conditions using the diffusion parameters listed in Table 6.6. Figure 6.12 shows the comparison of experimental and simulation results carried out using the diffusion parameters. The samples saturated at lower moisture concentrations do not fit with experimental data. This anomaly in the diffusion behaviour is due to the non-linear isotherm of diffusion, as shown in Figure 6.3.

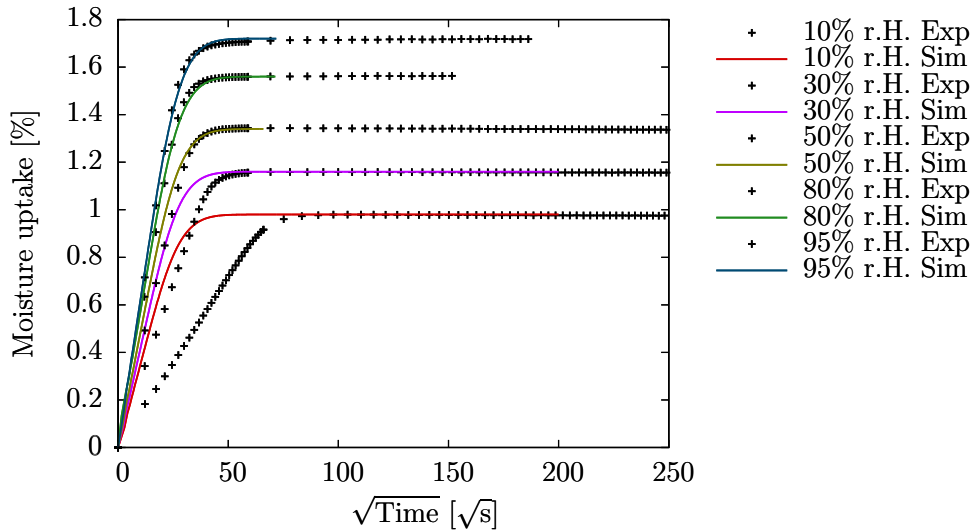


Figure 6.12: Experiment (Exp) and simulation (Sim) comparison of the moisture absorption by adhesive-B different relative humid conditions (r.H.)

6.2.3 Effective diffusion parameters

In traditional diffusion theories, the diffusion coefficient is assumed to be a constant material property irrespective of the boundary value problem. However, there are many reaction-diffusion systems with the diffusion parameters dependent on the boundary value [41, 133]. In here, the moisture diffusion in the adhesive-B is solved using the Langmuir-type diffusion equation with the effective diffusion parameters. These effective diffusion parameters are derived as the product of diffusion parameters and an exponential function of relative humidity as follows

$$D_{\text{eff}} = D_0 e^{-\frac{(\chi-A_1)^2}{2B_1^2}}; \alpha_{\text{eff}} = \alpha_0 e^{-\frac{(\chi-A_2)^2}{2B_2^2}}; \beta_{\text{eff}} = \beta_0 e^{-\frac{(\chi-A_3)^2}{2B_3^2}}, \quad (6.3)$$

D_{eff} , α_{eff} and β_{eff} are the effective diffusion parameters calculated from the optimal diffusion parameters D_0 , α_0 and β_0 identified for the sample saturated at the maximum relative humid atmosphere and χ is the relative humidity calculated as

$$\chi = \frac{m_{\infty}(H\%)}{m_{\infty}(95\%)}. \quad (6.4)$$

$m_{\infty}(H\%)$ is the equilibrium moisture content for $H\%$ of relative humidity in the atmosphere, and $m_{\infty}(95\%)$ is the equilibrium moisture content of the sample saturated at 95% r.H. A_1 , A_2 , A_3 , and B_1 , B_2 , B_3 are the empirical constants used to calculate the effective diffusion parameters. The Langmuir-type diffusion model based on effective material parameters is reformulated using equations (3.1) and (3.2) as

$$\begin{aligned} \dot{m} &= D_0 e^{-\frac{(\chi-A_1)^2}{2B_1^2}} \operatorname{div}(\operatorname{grad}(m - m_b)), \\ \dot{m}_b &= \alpha_0 e^{-\frac{(\chi-A_2)^2}{2B_2^2}} m_f - \beta_0 e^{-\frac{(\chi-A_3)^2}{2B_3^2}} m_b. \end{aligned} \quad (6.5)$$

In the identification of the effective diffusion parameters, the parameters listed in Table 6.6 for a saturated sample at 95% humid atmosphere are considered as the diffusion parameters (D_0 , α_0 , β_0) and χ is calculated using the equilibrium moisture content listed in Table 6.3 with equation (6.4). The empirical constants are identified on the sample exposed to 10% r.H. using the optimization algorithm and are listed in the Table 6.7.

The effective diffusion parameters are used to analyse the moisture absorption

Table 6.7: Empirical constants of the effective diffusion parameters in the moisture absorption

A_1	0.87	B_1	0.18
A_2	0.79	B_2	0.026
A_3	0.80	B_3	0.028

for different humidities in the air at an isothermal condition of 60°C. The simulation and experimental results are compared to validate the effective diffusion parameters. Figure 6.13 shows the comparison of the results and the comparison shows a good approximation between the experimental and simulation results.

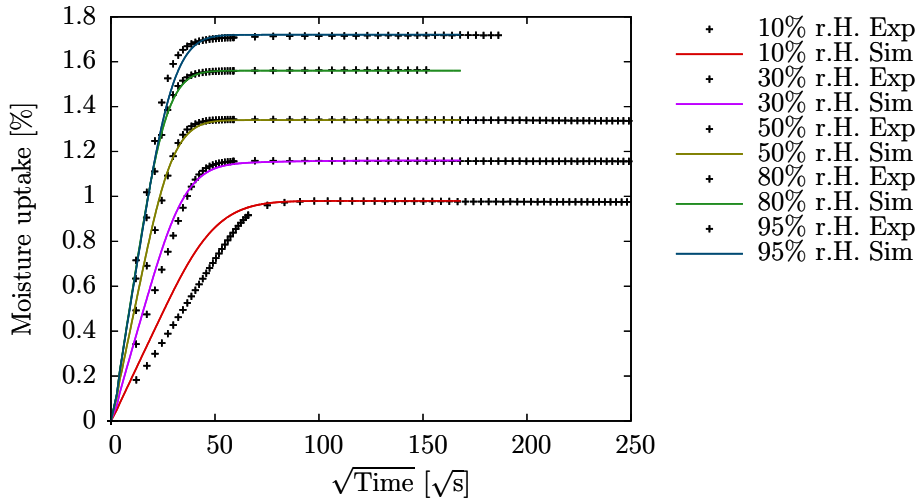


Figure 6.13: Experimental (Exp) and simulation (Sim) comparison of moisture absorption in adhesive-B at different relative humid conditions (r.H.)

Effective diffusion parameters are identified to analyse moisture desorption in adhesive-B. The moisture desorption parameters are identified for the sample saturated at 95% r.H. using the optimisation algorithm and are used to identify the empirical constants. The desorption parameters are listed in Table 6.8 for the sample saturated at 95% r.H. to reach a dry state.

The test data of the sample saturated at 10% r.H. is used to identify the empirical constants with the optimisation algorithm. The diffusion parameters listed in Table 6.8 and χ calculated with the equation (6.4) were used to cal-

Table 6.8: Identified Langmuir diffusion parameters of adhesive-B

D [$\text{mm}^2 \text{s}^{-1}$]	$7.49\text{E} - 06$
α [s^{-1}]	$1.36\text{E} - 01$
β [s^{-1}]	$9.17\text{E} - 04$

culate the effective diffusion parameters. The optimum empirical constants identified with the optimization algorithm are listed in Table 6.9

Table 6.9: Empirical constants of the effective diffusion parameters in the moisture desorption

A_1	3.29	B_1	0.88
A_2	2.05	B_2	0.65
A_3	–	B_3	–

The effective diffusion parameters are used to analyse the moisture desorption that were saturated at different relative humidities. The simulation and the experimental data are compared to validate the effective diffusion parameters. Figure 6.14 shows a good approximation between the test and simulation results validating the effective diffusion parameters for moisture desorption.

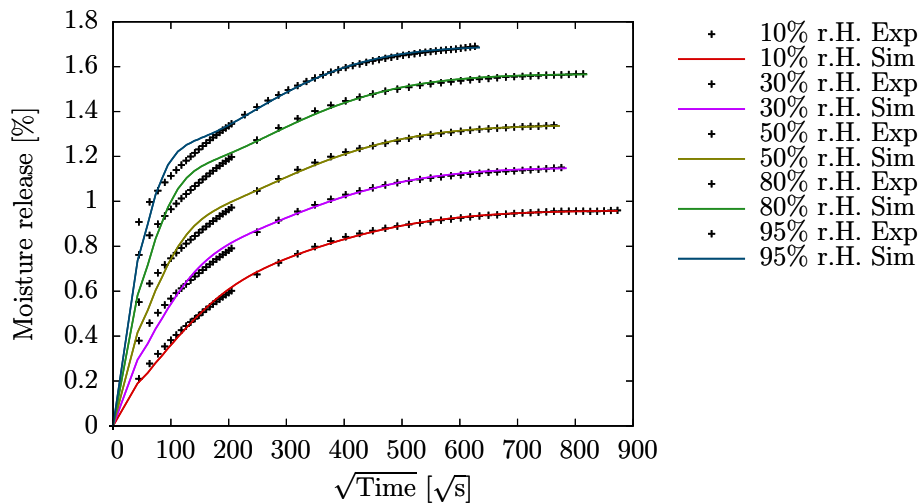


Figure 6.14: Experiment (Exp) and simulation (Sim) comparison of moisture desorption by adhesive-B at various relative humid conditions (r.H.)

7

Parameter identification of the ageing mechanical properties

This chapter discusses the numerical analysis of the ageing in polyurethane adhesives under the moisture influence. To this end, the effect of the moisture concentration on the viscoelastic behaviour is investigated by conducting the uniaxial tensile tests on the tailored tensile test samples at Lehrstuhl für Adhäsion & Interphasen in Polymeren, Universität des Saarlandes. These tailored tensile test samples are aged under different humid atmospheric conditions, and a tensile load is applied to the aged samples to measure stretch and stresses. Finally, tear tests are conducted on the angular samples aged under different humid atmospheric conditions at Fraunhofer-Institut für Fertigungstechnik und Angewandte Materialforschung to investigate the fracture toughness. The viscoelastic parameters of the aged samples are identified from the curve fitting process, and these parameters are used in the damage simulation using the phase-field damage model. The critical energy release rate of the material required for the phase-field damage model is identified by fitting simulation and tear test data.

7.1 Ageing of mechanical properties

The mechanical behaviour of the adhesive-A samples is significantly influenced by moisture diffusion. The uniaxial tensile test are used to investigate the influence of the moisture diffusion on the viscoelastic behaviour (see chapter 2 of IGF-Project 19730 N, Wulf et al. [154]). The fracture will likely start at any position along the cross-section in the classical tensile specimens with constant cross-section, making it difficult to measure strains locally at the observation window. Therefore, a tailored specimen is manufactured with a smaller cross-section at the centre of the sample. Tailored samples do not experience either pre-stress or pre-strain in the manufacturing process. Figure 7.1 shows the geometry of the tailored sample with a thickness of 2 mm used for the experimental investigation with the uniaxial tensile test.

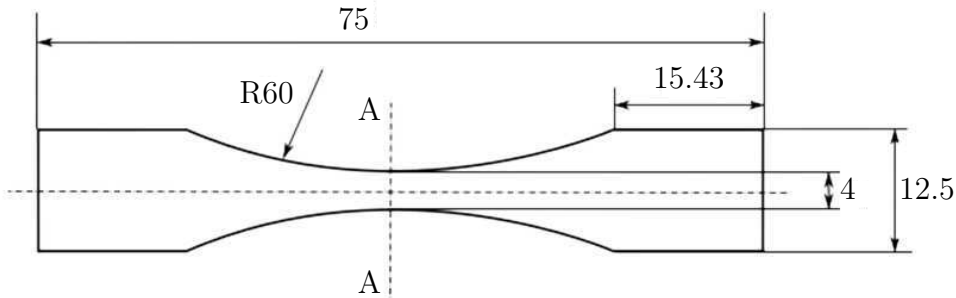


Figure 7.1: Tailored tensile test samples with a necked cross-section at the centre of the sample: all dimensions are in millimetres

Aged samples of adhesive-A are prepared by placing post-cured samples in a climatic chamber with a humid atmosphere until equilibrium. Four batches of aged samples are prepared under four relative humid states at an isothermal condition of 60°C . The uniaxial tensile test of these aged samples is conducted at a strain rate of 0.0005 s^{-1} . The stress-stretch data from the experimental investigation of aged samples with homogenous moisture distribution at equilibrium are used to identify the material parameters of the finite-strain viscoelastic material model. The parameters of the samples aged at different relative humid atmospheric conditions are used to develop functionally depend stiffness parameters on the local moisture concentration.

In the tensile test conducted on the aged samples, the strains are measured

locally at 2 mm from the centre of the sample. Therefore, the 2 mm span from the centre of the tailored sample is discretised into finite element mesh for the numerical simulation. The bottom surface of the finite element mesh is applied with the fixed support boundary conditions, and the top surface is applied with the displacement boundary conditions to impose stretch due to tension. In modelling the viscoelastic behaviour, four Maxwell elements are connected in parallel to the basic elastic spring component. c_{10} , c_{20} and c_{30} are the material parameters of the basic elasticity and the inelastic parameters of $j = 1, 2, \dots, 4$ Maxwell elements are represented with c_{10j} . The associated relaxation times of the Maxwell elements are chosen to be constant. The viscoelastic parameters identified with the optimization algorithm are summarised in Table 7.1.

Table 7.1: Material parameters of the finite-strain viscoelastic material model identified for the different relative humid atmospheres at 60° C

Material parameters of finite-strain viscoelastic model						
		Relaxation times [s]	0% r.H.	29% r.H.	67% r.H.	100% r.H.
Equilibrium	c_{10} [MPa]		9.886	7.886	7.196	7.072
	c_{20} [MPa]		-1.414	-1.357	-1.122	-1.128
	c_{30} [MPa]		3.214	1.443	0.918	0.872
	D [MPa]		0.306	0.244	0.241	0.314
Non-equilibrium	c_{101} [MPa]	0.5	4.886	2.886	2.296	2.172
	c_{102} [MPa]	10	0.886	0.231	0.139	0.107
	c_{103} [MPa]	100	0.055	0.017	0.014	0.011
	c_{104} [MPa]	1000	0.005	0.003	0.002	0.001

The corresponding stress-stretch data from the uniaxial tension tests are compared with simulation data obtained from the optimum material parameters. Figure 7.2 shows the comparison between the experiment and the simulation data with the standard deviation as an error bar. The tension test data plotted in the comparison corresponds to the mean values calculated from the test series consisting of five samples for aged samples at individual humid

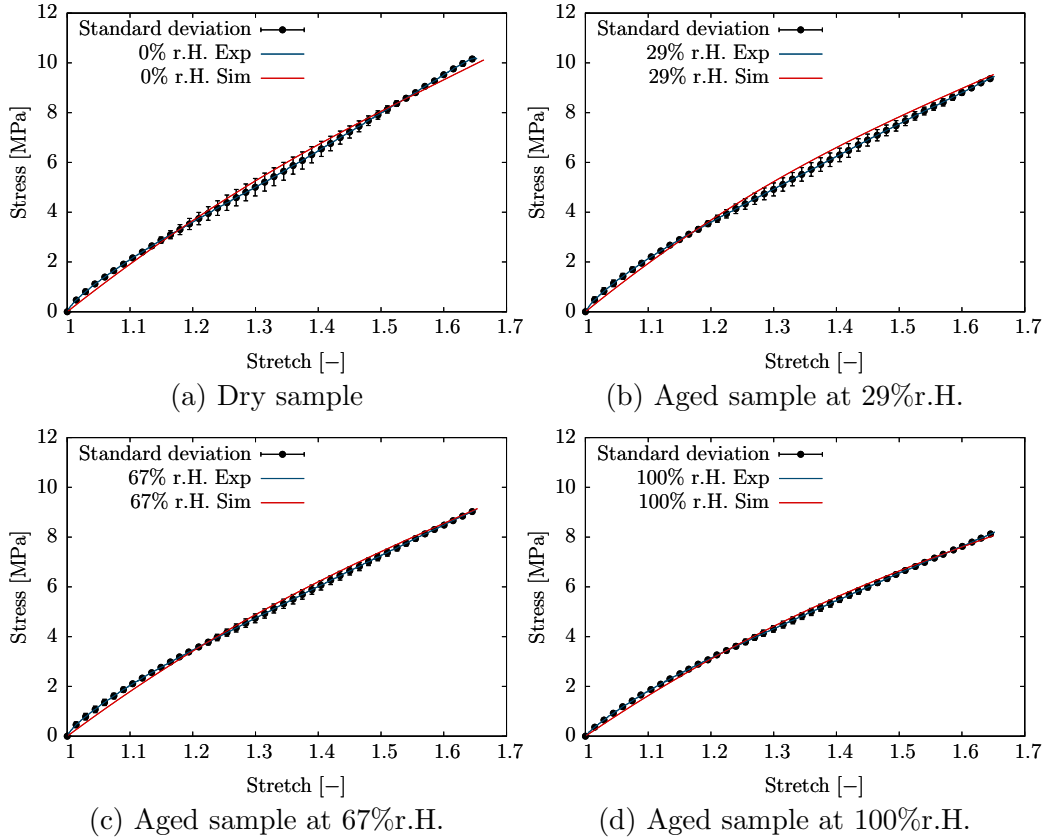


Figure 7.2: Stress - stretch data from uniaxial tensile tests of aged adhesive-A samples with homogeneous moisture distribution performed at 60°C with a strain rate of 0.0005 s^{-1}

climatic condition. The standard deviation in the form of the error bar indicates that the problem is well-posed and sufficient for further investigation of tensile behaviour under a higher strain rate.

The material parameters identified for a lower strain rate of 0.0005 s^{-1} listed in Table 7.1 are used to investigate tensile behaviour under a higher strain rate of 0.05 s^{-1} . The aged specimen's stress paths for the applied strain rate are analysed from the stress-stretch diagram. Figure 7.3 compares the simulation and the uniaxial tensile test data of the dry and aged samples. The experimental data plotted in Figure 7.3 correspond to the mean values calculated from the test series consisting of five sample for aged samples at individual humid conditions. The stresses in the material increase with an increase in the strain rate due to an increase in the non-equilibrium stress because of the viscoelastic behaviour. Although the standard deviation in-

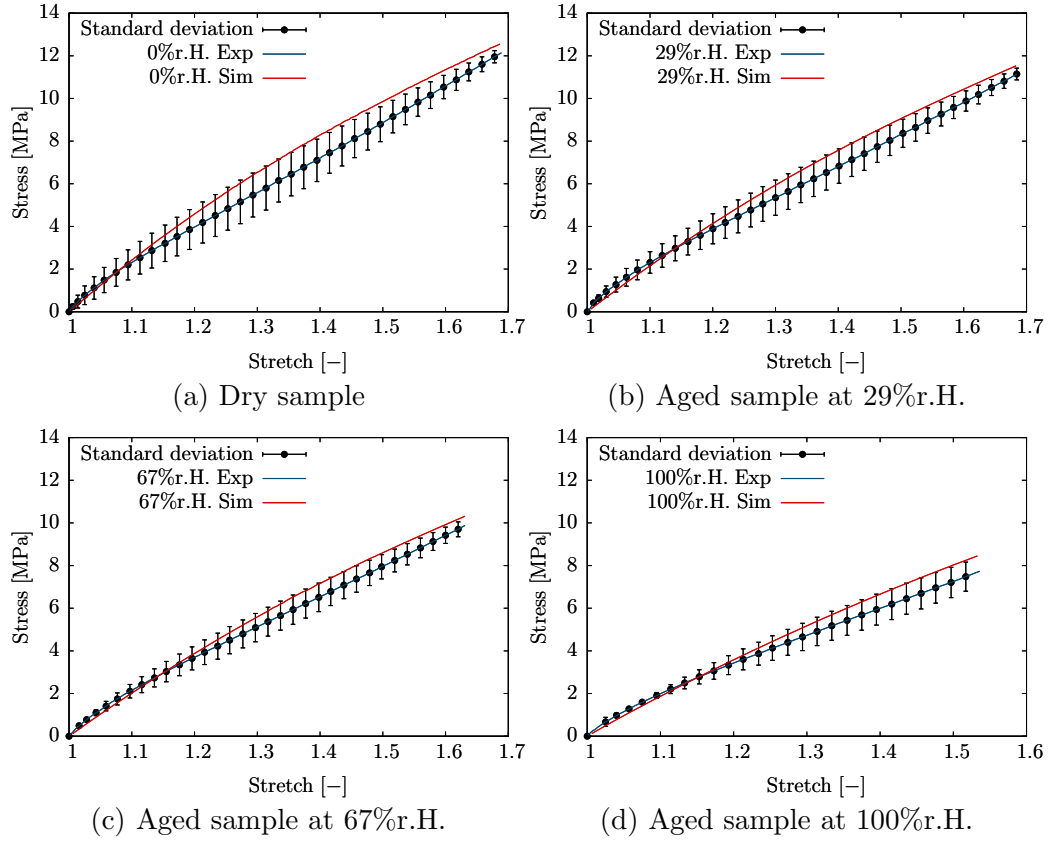


Figure 7.3: Stress - stretch data of aged adhesive-A samples with homogeneous moisture distribution performed at 60°C with a strain rate of 0.05 s^{-1}

creases between the simulation and the experimental data, the simulation results are still agreeable using the material parameters listed in Table 7.1 with a maximum error of 8.5% seen in the dry sample.

The optimal material parameters listed in Table 7.1 are used to analyse viscoelastic behaviour for lower and higher strain rates. The standard deviation between the experimental and simulation results are maximum of 8.5% for higher strain rates and a minimum of less than 2% for lower strain rates. Even with the increasing deviation under the larger strain rates, the reproducibility of the viscoelasticity is still agreeable. Hence, the identified stiffness parameters of the finite-strain viscoelastic material model can be used to identify the moisture-dependent stiffness parameters.

7.1.1 Parameter identification for coupled formulation

The experimental investigation shows that the stiffness parameters decay with an increase in moisture concentration (see Table 7.1). Therefore, moisture-dependent stiffness parameters are considered to enable a geometry-independent description. The decay in the material stiffness is calculated as the function of the local moisture concentration through interpolation. The associated relaxation times of the Maxwell elements are chosen to be constant. The interpolation of stiffness parameters follows

$$\mu(m) = f(m) \mu^{\text{dry}} + (1 - f(m)) \mu^{\text{sat}}. \quad (7.1)$$

$\mu(m)$ are the stiffness parameters of the finite-strain viscoelastic model calculated at the integration points. The moisture-dependent stiffness parameters of the equilibrium element are represented with $c_{10}(m)$, $c_{20}(m)$ and $c_{30}(m)$ and the non-equilibrium elements of $j = 1, 2, \dots, 4$ Maxwell element is represented with $c_{10j}(m)$. μ^{dry} and μ^{sat} are the stiffness parameters of the dry and the saturated samples listed in Table 7.1. $f(m)$ is a function of the moisture

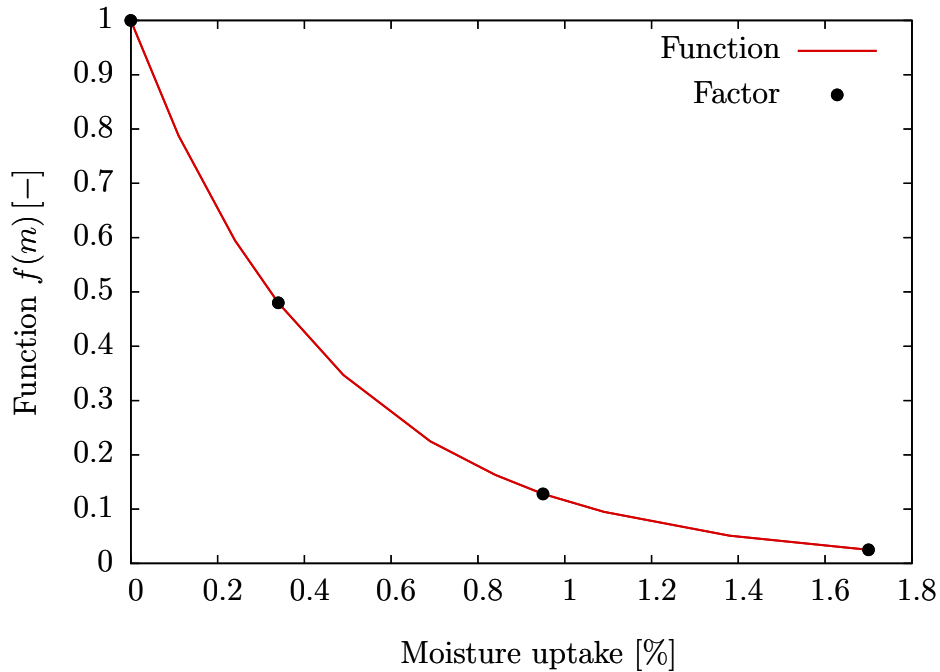


Figure 7.4: Exponential decay function to interpolate the stiffness parameters concentration used to interpolate the stiffness parameters and formulated

using an exponential function

$$f(m) = e^{-\Lambda m} \text{ where } 1 \leq f(m) \lesssim 0, \quad (7.2)$$

where $\Lambda = 3.93$ is a parameter of the coupling function $f(m)$. The coupling parameter Λ is determined from the individual material parameters of the volumetric, equilibrium and non-equilibrium parts. Figure 7.4 shows the evolution of the coupling function $f(m)$ with an increase in the local moisture concentration.

7.1.2 Investigation of the coupled problem

The coupled formulation is validated by comparing test data of dry and saturated samples with the simulation results of a tailored sample with inhomogeneous moisture concentration. The aged tailored tensile finite element model with inhomogeneous moisture is prepared by applying 98% diffusion boundary conditions for different times. The equilibrium mois-

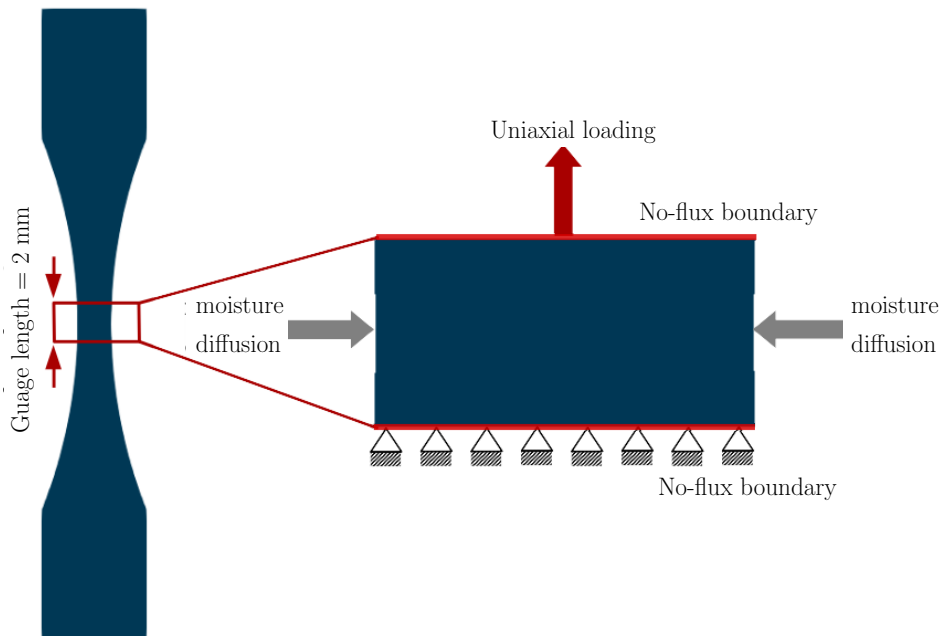


Figure 7.5: Left and right faces of 2 mm wide cross-section of the tailored tensile sample is subject to moisture diffusion for time t s with no-flux boundaries and then the sample is uniaxially loaded with a strain rate of 0.0005 s^{-1}

ture content $m_\infty(H) = 1.70\%$ is applied as the diffusion boundary conditions to prepare finite element models of the aged samples for time $t = 4000$ s, 10000 s, 15000 s, and 60000 s. 2 mm cross-section from the centre of the tailored sample is selected to numerically investigate the tensile behaviour and the simulation results are compared with the uniaxial tensile tests. Figure 7.5 shows the schematic representation of the applied boundary conditions to investigate the influence of the inhomogeneous moisture distribution on the viscoelastic behaviour. The coupled formulation is solved using the staggered method, where the diffusion problem is solved in the first step, and the influence of the local moisture concentration is superimposed on the viscoelastic behaviour in the second step.

The Langmuir-type diffusion parameters listed in Table 6.5 are used to investigate moisture diffusion for 98% relative humid conditions. Figure 7.6

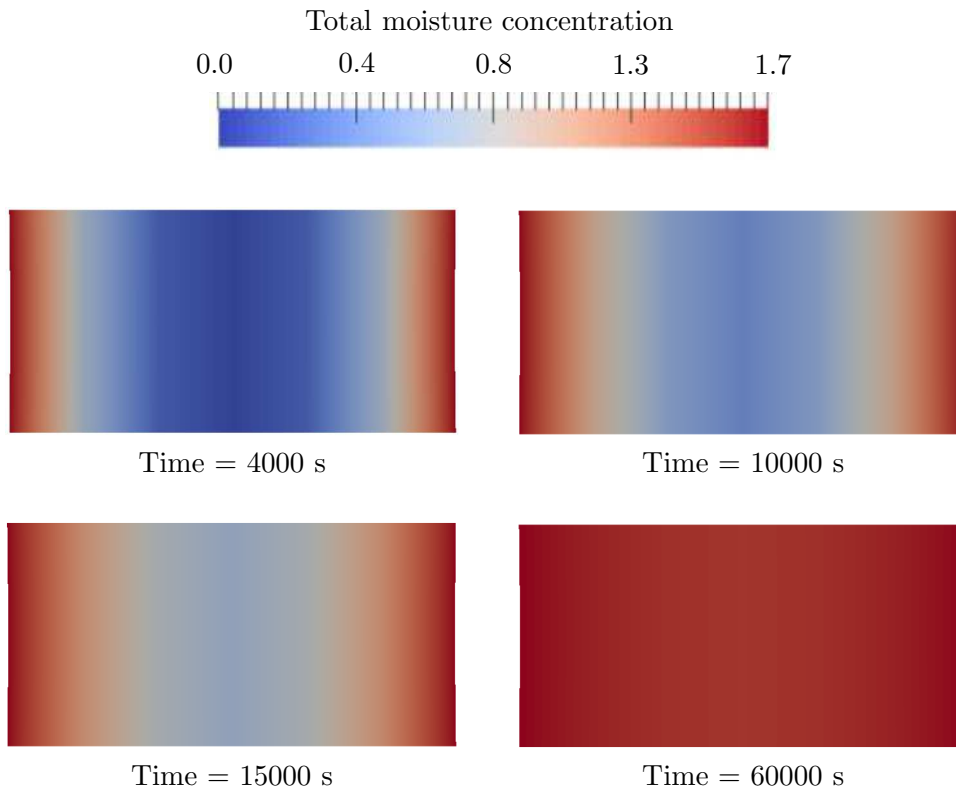


Figure 7.6: Moisture distribution in the tailored tension sample aged for different times

shows the moisture distribution in the spatial domain of the sample at dif-

ferent ageing times. Figure 7.7 compares the total moisture concentration profiles measured along the direction of moisture diffusion at the centre of the samples. It can be interpreted from the curves that the sample reaches saturation at time $t = 60,000$ s realising a homogeneous moisture distribution. In comparison, the moisture distribution is inhomogeneous with $0 < m < 1.7$ in the sample simulated for smaller time periods.

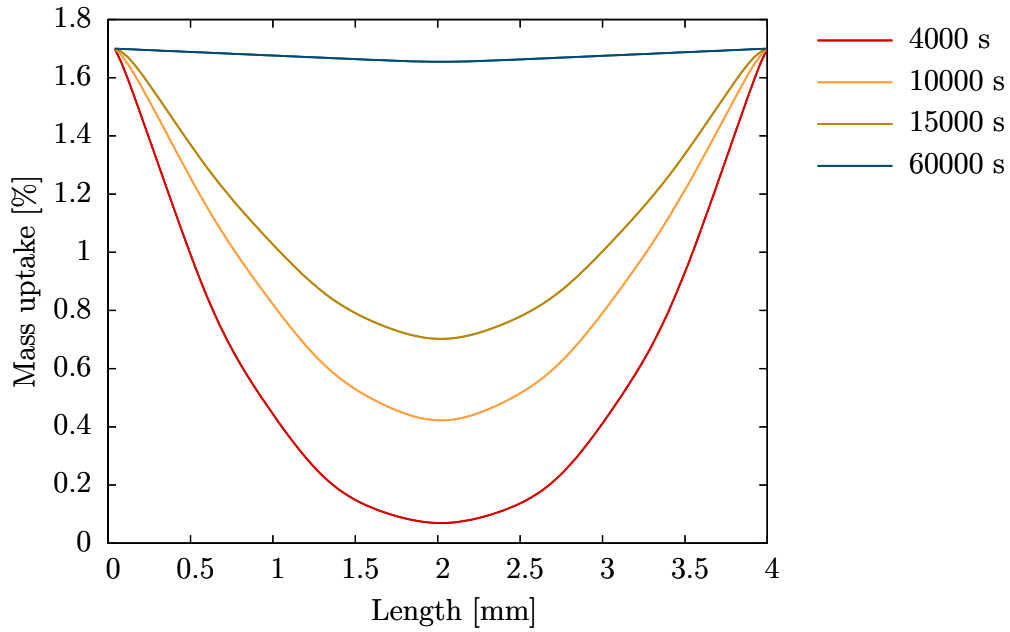


Figure 7.7: Distribution of moisture over the cross-section of the adhesive sample determined by simulation at different times

The tensile behaviour of the aged sample with inhomogeneous moisture distribution is investigated for a strain rate of 0.0005 s^{-1} . The viscoelastic parameters listed in Table 7.1 are used to interpolate the stiffness parameters due to the inhomogeneous moisture distribution. The local stiffness parameters are interpolated from the dry and the saturated properties using the equation (7.1). The stretch vs stress curves from the simulation results is compared with the tensile test data of the dry sample (0% r.H.) and the sample saturated at 100% relative humid atmosphere. It is evident from the curves that the stress for a given stretch reduces with an increase in local moisture concentration. The sample saturates at time $t = 60,000$ s, and the stress-stretch curve is shown in green colour coincides with the uniaxial tensile test results of the saturated sample at 100% r.H. humid climatic condition in blue. The stress-stretch curves of samples with inhomogeneous moisture

distribution obtained for time $t = 4000$ s, 10000 s, and 15000 s lie between the experimental data of the dry and saturated samples.

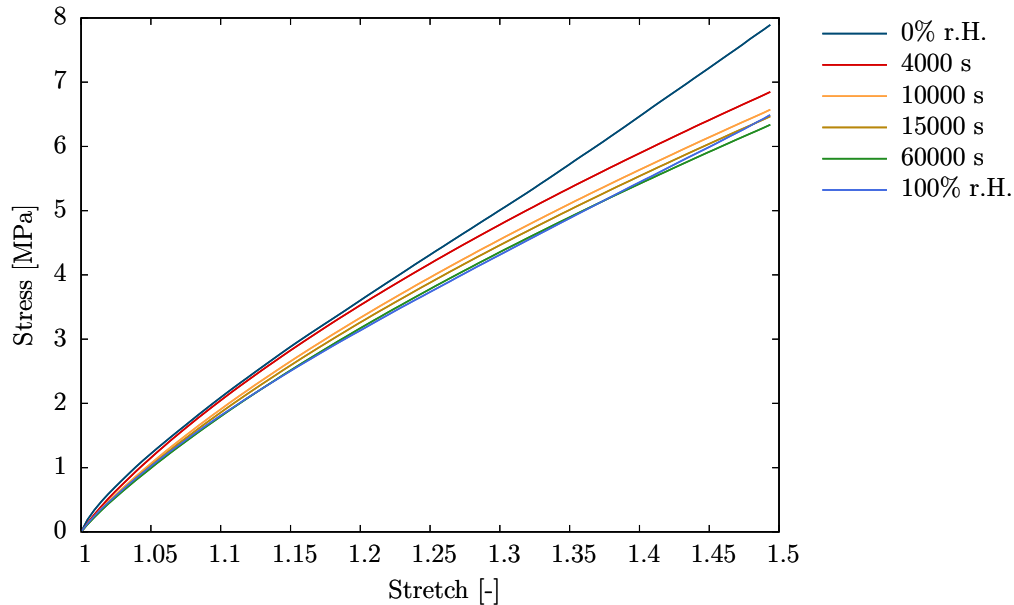


Figure 7.8: Comparison of the stress-stretch curves of the samples with inhomogeneous moisture distribution with dry and saturated samples at 100% relative humidity in climate

7.2 Phase-field damage parameters

Angular specimens with the geometry proposed in DIN ISO 34-1 (shown in Figure 7.9) were prepared for adhesive-A with a thickness of 2 mm to perform the tear test. An initial crack of 9.13 mm length was made at the notch of the specimen to investigate the tear strength. Aged samples are prepared to investigate the moisture influence on the tear strength of the material. The aged samples of adhesive-A are prepared by placing post-cured samples in a climatic chamber with humid air until saturation. These aged samples are prepared at four different humidity conditions at 60° C.

The test sample is clamped on both ends at approximately 22 mm and stretched until the sample fails. A cross-head displacement measurement

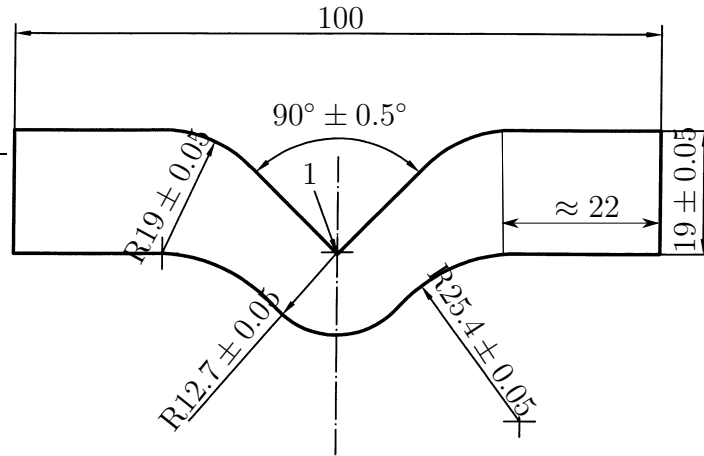


Figure 7.9: Geometry of the angle sample based on DIN ISO 34-1: all dimensions are in millimetres

is adequate to define the displacement boundary conditions on the free ends of the finite element model. The finite element model is prepared with a three-dimensional hexahedral mesh refined at the transition zone. The cross-section at the notch of the sample is the transition zone where the crack initiates and propagates until failure. The mesh is refined at the transition zone following the mesh refinement condition proposed by Miehe et al. [103] (see Equation (4.44)). The FE-mesh of the angular specimen follows the mesh

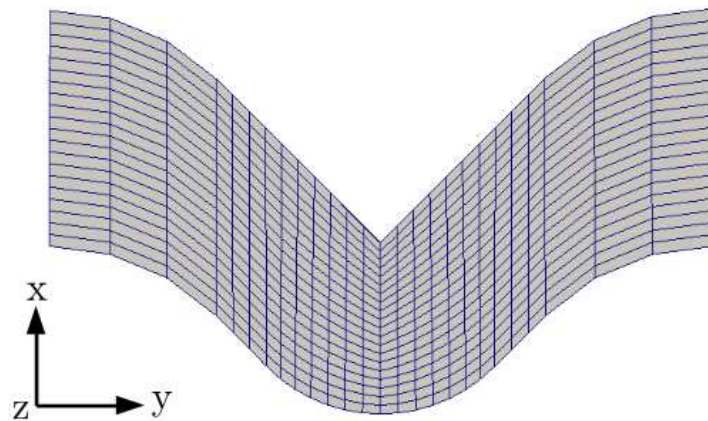


Figure 7.10: FE mesh of the angular sample discretised into finite elements with refined mesh at the transition zone in the centre of the sample.

sensitivity study condition between mesh size h and initial crack length ℓ_f , so that the regularised crack surface $\Gamma(\phi)$ is resolved in the finite element

approximation. Following the mesh sensitivity study as discussed in chapter 4.6, the mesh size of $h = 1.23$ mm is maintained at the transition zone for a length-scale parameter of $\ell_f = 9.31$ mm. Figure 7.10 shows the finite element mesh used for the numerical fracture simulation using the phase-field method.

In the experimental investigation, the free ends of the angular specimen are stretched at a constant strain rate until the sample fails. Therefore, the free ends of the finite element model are applied with fixed boundary conditions in the $-x$ and $-z$ translational degree of freedom and the displacement boundary conditions $u_y = 0.011$ mm are applied in the $-y$ direction. Finally, the phase-field damage boundary condition is applied to the sample with $\phi = 0$ defining the initial crack at the notch.



Figure 7.11: Angular specimen with 9.13 mm initial crack is applied with the displacement boundary conditions as tensile loading until failure

7.2.1 Dry sample

The fracture toughness is initially investigated on an adhesive-A dry sample using the finite element method. The finite element model of the angular sample is defined with the material properties of the dry sample (0% r.H.) listed in Table 7.1. The input parameters for the phase-field model are the initial crack length $\ell_f = 9.13$ mm and the critical fracture energy $E_c = 4.182$ N/mm.

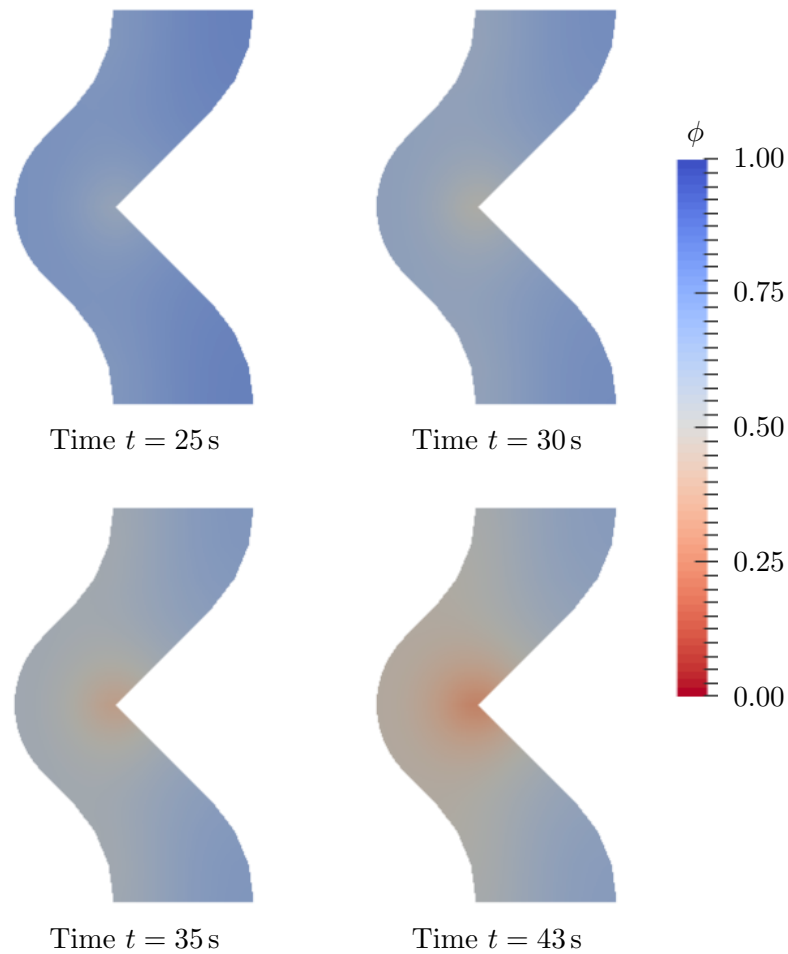


Figure 7.12: Contour plots of the crack propagation at different times of the finite element simulation in the angular sample (DIN ISO 34-1) under tensile loading condition

The finite element model for a dry sample is solved monolithically using the Newton's iterative method in a quasi-static manner. This means each time step of the simulation is solved in several pseudo-time steps until the residual norm reaches a tolerance. The solution scheme is solved in several time steps with a constant time increment until fracture. Figure 7.12 shows the contour plots of the diffusive crack under tensile load. A network of fine cracks is formed on the sample surface at time $t = 25$ s, and these cracks grow until the material fails into two pieces at time $t = 43$ s.

The force-time and the force-displacement curves from the simulation are compared with the experimental test data. The test used in the comparison

is the mean value calculated from the series of three angular test samples manufactured at the same atmospheric conditions [154]. Figure 7.13 compares the experimental and the simulation data, where the deviation between the curves is shown with the error bars. The standard deviation increases to the maximum for the stretch close to failure, as seen in the force-displacement curve, see Figure 7.13b.

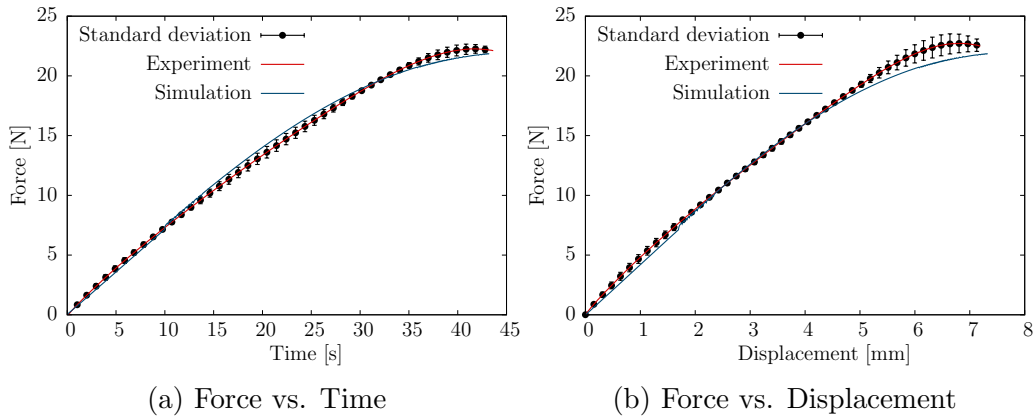


Figure 7.13: Tear tests are performed on dry samples of adhesive-A at 60°C

7.2.2 Aged sample

The influence of moisture concentration on fracture toughness is investigated in the aged samples. These aged samples were prepared in humid climatic conditions with relative humidities of 29% r.H., 67% r.H. and 100% r.H. at a temperature of 60°C. The length scale parameter ℓ_f and the critical energy release rate E_c are the required material parameter for the investigation of the damage using the phase-field approach. The length scale parameter $\ell_f = 9.13$ mm is the initial crack imparted in the angular specimen at the notch, and the critical energy release rate is identified using the optimisation algorithm. The critical energy release rate E_c is identified individually for the samples aged at different relative humid conditions (29% r.H., 67% r.H. and 100% r.H.) manufactured under the isothermal condition of 60 °C. The optimal value of the critical energy release rate is listed in Table 7.2.

The force-time and the force-displacement curves from the simulation and the tests are compared to verify the identified material parameters of the

Table 7.2: Material parameters of the phase-field damage material model identified for aged samples at different relative humidities in the atmosphere at an isothermal condition of 60° C

Identified critical energy release rate of the aged samples			
ageing condition	29% r.H.	67% r.H.	100% r.H.
E_c [N/mm]	5.25 N/mm	4.82 N/mm	4.52 N/mm

phase-field damage model. Figures 7.14, 7.15, and 7.16 show the comparison of the experiment and the simulation data. The tear test data (Experiment) shown in the figures correspond to the mean values of the series of three angular test samples manufactured for each atmospheric condition of three different relative humid conditions of 29% r.H., 67% r.H. and 100% r.H. at an isothermal condition of 60 °C. The standard deviation between the curves is represented in Figure 7.14, 7.15 and 7.16 with the error bars. The deviation in the form of small error bars indicates that the problem is well posed, and the phase-field material parameters are verified for the numerical analysis.

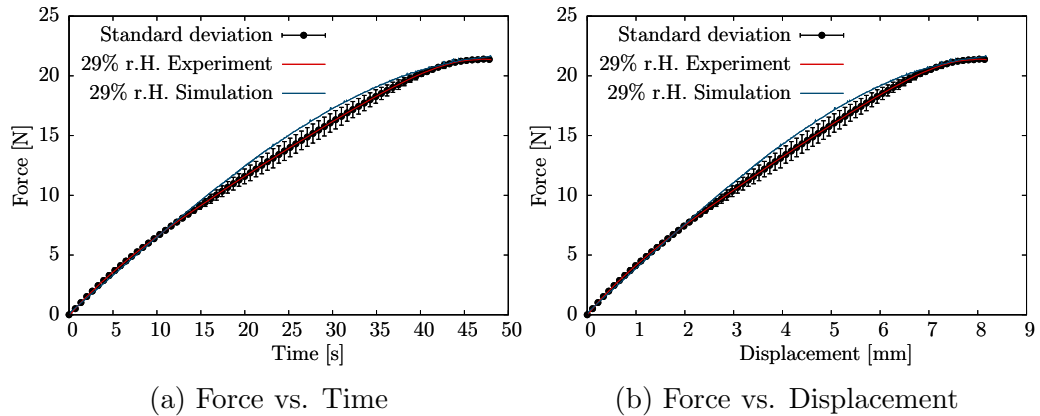


Figure 7.14: Tear tests are performed on the samples of adhesive-A aged at 29% relative humid atmospheric conditions with homogeneous moisture distribution at 60°C

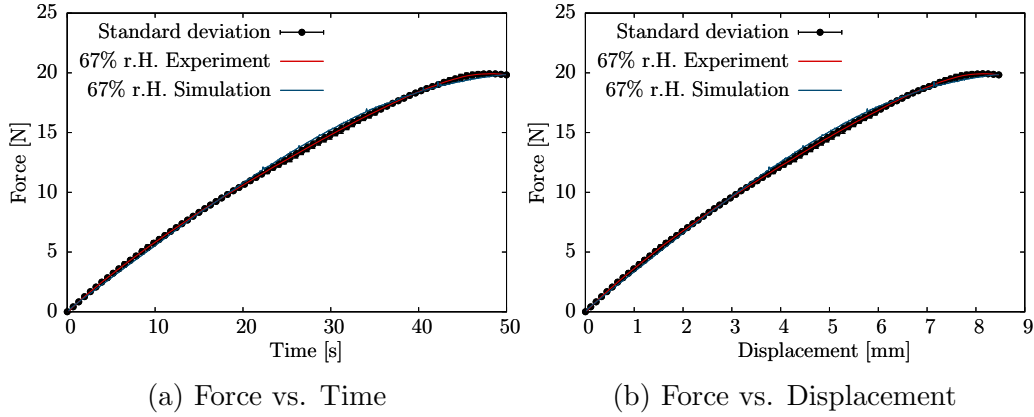


Figure 7.15: Tear tests are performed on the samples of adhesive-A aged at 67% relative humid atmospheric conditions with homogeneous moisture distribution at 60°C

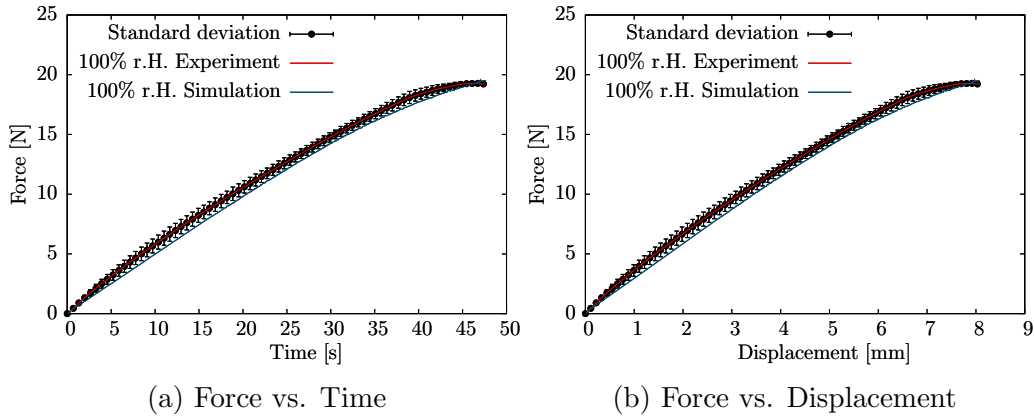


Figure 7.16: Tear tests are performed on the samples of adhesive-A aged at 100% relative humid atmospheric conditions with homogeneous moisture distribution at 60°C

The critical energy release rate of the aged samples shown in Figure 7.17 indicates that the adhesive material becomes ductile under the influence of moisture, thus leading to an increase in the critical energy release rate. The critical energy release rate is minimum for the dry sample and reaches a maximum for the sample saturated at 29% relative humidity.

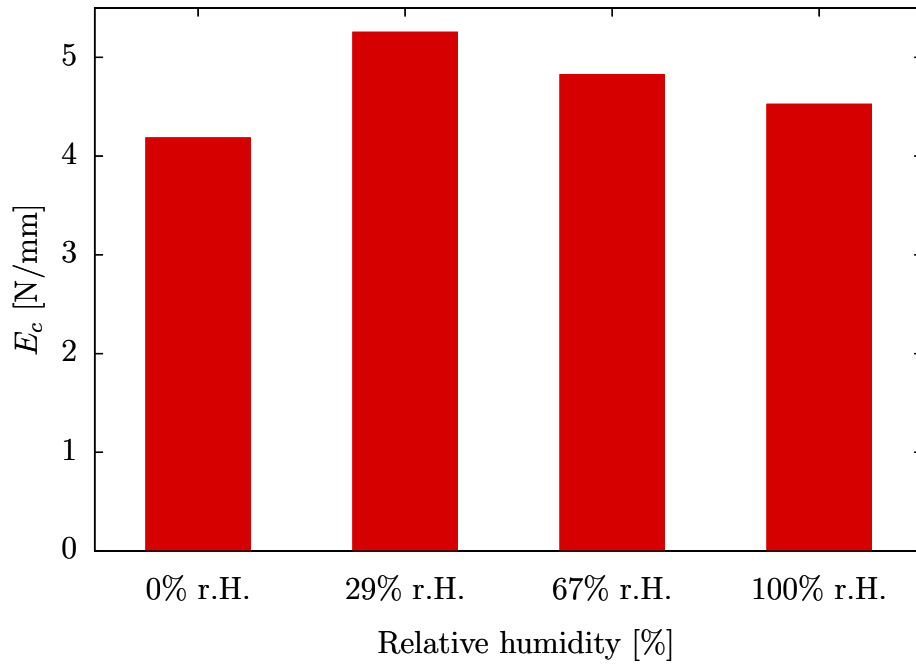


Figure 7.17: Critical fracture energy release rate E_c of adhesive-A samples aged at different relative humidities (r.H.) in the atmosphere at 60° C

8

Coupled diffusion-deformation-damage

Due to the ageing mechanism, the moisture diffused in the adhesive samples influences the mechanical properties. The ductility of the sample also depends on the local moisture concentration diffused in the material. The influence of moisture on the viscoelastic behaviour and fracture toughness is experimentally investigated in chapter 7. A material model is required for the numerical investigation of moisture influence on mechanical behaviour. To this end, a multi-physically coupled material model is formulated between the moisture diffusion, viscoelasticity and damage. The primary focus of this chapter is to give the theoretical background required for the coupled formulation and provide results of the numerical evaluation to validate the need for the material model quantitatively.

8.1 Diffusion coupled with phase-field damage

Moisture influence on the fracture toughness of adhesives is not yet fully understood but studied mostly with an emphasis on moisture influence in

the interface fracture between the adhesive and adherents in the bonded joints [37, 125]. From these studies influence of moisture on the debonding is investigated but not its influence on the tear strength. Here a multi-physically coupled material model is used to analyse the effects of moisture on the fracture toughness of the polyurethane adhesive. The thermodynamic consistency of the multi-physically coupled formulation is discussed with the Clausius-Duhem inequality and the Coleman-Noll procedure.

8.1.1 Thermodynamical consistency

The work done in the coupled mechanical diffusion problem can be decomposed into mechanical and diffusion parts. The mechanical part is further decomposed into the work done by the mechanical forces and the micro forces causing damage. This leads to virtual power as

$$\dot{\mathcal{E}} = \mathcal{P}_{\text{mech}} + \mathcal{P}_{\text{mic}} + \mathcal{P}_{\text{diff}}, \quad (8.1)$$

where \mathcal{E} is the total power, $\mathcal{P}_{\text{mech}}$ denotes the mechanical power, \mathcal{P}_{mic} denotes the power of the micro force system and $\mathcal{P}_{\text{diff}}$ is the power spent to diffuse moisture through the material domain. The virtual power of the system for a generalised virtual velocity $\mathcal{V} = \{\dot{\mathbf{u}}, \dot{\phi}, \dot{m}\}$ takes the form

$$\begin{aligned} \int_{\Omega} \mathbf{T} : \text{grad} \dot{\mathbf{u}} \, dV + \int_{\Omega} \boldsymbol{\omega} \cdot \text{grad} \dot{\phi} \, dV + \int_{\Omega} \zeta \dot{\phi} \, dV - \int_{\Omega} R_m \mathbf{q} \cdot \mathbf{N} \, dA = \\ \int_{\partial\Omega} \mathbf{t} \cdot \dot{\mathbf{u}} \, dA + \int_{\Omega} \mathbf{b} \cdot \dot{\mathbf{u}} \, dV + \int_{\partial\Omega} \chi \dot{\phi} \, dA + \int_{\Omega} \Upsilon \dot{\phi} \, dV, \end{aligned} \quad (8.2)$$

\mathbf{T} is the Cauchy stress tensor, \mathbf{t} is traction, and \mathbf{b} is the external body force acting on the system. $\boldsymbol{\omega}$ is the microscopic stress power conjugated to $\text{grad} \dot{\phi}$, microscopic internal force ζ , external traction χ and the external microscopic force Υ are the power-conjugate to $\dot{\phi}$. The diffusive power is introduced with chemical potential R_m for the diffusive flux of \mathbf{q} over the boundary.

Equilibrium equations of the viscoelastic, phase-field and diffusion behaviours are derived by setting an arbitrarily varying component of the generalised virtual velocity to value zero. The governing equation obtained after applying variational principle are

$$\operatorname{div} \mathbf{T} + \mathbf{b} = \mathbf{0}, \forall \mathcal{V} = \{\dot{\mathbf{u}}, 0, 0\} \quad (8.3a)$$

$$\operatorname{div} \boldsymbol{\omega} - \varsigma + \Upsilon = 0, \forall \mathcal{V} = \{0, \dot{\phi}, 0\} \quad (8.3b)$$

$$\dot{m} + \operatorname{div} \mathbf{q} = 0, \forall \mathcal{V} = \{0, 0, \dot{m}\} \quad (8.3c)$$

where equation (8.3a) corresponds to the balance of momentum describing the finite-strain viscoelastic behaviour, equation (8.3b) corresponds to phase-field microscopic force balance that describes the damage behaviour, and the equation (8.3c) describes the mass transport within the material domain. The traction \mathbf{t} and microscopic traction χ defined in the definition of the virtual power given in equation (8.2) is computed as $\mathbf{t} = \mathbf{T} \cdot \mathbf{n}$ and $\chi = \boldsymbol{\omega} \cdot \mathbf{n}$.

8.1.2 Material theory

The constitutive equations developed within the framework defined in equations (8.3a), (8.3b), and (8.3c) represent a specific definition of the relationships between kinematics and balance equations. These constitutive equations serve to couple mechanical behaviour with diffusion and damage. For the continuum mechanical description, the standard argument of the entropy principle has to be fulfilled

$$\mathbf{T} : \mathbf{D} + \boldsymbol{\omega} \cdot \operatorname{grad} \dot{\phi} + \varsigma \dot{\phi} - \operatorname{div} (R_m \mathbf{q}) - \dot{W} \geq 0. \quad (8.4)$$

Entropy inequality is still valid and independent of the considered material class. The Clausius-Planck inequality is evaluated with the process variables corresponding to the nonlinear viscoelasticity, the phase-field variable ϕ and moisture concentration m to introduce the constitutive relations

$$\mathcal{S} = \{\mathbf{B}, \mathbf{B}_e^j, \phi, \operatorname{grad} \phi, m\}, \quad (8.5)$$

where $\mathbf{B}, \mathbf{B}_e^j$ are the right Cauchy deformation tensor of the equilibrium and non-equilibrium springs. This free energy is additively decomposed into a mechanical W_{mech} , phase-field W_ϕ and diffusive W_m energies as

$$W = W_b \left(J, \bar{\mathbf{I}}_1^{\mathbf{B}}, \bar{\mathbf{I}}_1^{\mathbf{B}_e^j}, \phi, m \right) + W_\phi (\phi, \operatorname{grad} \phi, m) + W_m(m, m_b). \quad (8.6)$$

Due to the kinematic coupling between the mechanical, phase-field and diffusion energies, the mechanical free energy is the function of the phase-field

and diffusion variables. The mechanical free energy is additively decomposed into the volume-changing part W_{vol} and the shape-changing parts consisting of the equilibrium W_{eq} and j^{th} non-equilibrium W_{neq}^j parts to model a nearly incompressible viscoelastic behaviour

$$W_b \left(J, \bar{\mathbf{I}}_1^{\mathbf{B}}, \bar{\mathbf{I}}_1^{\mathbf{B}^j}, \phi, m \right) = W_{\text{vol}}(J, \phi, m) + W_{\text{eq}} \left(\bar{\mathbf{I}}_1^{\mathbf{B}}, \phi, m \right) + \sum_{j=1}^n W_{\text{neq}}^j \left(\bar{\mathbf{I}}_1^{\mathbf{B}^j}, \phi, m \right). \quad (8.7)$$

By combining equations (8.6) and (8.7) leads to the free energy function formulation as

$$\begin{aligned} W = & W_{\text{vol}}(J, \phi, m) + W_{\text{eq}} \left(\bar{\mathbf{I}}_1^{\mathbf{B}}, \phi, m \right) + \sum_{j=1}^n W_{\text{neq}}^j \left(\bar{\mathbf{I}}_1^{\mathbf{B}^j}, \phi, m \right) \\ & + W_{\phi}(\phi, \text{grad } \phi, m) + W_m(m, m_b). \end{aligned} \quad (8.8)$$

The time derivative of the energy function is derived according to the chain rule of the differentiation

$$\begin{aligned} \dot{W} = & \frac{\partial W_{\text{vol}}(J, \phi, m)}{\partial \mathbf{B}} : \dot{\mathbf{B}} + \frac{\partial W_{\text{eq}}(\bar{\mathbf{I}}_1^{\mathbf{B}}, \phi, m)}{\partial \mathbf{B}} : \dot{\mathbf{B}} + \sum_{j=1}^n \frac{\partial W_{\text{neq}}^j(\bar{\mathbf{I}}_1^{\mathbf{B}^j}, \phi, m)}{\partial \mathbf{B}_e^j} : \dot{\mathbf{B}}_e^j \\ & + \frac{\partial W}{\partial \phi} : \dot{\phi} + \frac{\partial W}{\partial \text{grad } \phi} : \text{grad } \dot{\phi} + \frac{\partial W_m(m, m_b)}{\partial m} : \dot{m}, \end{aligned} \quad (8.9)$$

after substituting the time derivative of free energy in the equation (8.4) leads to the inequality equation

$$\begin{aligned} & \left(-2\rho \mathbf{B} \cdot \frac{\partial W_{\text{vol}}}{\partial \mathbf{B}} - 2\rho \mathbf{B} \cdot \frac{\partial W_{\text{eq}}}{\partial \mathbf{B}} - \sum_{j=1}^n 2\rho \bar{\mathbf{B}}_e^j \cdot \frac{\partial W_{\text{neq}}}{\partial \bar{\mathbf{B}}_e^j} + \mathbf{T} \right) : \mathbf{D} \\ & + \sum_{j=1}^n 2\rho \frac{\partial W_{\text{neq}}}{\partial \bar{\mathbf{B}}_e^j} : \left(\mathbf{F}_e^j \cdot \overset{\Delta}{\Gamma}_i^j \cdot (\mathbf{F}_e^j)^T \right) + \left(\varsigma - \frac{\partial W}{\partial \phi} \right) \cdot \dot{\phi} \\ & + \left(\omega - \frac{\partial W}{\partial \text{grad } \phi} \right) \cdot \text{grad } \dot{\phi} + \left(-\rho \frac{\partial W_m(m, m_b)}{\partial m} + R_m \right) \cdot \dot{m} \\ & - \text{grad } R_m \cdot \mathbf{q} \geq 0. \end{aligned} \quad (8.10)$$

The entropy inequality is evaluated based on the argumentation of Coleman & Noll leading to the constitutive equation for the Cauchy stress. After considering an assumption for the free energy function $W_{(\bullet)} = \rho W_{(\bullet)}$ [55]

leads to the Cauchy stress tensor as

$$\mathbf{T} = 2\mathbf{B} \cdot \frac{\partial W_{\text{vol}}}{\partial \mathbf{B}} + 2\mathbf{B} \cdot \frac{\partial W_{\text{eq}}}{\partial \mathbf{B}} + \sum_{j=1}^n 2\bar{\mathbf{B}}_e^j \cdot \frac{\partial W_{\text{neq}}}{\partial \bar{\mathbf{B}}_e^j}, \quad (8.11)$$

and the constitutive equations for the microscopic phase-field equations

$$\omega = \frac{\partial W_\phi(\phi, \text{grad } \phi, m)}{\partial \phi}, \quad \varsigma = \frac{\partial W_\phi(\phi, \text{grad } \phi, m)}{\partial \text{grad } \phi}. \quad (8.12)$$

By inserting the constitutive equations of ω and ς in equation (8.3b) leads to the local micro force balance

$$\text{div} \left(\frac{\partial W_\phi(\phi, \text{grad } \phi, m)}{\partial \text{grad } \phi} \right) - \frac{\partial W_\phi(\phi, \text{grad } \phi, m)}{\partial \phi} = 0. \quad (8.13)$$

The phase-field evolution equation is derived from the phase-field constitutive equation based on the micro-force balance proposed by Gurtin [54]. The phase-field evolution equation dependent on the local moisture concentration takes the form

$$\dot{\phi} = -M \left(W_b \left(J, \bar{\mathbf{I}}_1^{\mathbf{B}}, \bar{\mathbf{I}}_1^{\bar{\mathbf{B}}_e^j}, \phi, m \right) - E_c(m) \left(\ell_f \text{div } \phi - \frac{1}{\ell_f} (1 - \phi) \right) \right), \quad (8.14)$$

where $E_c(m)$ is the critical energy release rate formulated as the function of the local moisture concentration to consider the influence of the moisture diffusion. Further evaluation of the inequality equation (8.10) lead to chemical potential

$$R_m = \rho \frac{\partial W_m(m, m_b)}{\partial m}. \quad (8.15)$$

After the evaluation, the residual dissipation equation remains

$$\sum_{j=1}^n 2\rho \frac{\partial W_{\text{neq}}}{\partial \bar{\mathbf{B}}_e^j} : \left(\mathbf{F}_e^j \cdot \bar{\mathbf{\Gamma}}_i^j \cdot (\mathbf{F}_e^j)^T \right) - \text{grad } R_m \mathbf{q} \geq 0, \quad (8.16)$$

that have to be fulfilled by all the terms of the inequality separately. The first term of the inequality is evaluated to obtain the inelastic right Cauchy-Green deformation tensor

$$\dot{\bar{\mathbf{C}}}_i^j = \frac{4}{r_j} \left[\bar{\mathbf{C}} - \frac{1}{3} \text{tr} \left(\bar{\mathbf{C}} \cdot (\bar{\mathbf{C}}_i^j)^{-1} \right) \bar{\mathbf{C}}_i^j \right]. \quad (8.17)$$

The chemical potential R_m is evaluated by substituting the free energy function of moisture diffusion $W(m, m_b)$ given in equation (3.48) in the equation (8.15). Constitutive equation satisfying the second term of the residual dissipation equation (8.16) is defined as

$$\mathbf{q} = -D (\text{grad} R_m), \quad (8.18)$$

where R_m is the chemical potential defined in the equation (3.43) and the moisture flux as takes the form (see Chapter 3.3.1)

$$\mathbf{q} = -D \text{grad} (m - m_b). \quad (8.19)$$

The moisture flux and balance of mass lead to the diffusion equation

$$\frac{dm}{dt} = D \text{div} (\text{grad} (m - m_b)) \quad (8.20)$$

where the immobile moisture concentration is evaluated with the evolution equation (3.2) as discussed in the chapter 3.1.

8.1.3 influence of moisture diffusion on fracture toughness

The influence of the moisture concentration on the fracture toughness is considered by taking the moisture-dependent critical energy release rate. A prerequisite of this theory is to compute the energy release rate at the integration points based on the local moisture concentration. As a result, the moisture-dependent energy release rate takes the form

$$\frac{E_c(m)}{E_c(m=0)} = g(m) \forall m \in [0, 1.70] \quad (8.21)$$

where $E_c(m=0)$ is the critical energy release rate of the dry sample. The bulk energy decreases as the crack propagates in the material because of the decay in the material stiffness. Where the decay in the stiffness is evaluated using the moisture-dependent viscoelastic parameters. The decrease in the bulk energy is evaluated by multiplying the bulk energy with the degradation function $g(\phi)$ as follows

$$W_b \left(\bar{\mathbf{I}}_1^{\mathbf{B}}, \bar{\mathbf{I}}_1^{\mathbf{B}^j}, J, \phi, m \right) = g(\phi) W_0 \left(\bar{\mathbf{I}}_1^{\mathbf{B}}, \bar{\mathbf{I}}_1^{\mathbf{B}^j}, J, m \right), \quad (8.22)$$

where $W_0(\bar{\mathbf{I}}_1^{\bar{\mathbf{B}}}, \bar{\mathbf{I}}_1^{\bar{\mathbf{B}}^j}, J, m)$ is the mechanical energy dependent on the moisture concentration. The moisture-dependent stiffness parameters $\mu(m)$ are calculated by interpolating the dry and saturated stiffness parameters as discussed in chapter 7.1.1. The constitutive equation for the Cauchy stress is calculated with the moisture-dependent stiffness parameter as

$$\mathbf{T}(\bar{\mathbf{B}}, \bar{\mathbf{B}}_e^j, J, m, \phi) = g(\phi) \left(\mathbf{T}_{\text{vol}}(J, m) + \mathbf{T}_{\text{eq}}(\bar{\mathbf{B}}, m) + \sum_{j=1}^n \mathbf{T}_{\text{neq}}^j(\bar{\mathbf{B}}_e^j, m) \right). \quad (8.23)$$

After taking into account degradation and decay in the mechanical properties and energies discussed in the equations (8.22) and (8.23) and combining with the phase-field evolution equation (8.14) with the set of equilibrium equations (8.3a), (8.3b) and (8.3c) yields

$$\text{div}(g(\phi) \mathbf{T}(\bar{\mathbf{B}}, \bar{\mathbf{B}}_e^j, J, m)) = \mathbf{0} \quad (8.24a)$$

$$g'(\phi) W_0(\bar{\mathbf{I}}_1^{\bar{\mathbf{B}}}, \bar{\mathbf{I}}_1^{\bar{\mathbf{B}}^j}, J, m) + E_c(m) \left[-\frac{1}{\ell_f} (1 - \phi) + \ell_f \text{div} \phi \right] = 0 \quad (8.24b)$$

$$\dot{m} - D \text{div}(\text{grad}(m - m_b)) = 0 \quad (8.24c)$$

8.2 Boundary conditions

The coupled formulation is specified with the Dirichlet and Neumann-type boundary conditions. The surface $\partial\Omega$ is decomposed to define boundary conditions according to the primary field variables. These boundary conditions are postulated based on the corresponding primary field variables

$$\partial\Omega = \partial\Omega_{\mathbf{u}}^D \cup \partial\Omega_{\mathbf{t}}^N, \quad \partial\Omega = \partial\Omega_m^D \cup \partial\Omega_{\mathbf{q}}^N \quad \text{and} \quad \partial\Omega = \partial\Omega_{\phi}^D \cup \partial\Omega_{\nabla\phi}^N \quad (8.25)$$

with $\partial\Omega_{\mathbf{u}}^D \cap \partial\Omega_{\mathbf{t}}^N = \emptyset$, $\partial\Omega_m^D \cap \partial\Omega_{\mathbf{q}}^N = \emptyset$ and $\partial\Omega_{\phi}^D \cap \partial\Omega_{\nabla\phi}^N = \emptyset$. The prescribed deformation \mathbf{u} and traction \mathbf{t} of the mechanical problem on the boundaries is postulated with the Dirichlet and Neumann boundary conditions

$$\mathbf{u}(\mathbf{x}, t) = \mathbf{u}_D(\mathbf{x}, t) \quad \text{on} \quad \partial\Omega_{\mathbf{u}}^D \quad \text{and} \quad \mathbf{T} \cdot \mathbf{n} = \mathbf{t} \quad \text{on} \quad \partial\Omega_{\mathbf{t}}^N. \quad (8.26)$$

The Dirichlet and Neumann boundary conditions are derived on the crack surface for the phase-field damage model with

$$\phi(\mathbf{x}, t) = 0 \quad \text{on} \quad \partial\Omega_{\phi}^D \quad \text{and} \quad \nabla\phi \cdot \mathbf{n} = 0 \quad \text{on} \quad \partial\Omega_{\nabla\phi}^N. \quad (8.27)$$

and the Dirichlet- and Neumann-type boundary conditions for moisture diffusion are given by

$$\begin{aligned} m(\mathbf{x}, t) &= m(\mathbf{x}, t) \text{ on } \partial\Omega_m^D \text{ and} \\ \mathbf{q} \cdot \mathbf{n} &= D(\text{grad } m_f) \cdot \mathbf{n} = q(\mathbf{x}, t) \text{ on } \partial\Omega_q^N. \end{aligned} \quad (8.28)$$

8.3 Finite element implementation

The weak forms of the coupled system of equations for diffusion, phase-field and viscoelasticity follow

$$\begin{aligned} \mathbf{r}_u(\mathbf{u}) &= \int_{\Omega} g(\phi) \mathbf{T}(\bar{\mathbf{B}}, \bar{\mathbf{B}}_e^j, J, m) : \text{grad}^s \delta \mathbf{u} \, dV = 0, \\ \mathbf{r}_i^\phi &= \int_{\Omega} [2(1-\zeta)\phi \delta\phi W] \, dV + E_c \int_{\Omega} \left[-\frac{1}{\ell_f} (1-\phi) \delta\phi + \ell_f \text{grad}\phi \text{grad}\delta\phi \right] \, dV = 0, \\ \mathbf{r}_m(m) &= \int_{\Omega} \delta m \frac{m^{t+1} - m^t}{\Delta t} \, dV + \int_{\Omega} \left[\text{grad}\delta m \cdot D \frac{1}{2} \text{grad}(m^{t+1} - m_b^{t+1}) \right] \, dV \\ &\quad - \int_{\Omega} \left[\text{grad}\delta m \cdot D \frac{1}{2} \text{grad}(m^t - m_b^t) \right] \, dV = 0. \end{aligned} \quad (8.29)$$

Displacement field \mathbf{u} , damage ϕ and moisture concentration m variables of the coupled system are approximated as

$$\mathbf{u} = \sum_{i=1}^{n_{\text{ele}}} \mathbf{N}_i^u \mathbf{u}_i, \quad m = \sum_{i=1}^{n_{\text{ele}}} N_i m_i, \quad \phi = \sum_{i=1}^{n_{\text{ele}}} N_i^\phi \phi_i, \quad (8.30)$$

where n_{ele} is a number of an unknown degree of freedom of an element. \mathbf{N}_i^u , N_i^ϕ and N_i are the shape functions of the displacement, damage and moisture concentration. The shape function of the displacement field follows

$$\mathbf{N}_i^u = \begin{bmatrix} N_i & 0 & 0 \\ 0 & N_i & 0 \\ 0 & 0 & N_i \end{bmatrix}, \quad (8.31)$$

where, $N_i = N_1, N_2, \dots, N_{n_{\text{ele}}}$ denotes the respective shape function of the element at the quadrature points associated with the respective nodes. Con-

sequently, the virtual quantities of the primary variables and their corresponding derivatives are discretised as

$$\begin{aligned}\delta \mathbf{u} &= \sum_{i=1}^{\text{n_ele}} \mathbf{N}_i^{\delta \mathbf{u}} \mathbf{u}_i, & \delta m &= \sum_{i=1}^{\text{n_ele}} N_i \delta m_i, & \delta \phi &= \sum_{i=1}^{\text{n_ele}} N_i^{\phi} \delta \phi_i \\ \text{grad}^s \delta \mathbf{u} &= \sum_{i=1}^{\text{n_ele}} \mathbf{S}_i^{\mathbf{u}} \delta \mathbf{u}_i, & \text{grad} \delta m &= \sum_{i=1}^{\text{n_ele}} \mathbf{S}_i^m \delta m_i, & \text{grad} \delta \phi &= \sum_{i=1}^{\text{n_ele}} \mathbf{S}_i^{\phi} \delta \phi_i.\end{aligned}\quad (8.32)$$

Here, the derivative of the shape function as \mathbf{S} matrix is introduced to evaluate the strain-displacement matrix as

$$\mathbf{S}_i^{\mathbf{u}} = \begin{bmatrix} N_{i,x} & 0 & 0 \\ 0 & N_{i,y} & 0 \\ 0 & 0 & N_{i,z} \\ N_{i,y} & N_{i,x} & 0 \\ 0 & N_{i,z} & N_{i,y} \\ N_{i,z} & 0 & N_{i,x} \end{bmatrix}, \quad \mathbf{S}_i^m = \begin{bmatrix} N_{i,x} \\ N_{i,y} \\ N_{i,z} \end{bmatrix}, \quad \mathbf{S}_i^{\phi} = \begin{bmatrix} N_{i,x} \\ N_{i,y} \\ N_{i,z} \end{bmatrix}, \quad \text{with} \quad \begin{bmatrix} N_{i,x} \\ N_{i,y} \\ N_{i,z} \end{bmatrix} = \begin{bmatrix} \frac{\partial N_i}{\partial x} \\ \frac{\partial N_i}{\partial y} \\ \frac{\partial N_i}{\partial z} \end{bmatrix}.$$

(8.33)

Inserting the approximated field variables and their derivatives in the residuals of the coupled system of equations leads to

$$\begin{aligned}\mathbf{r}_{\mathbf{u}}(\mathbf{u}) &= \int_{\Omega} g(\phi) \mathbf{T}(\bar{\mathbf{B}}, \bar{\mathbf{B}}_e^j, J, m) : (\mathbf{S}_i^{\mathbf{u}})^T dV = \mathbf{0} \\ r_i^{\phi} &= \int_{\Omega} [2(1-\zeta)\phi N_i W] dV + E_c \left[-\frac{1}{\ell_f} (1-\phi) N_i + \ell_f (\mathbf{S}_i^{\phi})^T \mathbf{S}_j^{\phi} \right] dV = 0 \\ r_m(m) &= \int_{\Omega} N_i^m \frac{m^{t+1} - m^t}{\Delta t} dV + \int_{\Omega} \left[\mathbf{S}_i^m \cdot D \frac{1}{2} \text{grad} (m^{t+1} - m_b^{t+1}) \right] dV \\ &\quad - \int_{\Omega} \left[\mathbf{S}_i^m \cdot D \frac{1}{2} \text{grad} (m^t - m_b^t) \right] dV = 0.\end{aligned}\quad (8.34)$$

This system of coupled equations is to be solved with the help of the Newton-Raphson iterative method

$$\begin{bmatrix} \mathbf{K}^{uu} & \mathbf{K}^{u\phi} & 0 \\ \mathbf{K}^{\phi u} & \mathbf{K}^{\phi\phi} & 0 \\ 0 & 0 & \mathbf{K}^{mm} \end{bmatrix} \begin{bmatrix} d\mathbf{u} \\ d\phi \\ dm \end{bmatrix} = \begin{bmatrix} -\mathbf{r}_u(\mathbf{u}_i) \\ -\mathbf{r}_\phi(\phi_i) \\ -\mathbf{r}_m(m_i) \end{bmatrix}, \quad (8.35)$$

and the components of the tangent stiffness matrix are

$$\begin{aligned} \mathbf{K}_{i,j}^{uu} &= \frac{\partial \mathbf{r}_i^u}{\partial \mathbf{u}_j} = \int_{\Omega} ((1-\zeta)\phi^2 + \zeta) \left(\mathbf{S}_i^u : \overset{4}{\boldsymbol{\kappa}}(m) : \mathbf{S}_j^u + \mathbf{S}_i^u : [\mathbf{T}(m) \cdot \mathbf{S}_j^u] \right) dV, \\ \mathbf{K}_{i,j}^{u\phi} &= \frac{\partial \mathbf{r}_i^u}{\partial \phi_j} = \int_{\Omega} 2(1-\zeta)\phi \mathbf{S}_i^u : \mathbf{T}^T(m) \cdot \mathbf{N}_j^u dV, \\ \mathbf{K}_{i,j}^{\phi u} &= \frac{\partial \mathbf{r}_i^\phi}{\partial \mathbf{u}_j} = \int_{\Omega} 2(1-\zeta)\phi \mathbf{N}_i^u \cdot \mathbf{T}^T(m) : \mathbf{S}_j^u dV, \\ \mathbf{K}_{i,j}^{\phi\phi} &= \frac{\partial \mathbf{r}_i^\phi}{\partial \phi_j} = \int_{\Omega} \left\{ (1-\zeta)W(m) \mathbf{N}_i^\phi \mathbf{N}_j^\phi + E_c \left[\frac{1}{\ell_f} \mathbf{N}_i^\phi \mathbf{N}_j^\phi + \ell_f (\mathbf{S}_i^\phi)^T : \mathbf{S}_j^\phi \right] \right\} dV, \\ \mathbf{K}_{i,j}^{mm} &= \frac{\partial \mathbf{r}_i^m}{\partial m_j} = \int_{\Omega} \mathbf{S}_i^m \mathbf{S}_j^m dV. \end{aligned} \quad (8.36)$$

The moisture diffusion equation is first solved from the coupled system of equations. Then the moisture influence is super-imposed over the mechanical properties by computing these properties at every integration point as the function of moisture concentration.

8.3.1 Numerical implementation

The multi-physically coupled diffusion, deformation and damage system is solved in a two-step process. The first step solves the diffusion problem using the Langmuir-type diffusion model. The second step solves the phase-field damage model monolithically using the moisture-dependent mechanical parameters. The coupled system of the equations is solved as a coupled staggering field to find a stable implicit solution as monolithic solutions encounter convergence problems.

The multi-physically coupled material model is implemented in deal.II and the implementation of the material model is explained with the help of the algorithms discussed in chapter 5.1.2. The diffusion problem solved using the Langmuir-type diffusion equation is explained with the Algorithm 1. The finite element mesh is imported to define the material properties and apply the desired boundary conditions to solve the moisture diffusion problem. Then the local moisture concentration is superimposed over the fracture problem to calculate the local stiffness and the critical-energy release rate of the material to investigate the moisture influence on the mechanical behaviour. The fracture problem is solved using the finite-strain phase-field damage model, and Algorithm 3 describes implementing the material model in deal.II. The set of classes and header files required to implement the coupled material model in deal.II FEM library is discussed in chapter 5.3.

8.4 Numerical simulation of notched specimen

Here the multi-physically coupled model is investigated on the double V-notched sample with the identified material properties of adhesive-A listed in chapter 6 & 7 to validate the reliability of the proposed coupled material model. At first, the double-notched V-shaped sample is numerically analysed

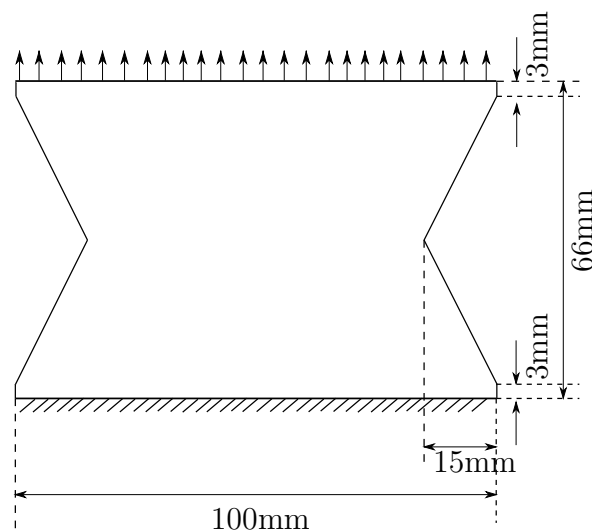


Figure 8.1: Bottom face of the sample applied with fixed boundary conditions and top face applied with displacement boundary conditions

for failure with the phase-field damage model. A schematic representation of the considered doubled V-notched sample with the applied tensile boundary conditions is shown in figure 8.1.

The finite-strain viscoelastic parameters and the phase-field damage identified for the adhesive-A sample in chapter 7 are used to evaluate the damage behaviour in a double V-notched sample. A three-dimensional specimen of a double V-notched sample of thickness 2 mm is discretised into finite element mesh with a mesh size of $h = 1.23\text{mm}$. The finite element model is analysed to investigate the fracture behaviour using the material properties of the dry and the aged samples listed in Table 8.1. The FE model is applied with displacement boundary conditions on the top face, and the bottom face is applied with fixed boundary conditions.

Table 8.1: Stiffness and energy release rate of polyurethane adhesive material identified for the different relative humid atmosphere at 60°C

Material parameters of finite-strain viscoelastic model						
		Relaxation times [s]	0% r.H.	29% r.H.	67% r.H.	100% r.H.
Equilibrium	c_{10} [MPa]		9.886	7.886	7.196	7.072
	c_{20} [MPa]		-1.414	-1.357	-1.122	-1.128
	c_{30} [MPa]		3.214	1.443	0.918	0.872
	D [MPa]		0.306	0.244	0.241	0.314
Non-equilibrium	c_{101} [MPa]	0.5	4.886	2.886	2.296	2.172
	c_{102} [MPa]	10	0.886	0.231	0.139	0.107
	c_{103} [MPa]	100	0.055	0.017	0.014	0.011
	c_{104} [MPa]	1000	0.005	0.003	0.002	0.001
Energy release rate	E_c [N/mm]		4.18	5.25	4.82	4.52

The load-displacement curves from the FE simulation of the dry and aged samples are shown in figure 8.2. The load-displacement curve of the dry sample shows better tensile behaviour when compared with the saturated sample. Still, the dry sample fails at a smaller load than the saturated samples because of the lower fracture toughness. From figure 8.2, it is evident that the sample's ductility increases with the increase in the diffused moisture concentration in the sample up to 29%, and a further increase in the moisture concentration leads to a decrease in the material's ductility.

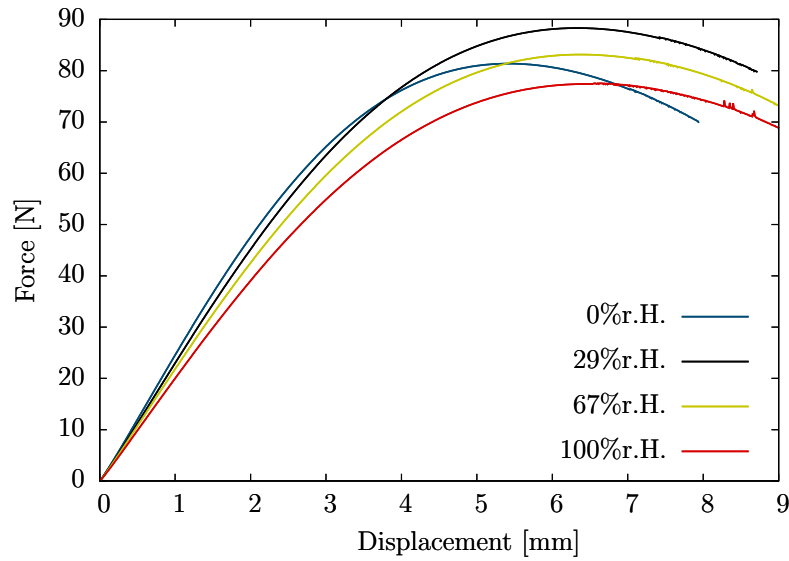


Figure 8.2: Load-Displacement comparison of dry and aged samples of the double V-notched samples from FE-simulation

8.4.1 Moisture-dependent mechanical properties

The influence of moisture diffusion on the energy release rate E_c is considered by taking a moisture-dependent energy release rate in the coupled problem. Where the energy release rate dependence on the moisture concentration is defined using a cubic spline function

$$\frac{E_c(m)}{E_c(m=0)} = \begin{cases} -1.56m^3 + 0.93m + 1, & \text{if } m \in [0, 0.34], \\ 1.11m^3 - 2.73m^2 + 1.86m + 0.89, & \text{if } m \in [0.34, 0.95], \\ -0.19m^3 + 0.97m^2 - 1.65m + 2.01, & \text{if } m \in [0.95, 1.70]. \end{cases} \quad (8.37)$$

The viscoelastic parameters are calculated by interpolating material parameters of the dry and saturated sample

$$\mu(m) = f(m) \mu^{\text{dry}} + (1 - f(m)) \mu^{\text{sat}}. \quad (8.38)$$

$\mu(m)$ is the resultant moisture-dependent stiffness parameters of the finite-strain viscoelastic model calculated at the integration points. μ^{dry} and μ^{sat} are the material parameters of dry and saturated samples at 60° C listed in table 7.1. $f(m)$ is the interpolation function for adhesive-A is calculated as

$$f(m) = e^{-3.93m} \text{ where } 1 \leq f(m) \lesssim 0, \quad (8.39)$$

8.5 Numerical evaluation

The coupled formulation is validated by conducting a numerical investigation on a double V-notch sample of adhesive-A. The adhesive-A material properties are considered from the chapters 6.2.1, 7.1.1 and 7.2.2. The double V-notched sample is applied with the diffusion and tensile boundary conditions. The influence of ageing on fracture is investigated on samples aged for different times $t = 500 \text{ s}, 1000 \text{ s}$ and 1500 s . A simple schematic representation of the aged geometry of the applied boundary conditions is illustrated in Figure 8.3a and 8.3b.

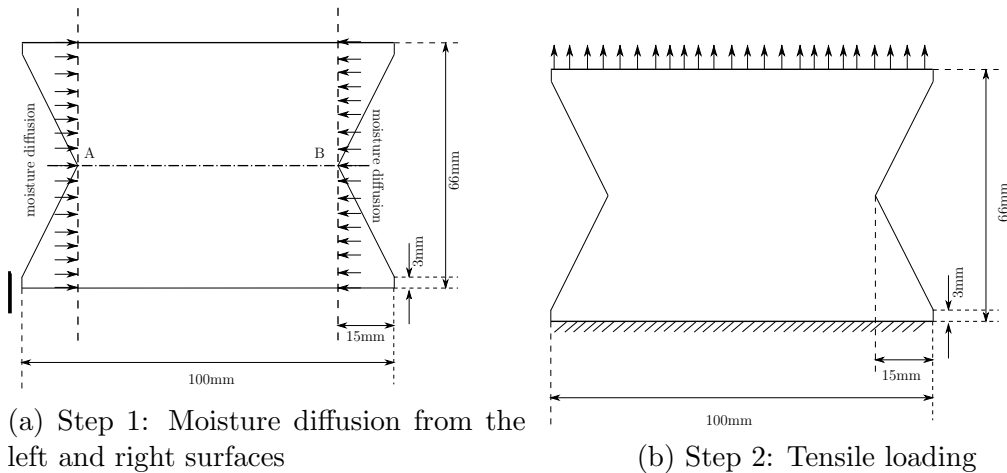


Figure 8.3: Double V-notched sample is influenced by moisture diffusion to age the sample in (a) Step 1, and then the tensile boundary conditions are applied until failure in (b) Step 2

The influence of moisture on the tear strength of adhesive-A is investigated for different relative humid atmospheric conditions. The tear strength is investigated for 29% r.H. climatic conditions, and the aged samples are prepared for 500h, 1000h and 1500h to understand the local effects of moisture diffusion on the tear strength. The diffusion of moisture is investigated in the first step then the moisture-dependent mechanical parameters of viscoelasticity and damage are calculated locally to consider the local effects of inhomogeneous moisture distribution.

The Langmuir-type diffusion parameters identified for the adhesive-A sample listed in Table 6.5 is used to analysing moisture diffusion. The equilibrium moisture concentration for 30%r.H. atmosphere listed in Table 6.1 is used as the diffusion boundary conditions. Diffusion boundary conditions are applied at the 15 mm cross-section at the start of V-notch on both sides to realise one-dimensional moisture diffusion. Figure 8.4 shows the distribution of moisture measured at the notch along the cross-section AB as shown in Figure 8.3a and varies between $0 < m < 0.35$.

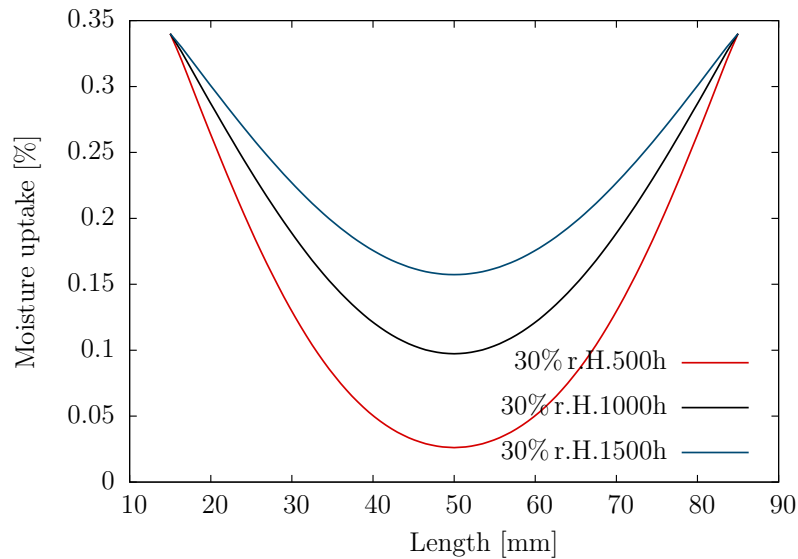


Figure 8.4: Distribution of moisture concentration at the centre along the 100mm length of the double V-notched sample at 30% r.H. at 60 °C

The tensile boundary conditions are applied on the sample with the inhomogeneous moisture distribution to analyse the tear strength using coupled formulation. The material parameters for dry and 29% r.H. saturated samples listed in Table 8.1 were used to calculate the moisture-dependent stiffness

parameters and energy release rate using the equations (8.38) and (8.37). The load-displacement data evaluated from the FE simulation is compared with the dry and saturated sample at 29% r.H. for the qualitative evaluation of the coupled-material model. Figure 8.5 compares the load-displacement data from FE-simulation of the double-V notched samples with inhomogeneous moisture against a dry (0% r.H.) and saturated sample at 29% r.H. as shown in Figure 8.2. The comparison shows that the sample becomes ductile as the ageing of the material progress with time, and the material saturated at 29% r.H shows higher tear resistance to fracture.

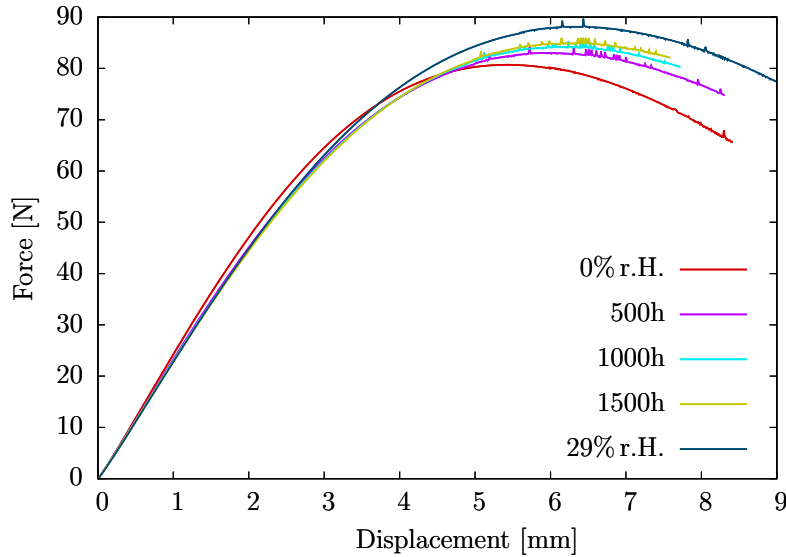


Figure 8.5: Load-Displacement comparison for the samples aged from 500h to 1500h with the dry and saturated sample at 29% r.H. at 60 °C

Maximum load and displacement values for the aged samples at failure are tabulated in Table 8.2. The load required for the sample to fail increases until the saturation is reached, and the displacement of the sample also increases showing ductile behaviour.

Table 8.2: Maximum load-displacement data of the sample aged at 29%r.H. at an isothermal condition of 60 °C

Load-Displacement					
	0% r.H.	500h	1000h	1500h	29% r.H.
Displacement [mm]	5.427	5.724	6.237	6.435	6.435
Load [N]	80.709	84.172	85.224	85.971	89.701

The coupled formulation is evaluated for 67%r.H. atmospheric conditions in the next step. Here, the equilibrium moisture concentration for 70%r.H. atmosphere listed in Table 6.1 is used as the diffusion boundary condition since diffusion tests were not performed for atmosphere with 67%r.H.¹. The Langmuir-type diffusion parameters of adhesive-A listed in Table 6.5 are used in analysing moisture diffusion. Figure 8.6 shows the inhomogeneous moisture distribution measured at the notch along the cross-section AB shown in Figure 8.3a and varies between $0 < m < 0.95$.

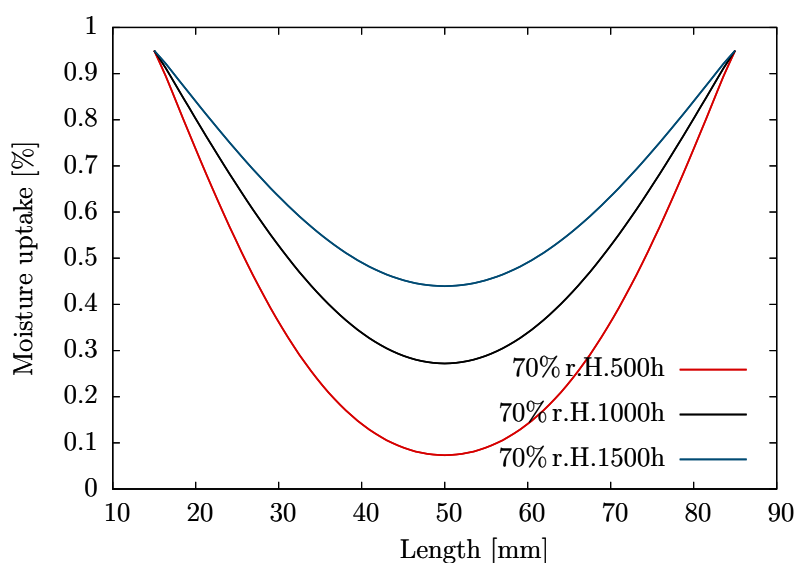


Figure 8.6: Distribution of moisture concentration at the centre along the 100mm length of the double V-notched sample aged at 70%r.H. at 60 °C

The tensile boundary conditions are applied to the aged samples with inhomogeneous moisture distribution to investigate the tear strength of the material. The material parameters of dry and 67% r.H. saturated samples listed in Table 8.1 were used to calculate the moisture-dependent stiffness parameters and energy release rate using the equations (8.38) and (8.37). The load-displacement data from FE-simulation performed on the aged samples with inhomogeneous moisture distribution is compared with the load-displacement data obtained from the FE-simulation of dry sample and saturated sample at 67% r.H. Figure 8.7 shows the load-displacement comparison of an aged

¹Here, the moisture absorbed by the sample saturated for a climate with 67%r.H. at 60°C is assumed to be approximately same as the moisture absorbed by the sample at 70%r.H.

sample with inhomogeneous moisture distribution against dry and saturated sample at 67% r.H. shown in Figure 8.2.

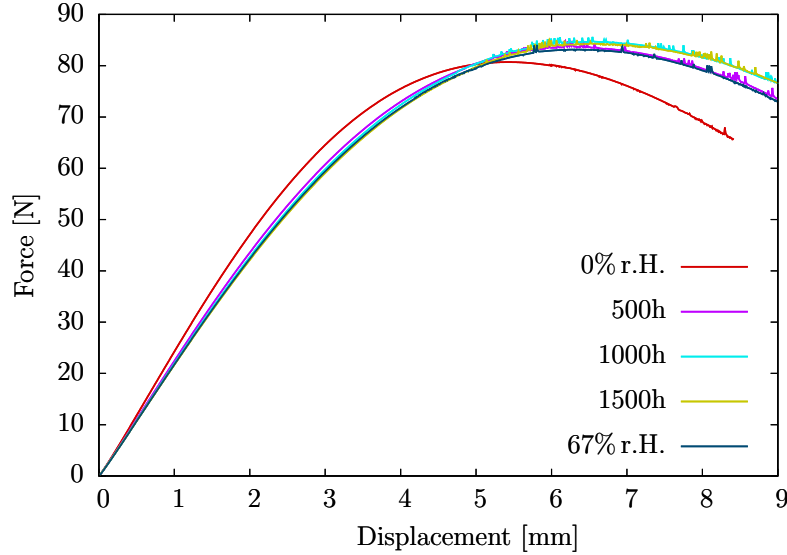


Figure 8.7: Load-Displacement comparison of the samples aged from 500h to 1500h with the dry and saturated sample for 67% r.H. at 60 °C

Maximum load and displacement values required by the sample until failure obtained from FE-simulation are tabulated in Table 8.3. The investigation performed with 67%r.H. climate condition shows that the material becomes ductile with the largest displacement and tear strength for the sample aged for 1000h. Further ageing leads to decreased material ductility with smaller displacement and tear strength. The saturated sample at 67%r.H. shows ductile behaviour than the dry material with larger displacement and higher tear strength at failure.

Table 8.3: Maximum load-displacement of the sample aged for 67%r.H. at an isothermal condition of 60 °C

Load-Displacement					
	0% r.H.	500h	1000h	1500h	67% r.H.
Displacement [mm]	5.427	6.183	6.543	6.336	5.805
Load [N]	80.709	84.836	85.612	84.994	84.083

The behaviour of the double V-notched sample is investigated for the atmosphere with 100%r.H humid condition. In the first step, the moisture distribution due to moisture diffusion is investigated by applying diffusion boundary condition listed in Table 6.2 and the Langmuir-type diffusion parameters of adhesive-A listed in Table 6.5 are used in analysing moisture diffusion. Figure 8.8 shows the moisture concentration distribution measured at the transition zone along the cross-section AB as shown in Figure 8.3a. The investigation is carried for samples aged for 500h, 1000h and 1500h and varies between $0 < m < 1.70$.

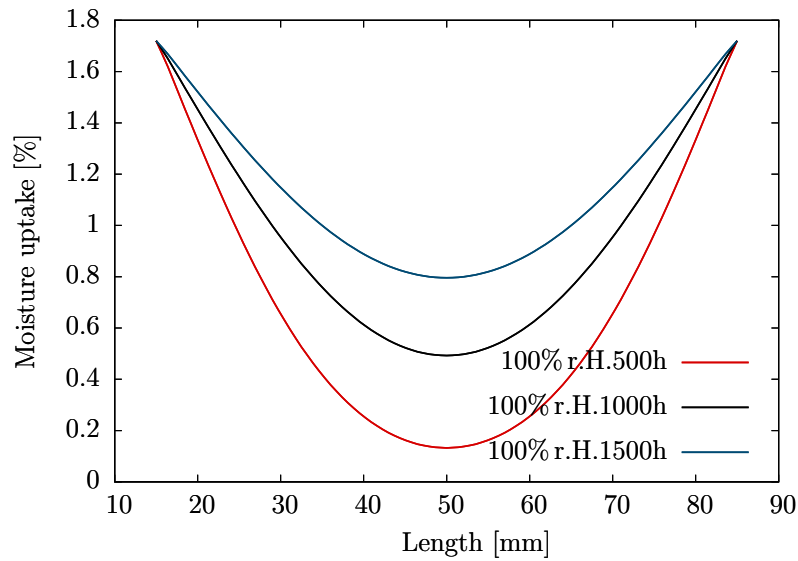


Figure 8.8: Distribution of moisture concentration at the centre along the 100mm length of the double V-notched sample aged at 100%r.H. at 60 °C

To investigate the fracture behaviour, the tensile load boundary conditions are applied on the samples aged for 500h, 1000h and 1500h. The moisture-dependent stiffness parameters and energy release rate properties are calculated with the equations (8.38) and (8.37) using the material parameters listed in Table 8.1. The load-displacement data from the FE-simulation of the aged double V-notch samples with the inhomogeneous moisture distribution is compared with the load-displacement FE-simulation data of dry and saturated sample at 100% r.H. Figure 8.9 shows the comparison of load-displacement data of aged samples with inhomogeneous moisture against the dry and saturated sample at 100% r.H. shown in the Figure 8.2.

The maximum load and displacement at the fracture of the samples are tab-

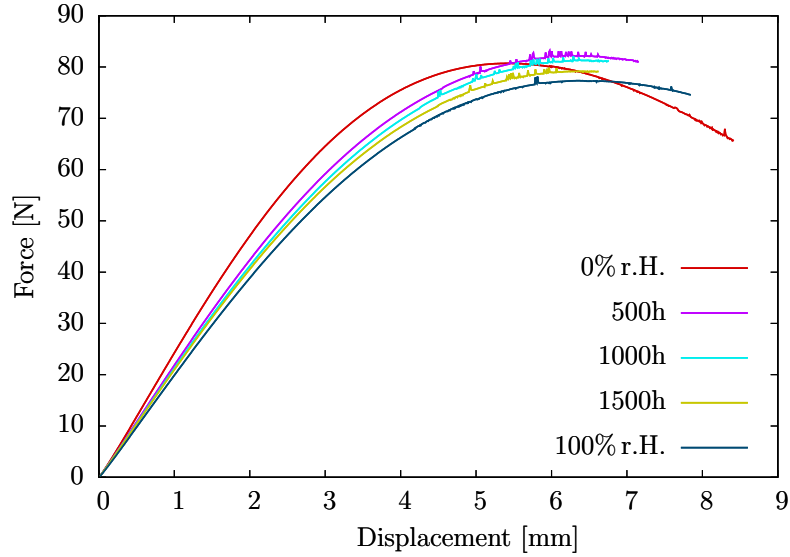


Figure 8.9: Load-Displacement comparison of the samples aged from 500h to 1500h with the dry and saturated sample for 100% r.H. at 60 °C

ulated in Table 8.4. The tear strength increases as the material is exposed to a humid atmosphere for 500h. Further ageing leads to a decrease in the tear strength of the material. The dry shows higher tear strength than the saturated sample at 100% r.H. However, the elongation of the saturated sample is higher in comparison due to the increased material's ductility. The ductile behaviour also depends on the moisture distribution, where the material's ductility is maximum for 1000h aged sample and decreases with further ageing of the material until saturation.

Table 8.4: Maximum load-displacement data of the sample aged at 100%r.H. at an isothermal condition of 60 °C

Load-Displacement					
	0% r.H.	500h	1000h	1500h	100% r.H.
Displacement [mm]	5.427	5.976	6.291	5.967	5.814
Load [N]	80.709	83.159	82.143	79.881	78.125

9

Summary and outlook

9.1 Summary

This thesis aims to develop a desired material model to analyse the ageing in crosslinked polyurethane adhesives under the influence of moisture. In this work, tests conducted on the diffusion and mechanical behaviour under isothermal conditions at 60° C are carried out at Lehrstuhl für Adhäsion und Interphasen in Polymeren, Saarland University and Fraunhofer-Institut für Fertigungstechnik und Angewandte Materialforschung (IFAM), Bremen. The moisture diffusion is investigated on two commercial adhesive materials referred to as adhesive-A and adhesive-B, whereas the tensile and fracture behaviour is investigated only on adhesive-A.

The dynamic vapour sorption method investigates moisture transport in the adhesive samples for different humidity conditions at an isothermal condition. Initially, adhesive samples are placed in a climate chamber until the saturation state is reached to record moisture uptake in absorption. Once the samples reach saturation, the atmosphere in the climate chamber is shifted to dry air to measure mass release in desorption.

The Langmuir-type diffusion model is used to analyse moisture diffusion in selected adhesive materials. Material parameters of the diffusion model are identified to simulate moisture diffusion for different saturation states in the adhesive-A sample. Kinetics of the moisture absorption and desorption in adhesive-B follow different profiles since the chemical potential of the material is the driving force of diffusion but not the concentration gradient. Therefore, the material parameters for absorption and desorption behaviours are identified individually. Concentration-dependent diffusion parameters depend on the boundary conditions used in the Langmuir-type diffusion model to analyse non-linear moisture diffusion in adhesive-B.

The nearly incompressible finite-strain viscoelastic behaviour of the crosslinked polyurethane is modelled based on the rheological properties considering the material's elastic and viscous parts. This material model is modelled by considering four Maxwell elements connected in parallel to the elastic spring component. An evolution equation is used to compute the deformation in the elastic spring element of the Maxwell element. The constitutive equations for stresses defined in Chapter 3 were used to implement the finite-strain viscoelastic model in the open-source finite element library deal.II programmed in C++.

The moisture diffusion in the polyurethane adhesive results in the ageing of the material leading to softening of the material because of the decay in the stiffness. In order to investigate the ageing process, the finite-strain viscoelastic material model is coupled with the Langmuir-type diffusion model. The softening of the material due to the ageing is considered in numerical simulation by using moisture-dependent stiffness parameters. The moisture-dependent stiffness parameters are calculated by interpolating the dry and saturated stiffness parameters using an exponential decay function. The coupled material model is solved using a staggered method, where the Langmuir-type diffusion is solved in the first step, and the finite-strain viscoelastic model is solved using the Newtons method.

The fracture behaviour in crosslinked polyurethane adhesives is modelled with the phase-field damage model under large deformations. The finite-strain phase-field model was modelled by coupling the finite-strain viscoelastic material model with a crack propagation model based on Griffith's theory. A numerical investigation of the finite-strain phase-field damage model is carried out on the angular specimen described in DIN ISO 34-1 to evaluate the tear strength of the adhesive-A specimen. Aged samples are used in the experimental investigation to understand the influence of moisture on fracture

behaviour in crosslinked polyurethane adhesives. Finally, the finite-strain phase-field damage model is coupled with the Langmuir-type diffusion model to understand moisture's influence on adhesive-A's fracture toughness.

The material parameters required for the numerical simulation are identified using the gradient-free algorithm proposed by Nelder & Mead. The simulation results are compared with the experimental results to validate the identified material parameters. Finally, the material models corresponding to the coupled diffusion-deformation and diffusion-deformation-damage are investigated numerically. The numerical results are compared with the experimental data to check for the validity of the proposed material models.

9.2 Outlook for the future work

Environmental conditions like temperature and humidity influence the crosslinked polyurethane adhesives. The present work is focused mainly on the influence of local moisture concentration transported into the material at an isothermal condition. However, temperature influences moisture diffusion, hence it is necessary to investigate temperature influence to identify temperature-dependent material parameters with Arrhenius law. The diffusion tests conducted on the adhesive-B show that moisture absorption and desorption kinetic follow different paths. Therefore further investigation on the chemical potential of the adhesive-B is necessary to formulate a diffusion equation that can be used to simulate absorption and desorption behaviour with unique material parameters.

This work focuses on modelling the finite-strain viscoelasticity using phenomenological material model. The material models based on the phenomenological theories are formulated from the empirical relation derived from the experimental data and observation. The parameters of phenomenological models are identified by fitting the experimental data and have no relevance to the material's molecular structure. Therefore, the micromechanical network models need to be formulated based on the statistical mechanics with a motivation to describe the complex micromechanical behaviour. 8-chain model [20, 8] and the micro-sphere model [99, 98, 44] are some of the popular micromechanical network material models to investigate polymer network materials.

Coupled material model for diffusion and finite-strain viscoelasticity can capture the effects of local moisture concentration on mechanical behaviour. However, the coupled material model does not account for the swelling in the material on account of moisture diffusion. The swelling deformation can be accounted for by considering the multiplicative decomposition of the deformation into swelling and mechanical deformations. The multiplicative decomposition of the deformation gradient requires experimental investigations that measure swelling strains. The presented multi-physically coupled material model does not consider the influence of mechanical deformation on diffusion. Thus the material model cannot capture bending effects on the moisture distribution.

In this work, the study of modelling fracture is restricted to Mode I failure. The parameters obtained for Mode I failure can not be used in Mode II and Mode III failure simulation. The experimental investigation are needed to identify critical fracture energy of Mode II and Mode III for the phase-field fracture simulation. The experiment and simulation in the current work only help us understand some aspects of the ageing process under the influence of moisture. The material models presented in this work provide a significant basis for further consideration in material modelling for the future work. This prospect of work will enable a more precise understanding of ageing in the crosslinked polyurethane adhesives at different isothermal conditions.

Bibliography

- [1] ALAM, M., AND BAILEY, C. 1 - introduction to adhesives joining technology for electronics. In *Advanced Adhesives in Electronics*, M. O. Alam and C. Bailey, Eds., Woodhead Publishing Series in Electronic and Optical Materials. Woodhead Publishing, 2011, pp. 1–12.
- [2] ALFREY, T., GURNEE, E. F., AND LLOYD, W. G. Diffusion in glassy polymers. *Journal of Polymer Science Part C: Polymer Symposia* 12, 1 (1966), 249–261.
- [3] AMBATI, M., AND DE LORENZIS, L. Phase-field modeling of brittle and ductile fracture in shells with isogeometric nurbs-based solid-shell elements. *Computer Methods in Applied Mechanics and Engineering* 312 (2016), 351–373.
- [4] AMBATI, M., GERASIMOV, T., AND DE LORENZIS, L. Phase-field modeling of ductile fracture. *Mechanics Research Communications* 55 (2015), 1017–1040.
- [5] ANAND, L. A constitutive model for compressible elastomeric solids. *Computational Mechanics* 18 (1996), 339–355.
- [6] ARANSON, I. S., KALATSKY, V. A., AND VINOKUR, V. M. Continuum field description of crack propagation. *Phys. Rev. Lett.* 85 (2000), 118–121.
- [7] ARNDT, D., BANGERTH, W., DAVYDOV, D., HEISTER, T., HELTAI, L., KRONBICHLER, M., MAIER, M., PELTERET, J.-P., TURCK SIN, B., AND WELLS, W. The deal.ii library, version 8.5. *Journal of Numerical Mathematics* 25 (2017), 137–145.

-
- [8] ARRUDA, E. M., AND BOYCE, M. C. A three-dimensional constitutive model for the large stretch behavior of rubber elastic materials. *Journal of the Mechanics and Physics of Solids* 41, 2 (1993), 389–412.
- [9] ARSLANOV, V., AND OGAREV, V. Adhesive joints of light metals with polymers. *Progress in Organic Coatings* 15 (1987), 1–31.
- [10] AWAJA, F., GILBERT, M., KELLY, G., FOX, B., AND PIGRAM, P. J. Adhesion of polymers. *Progress in Polymer Science* 34, 9 (2009), 948–968.
- [11] BANGERTH, W., HARTMANN, R., AND KANSCHAT, G. deal.ii – a general purpose object oriented finite element library. *ACM Transactions on Mathematical Software* 33 (2007), 24.
- [12] BATHE, K. J. *Finite element procedures*. Prentice Hall, Pearson Education, Inc., 2014.
- [13] BENZARTI, K., CHATAIGNER, S., QUIERTANT, M., MARTY, C., AND AUBAGNAC, C. Accelerated ageing behaviour of the adhesive bond between concrete specimens and cfrp overlays. *Construction and Building Materials* 25, 2 (2011), 523–538. Composite Materials and Adhesive Bonding Technology.
- [14] BISCHOFF, J. E., ARRUDA, E. A., AND GROSH, K. A microstructurally based orthotropic hyperelastic constitutive law. *Journal of Applied Mechanics* 69, 5 (08 2002), 570–579.
- [15] BJÖRCK, A. *Numerical Methods for Least Squares Problems*. Society for Industrial and Applied Mathematics, 1996.
- [16] BONET, J., AND WOOD, R. D. *Nonlinear Continuum Mechanics for Finite Element Analysis*, 2 ed. Cambridge University Press, 2008.
- [17] BORDEN, M. J., VERHOOSSEL, C. V., SCOTT, M. A., HUGHES, T. J., AND LANDIS, C. M. A phase-field description of dynamic brittle fracture. *Computer Methods in Applied Mechanics and Engineering* 217-220 (2012), 77–95.
- [18] BOURDIN, B., FRANCFORT, G., AND MARIGO, J.-J. Numerical experiments in revisited brittle fracture. *Journal of the Mechanics and Physics of Solids* 48, 4 (2000), 797–826.
- [19] BOURDIN, B., FRANCFORT, G. A., AND MARIGO, J.-J. The variational approach to fracture. *Journal of Elasticity* 91 (2008), 5–148.

-
- [20] BOYCE, M. C., AND ARRUDA, E. M. Constitutive models of rubber elasticity: A review. *Rubber Chemistry and Technology* 73, 3 (2000), 504–523.
- [21] BRAIDES, A. *Approximation of Free-Discontinuity Problems*. Springer-Verlag Berlin Heidelberg, 2000.
- [22] BRINK, U., AND STEIN, E. On some mixed finite element methods for incompressible and nearly incompressible finite elasticity. *Rubber Chemistry and Technology* 19 (1996), 105–119.
- [23] CARTER, H., AND KIBLER, K. Langmuir-type model for anomalous moisture diffusion in composite resins. *Journal of Composite Materials* 12 (1978), 118–131.
- [24] CHARLOTTE, K. *Numerical and Analytical Investigation of a Phase Field Model for Fracture*. Dissertation, Lehrstuhl für Technische Mechanik, Technischen Universität Kaiserslautern, 2013.
- [25] CHARLOTTE, K., AND MÜLLER, R. A continuum phase field model for fracture. *Engineering Fracture Mechanics* 77, 18 (2010), 3625–3634.
- [26] CHO, K. S. *Viscoelasticity of Polymers*. Springer, 2016.
- [27] COLE, G., AND SHERMAN, A. Light weight materials for automotive applications. *Materials Characterization* 35, 1 (1995), 3–9.
- [28] COLEMAN, B. D., AND NOLL, W. The thermodynamics of elastic materials with heat conduction and viscosity. *Archive for Rational Mechanics and Analysis* 13 (1963), 167–178.
- [29] CORSON, F., ADDA-BEDIA, M., HENRY, H., AND KATZAV, E. Thermal fracture as a framework for quasi-static crack propagation. *International Journal of Fracture* 158 (2009), 1–14.
- [30] CRANK, J. A theoretical investigation of the influence of molecular relaxation and internal stress on diffusion in polymers. *Journal of Polymer Science* 11, 2 (1953), 151–168.
- [31] CRANK, J. *The Mathematics of Diffusion*. Oxford science publications. Clarendon Press, 1979.
- [32] CRANK, J., AND NICOLSON, P. A practical method for numerical evaluation of solutions of partial differential equations of the heat-conduction type. *Mathematical Proceedings of the Cambridge Philosophical Society* 43, 1 (1947), 50–67.

- [33] DAS, A., AND MAHANWAR, P. A brief discussion on advances in polyurethane applications. *Advanced Industrial and Engineering Polymer Research 3* (2020), 93 – 101.
- [34] DIEBELS, S. *Kontinuumsmechanik*. Lehrstuhl für Technische Mechanik, 2016.
- [35] DUDA, F. P., CIARBONETTI, A., P., S. F., AND E., H. A. A phase-field/gradient damage model for brittle fracture in elastic–plastic solids. *International Journal of Plasticity 65* (2015), 269–296.
- [36] EASTGATE, L. O., SETHNA, J., RAUSCHER, M., CRETEGNY, T., CHEN, C., AND MYERS, C. Fracture in mode i using a conserved phase-field model. *Physical review. E, Statistical, nonlinear, and soft matter physics 65 3 Pt 2A* (2002), 036117.
- [37] FERNANDES, R., DE MOURA, M., AND MOREIRA, R. Effect of moisture on pure mode i and ii fracture behaviour of composite bonded joints. *International Journal of Adhesion and Adhesives 68* (2016), 30–38.
- [38] FICK, A. Über diffusion. *Annalen der Physik 170*, 1 (1855), 59–86.
- [39] FLORY, P. J. Thermodynamic relations for high elastic materials. *Transactions of the Faraday Society 57* (1961), 829–838.
- [40] FRANCFORT, G., AND MARIGO, J.-J. Revisiting brittle fracture as an energy minimization problem. *Journal of the Mechanics and Physics of Solids 46*, 8 (1998), 1319–1342.
- [41] FREUNDLICH, H. M. F. Over the adsorption in solution. *The Journal of Physical Chemistry 57* (1906), 385–471.
- [42] FRIED, E., AND GURTIN, M. E. Continuum theory of thermally induced phase transitions based on an order parameter. *Physica D: Nonlinear Phenomena 68*, 3 (1993), 326–343.
- [43] FRIED, E., AND GURTIN, M. E. Dynamic solid-solid transitions with phase characterized by an order parameter. *Phys. D 72*, 4 (may 1994), 287–308.
- [44] GÖKTEPE, S., AND MIEHE, C. A micro–macro approach to rubber-like materials. part iii: The micro-sphere model of anisotropic mullins-type damage. *Journal of the Mechanics and Physics of Solids 53*, 10 (2005), 2259–2283.

- [45] GOLDSCHMIDT, F. *Modellierung und Simulation von Klebeverbindungen mit gradierten mechanischen Eigenschaften*. Dissertation, Lehrstuhl für Technische Mechanik, Universität des Saarlandes, 2011.
- [46] GOLDSCHMIDT, F., AND DIEBELS, S. Modelling and numerical investigations of the mechanical behavior of polyurethane under the influence of moisture. *Archive of Applied Mechanics* 85 (2015), 1035–1042.
- [47] GOLDSCHMIDT, F., DIEBELS, S., SCHERFF, F., DEPOLLIER, L., HUACUJA-SANCHEZ, J. E., AND POSSART, W. *Viscoelasticity in Ageing Joints – Experiments and Simulation*. John Wiley & Sons, Ltd, 2018, ch. B.6, pp. 355–374.
- [48] GOVINDJEE, S., AND REESE, S. A presentation and comparison of two large deformation viscoelasticity models. *Journal of Engineering Materials and Technology* 119, 3 (07 1997), 251–255.
- [49] GRELLMANN, W., AND LANGER, B., Eds. *Deformation and Fracture Behaviour of Polymer Materials*, 1 ed., vol. 247. Springer International Publishing, 2017.
- [50] GREVE, R. *Kontinuumsmechanik: Ein Grundkurs für Ingenieure und Physiker*. Springer, 2003.
- [51] GRIFFITH, A. A. The phenomena of rupture and flow in solids. *Philosophical Transactions of the Royal Society of London. Series A, Containing Papers of a Mathematical or Physical Character* 221 (1921), 163–198.
- [52] GROSS, D., AND SEELIG, T. *Linear fracture mechanics*. Springer Berlin Heidelberg, Berlin, Heidelberg, 2011, pp. 63–144.
- [53] GRUBER, E. L. g. e. struik: Physical aging in amorphous polymers and other materials. elsevier sci. publ. comp., amsterdam-oxford-new york 1978. 229 seiten, 141 abbildungen, preis: Us \$ 42,50, holl. gulden 97,50. *Berichte der Bunsengesellschaft für physikalische Chemie* 82, 9 (1978), 1019–1019.
- [54] GURTIN, M. E. Generalized ginzburg-landau and cahn-hilliard equations based on a microforce balance. *Physica D: Nonlinear Phenomena* 92, 3 (1996), 178–192.

-
- [55] HARTMANN, S. Computation in finite-strain viscoelasticity: finite elements based on the interpretation as differential–algebraic equations. *Computer Methods in Applied Mechanics and Engineering* 191, 13 (2002), 1439–1470.
- [56] HAUPT, P. *Continuum Mechanics and Theory of Materials*. Springer-Verlag Berlin Heidelberg, 2002.
- [57] HAUPT, P., AND LION, A. On finite linear viscoelasticity of incompressible isotropic materials. *Acta Mechanica* 159 (2002), 87–124.
- [58] HAUPT, P., LION, A., AND BACKHAUS, E. On the dynamic behaviour of polymers under finite strains: constitutive modelling and identification of parameters. *International Journal of Solids and Structures* 37, 26 (2000), 3633–3646.
- [59] HAUPT, P., AND SEDLAN, K. Viscoplasticity of elastomeric materials: experimental facts and constitutive modelling. *Archive of Applied Mechanics* 71 (2001), 89–109.
- [60] HEISTER, T., WHEELER, M. F., AND WICK, T. A primal-dual active set method and predictor-corrector mesh adaptivity for computing fracture propagation using a phase-field approach. *Computer Methods in Applied Mechanics and Engineering* 290 (2015), 466–495.
- [61] HENGDI, S., HUIXIAN, Y., AND JIN, B. Finite element method for coupled diffusion-deformation theory in polymeric gel based on slip-link model. *Applied Mathematics and Mechanics* 39 (2018), 581–596.
- [62] HOFACKER, M., AND MIEHE, C. A phase field model for ductile to brittle failure mode transition. *PAMM* 12, 1 (2012), 173–174.
- [63] HOLZAPFEL, G. A. *Nonlinear Solid Mechanics: A Continuum Approach for Engineering*. Wiley, 2000.
- [64] HOLZAPFEL, G. A., GASSER, T., AND OGDEN, R. W. A new constitutive framework for arterial wall mechanics and a comparative study of material models. *Journal of elasticity* 61, 1-3 (2000), 1–48.
- [65] HOSSAIN, M., HSUEH, C.-J., BOURDIN, B., AND BHATTACHARYA, K. Effective toughness of heterogeneous media. *Journal of the Mechanics and Physics of Solids* 71 (2014), 15–32.

- [66] HUA, Y., CROCOMBE, A., WAHAB, M., AND ASHCROFT, I. Continuum damage modelling of environmental degradation in joints bonded with ea9321 epoxy adhesive. *International Journal of Adhesion and Adhesives* 28, 6 (2008), 302–313.
- [67] HUÁCUJA-SANCHEZ, J., MÜLLER, K., AND POSSART, W. Water diffusion in a crosslinked polyether-based polyurethane adhesive. *International Journal of Adhesion and Adhesives* 66 (2016), 167–175.
- [68] HUTCHINSON, J. M. Physical aging of polymers. *Progress in Polymer Science* 20, 4 (1995), 703–760.
- [69] JERZY, P. The criterion for determining the direction of crack propagation in a random pattern composites. *Progress in Organic Coatings* 52 (2017), 1923–1934.
- [70] JOHLITZ, M. *Experimentelle Untersuchung und Modellierung von Maßstabeffekten in Klebungen*. Dissertation, Lehrstuhl für Technische Mechanik, Universität des Saarlandes, 2008.
- [71] JOHLITZ, M. *Numerical Methods for Least Squares Problems*. Dissertation, Lehrstuhl für Technische Mechanik, Universität des Saarlandes, 2008.
- [72] JOHLITZ, M. *Materialmodellierung*. Script, Lehrstuhl für Technische Mechanik, Universität des Saarlandes, 2009.
- [73] JOHLITZ, M., DIEBELS, S., AND POSSART, W. Investigation of the thermoviscoelastic material behaviour of adhesive bonds close to the glass transition temperature. *Archive of Applied Mechanics* 82 (2012), 1089–1102.
- [74] JOHLITZ, M., AND LION, A. Chemo-thermomechanical ageing of elastomers based on multiphase continuum mechanics. *Continuum Mechanics and Thermodynamics* 25 (2013), 605–624.
- [75] JOLIFF, Y., BELEC, L., AND CHAILAN, J. Modified water diffusion kinetics in an unidirectional glass/fibre composite due to the interphase area: Experimental, analytical and numerical approach. *Composite Structures* 97 (2013), 296–303.
- [76] KALISKE, M. A formulation of elasticity and viscoelasticity for fibre reinforced material at small and finite strains. *Computer Methods in Applied Mechanics and Engineering* 185, 2 (2000), 225–243.

- [77] KALISKE, M., AND ROTHERT, H. On the finite element implementation of rubber-like materials at finite strains. *Engineering Computations* 14, 2 (1997), 216–232.
- [78] KARMA, A., KESSLER, D. A., AND LEVINE, H. Phase-field model of mode iii dynamic fracture. *Phys. Rev. Lett.* 87 (2001), 045501.
- [79] KERN, M., AND WEGNER, S. M. Bonding to zirconia ceramic: adhesion methods and their durability. *Dental materials : official publication of the Academy of Dental Materials* 14, 1 (1998), 64–71.
- [80] KLAUS, F., AND ABDULHAKIM, A. A. Manufacturing aspects of advanced polymer composites for automotive applications. *Applied Composite Materials* 20, 2 (2013), 107–128.
- [81] KRAJCIKOVIC, D., AND LEMAITRE, J., Eds. *Continuum Damage Mechanics Theory and Application*. Springer-Verlag Wien, 1987.
- [82] KUHN, C., AND MÜLLER, R. A continuum phase field model for fracture. *Engineering Fracture Mechanics* 77, 18 (2010), 3625–3634.
- [83] KUHN, C., SCHLÜTER, A., AND MÜLLER, R. On degradation functions in phase field fracture models. *Computational Materials Science* 108 (2015), 374–384.
- [84] KUHN, C., SCHLÜTER, A., AND MÜLLER, R. On degradation functions in phase field fracture models. *Computational Materials Science* 108 (2015), 374–384. Selected Articles from Phase-field Method 2014 International Seminar.
- [85] LAI, M., KREMPL, E., AND RUBIN, D. *Introduction to Continuum Mechanics*. Elsevier, 1994.
- [86] LE TALLEC, P., AND RAHLER, C. Numerical models of steady rolling for non-linear viscoelastic structures in finite deformations. *International Journal for Numerical Methods in Engineering* 37, 7 (1994), 1159–1186.
- [87] LEE, E., AND LIU, D. Finite strain elastic plastic theory with application to plane wave analysis. *Journal of Applied Physics* 38 (1967), 19–27.
- [88] LEE, E. H. Elastic-plastic deformation at finite strains. *Journal of Applied Mechanics* 36, 1 (1969), 1–6.

- [89] LION, A. A physically based method to represent the thermo-mechanical behaviour of elastomers. *Acta Mechanica* 123 (1997), 1–25.
- [90] LION, A. *Thermomechanik von Elastomeren*. 12 2000.
- [91] LUBARDA, V. A. Constitutive theories based on the multiplicative decomposition of deformation gradient: Thermoelasticity, elastoplasticity, and biomechanics. *Applied Mechanics Reviews* 57, 2 (04 2004), 95–108.
- [92] LUBLINER, J. A model of rubber viscoelasticity. *Mechanics Research Communications* 12 (1985), 93–99.
- [93] MARIAM, M., AFENDI, M., ABDUL MAJID, M. S., RIDZUAN, M. J. M., AZMI, A. I., AND SULTAN, M. T. H. Influence of hydrothermal ageing on the mechanical properties of an adhesively bonded joint with different adherends. *Composites Part B: Engineering* 165 (2019), 572–585.
- [94] MARQUES, S. P. C., AND CREUS, G. J. *Computational Viscoelasticity*. Springer, 2012.
- [95] MAZUMDER, S. Chapter 5 - treatment of the time derivative (parabolic and hyperbolic pdes). In *Numerical Methods for Partial Differential Equations*, S. Mazumder, Ed. Academic Press, 2016, pp. 219–275.
- [96] MEISER, A., WILLSTRAND, K., FEHLING, P., AND POSSART, W. Chemical aging in epoxies: A local study of the interphases to air and to metals. *The Journal of Adhesion* 84, 4 (2008), 299–321.
- [97] MIEHE, C., ALDAKHEEL, F., AND RAINA, A. Phase field modeling of ductile fracture at finite strains: A variational gradient-extended plasticity-damage theory. *International Journal of Plasticity* 84 (2016), 1–32.
- [98] MIEHE, C., AND GÖKTEPE, S. A micro–macro approach to rubber-like materials. part ii: The micro-sphere model of finite rubber viscoelasticity. *Journal of the Mechanics and Physics of Solids* 53, 10 (2005), 2231–2258.
- [99] MIEHE, C., GÖKTEPE, S., AND LULEI, F. A micro-macro approach to rubber-like materials-part i: the non-affine micro-sphere model of rubber elasticity. *Journal of the Mechanics and Physics of Solids* 52, 11 (2004), 2617–2660.

-
- [100] MIEHE, C., HOFACKER, M., SCHÄNZEL, L.-M., AND ALDAKHEEL, F. Phase field modeling of fracture in multi-physics problems. part ii. coupled brittle-to-ductile failure criteria and crack propagation in thermo-elastic-plastic solids. *Computer Methods in Applied Mechanics and Engineering* 294 (2015), 486–522.
- [101] MIEHE, C., AND KECK, J. Superimposed finite elastic-viscoelastic-plastoelastic stress response with damage in filled rubbery polymers. experiments, modelling and algorithmic implementation. *Journal of the Mechanics and Physics of Solids* 48, 2 (2000), 323–365.
- [102] MIEHE, C., SCHÄNZEL, L.-M., AND ULMER, H. Phase field modeling of fracture in multi-physics problems. part i. balance of crack surface and failure criteria for brittle crack propagation in thermo-elastic solids. *Computer Methods in Applied Mechanics and Engineering* 294 (2015), 449–485.
- [103] MIEHE, C., WELSCHINGER, F., AND HOFACKER, M. Thermodynamically consistent phase-field models of fracture: Variational principles and multi-field fe implementations. *International Journal for Numerical Methods in Engineering* 83, 10 (2010), 1273–1311.
- [104] MIN-YOUNG, L., AND TAE GYUN, C. Research trends in polymer materials for use in lightweight vehicles. *International Journal of Precision Engineering and Manufacturing* 16, 1 (2015), 213–220.
- [105] MOONEY, M. A theory of large elastic deformation. *Journal of Applied Physics* 11, 9 (1940), 582–592.
- [106] MORTON, E. G., AND CHIKAYOSHI, Y. On a model for two phase diffusion in composite materials. *Journal of Composite Materials* 13, 2 (1979), 126–130.
- [107] MUBASHAR, A., ASHCROFT, I., CRITCHLOW, G., AND CROCOMBE, A. Moisture absorption-desorption effects in adhesive joints. *International Journal of Adhesion and Adhesives* 29, 8 (2009), 751–760.
- [108] NAVIDTEHRANI, Y., BETEGÓN, C., AND MARTÍNEZ-PAÑEDA, E. A unified abaqus implementation of the phase field fracture method using only a user material subroutine. *Materials* 14, 8 (2021).
- [109] NELDER, J. A., AND MEAD, R. A simplex method for function minimization. *The Computer Journal* 7 (1965), 308–313.

-
- [110] ÖCHSNER, A. *Continuum Damage and Fracture Mechanics*, 1 ed. Springer Singapore, 2016.
- [111] ODEN, J. A theory of penalty methods for finite element approximations of highly nonlinear problems in continuum mechanics. *Computers & Structures* 8, 3 (1978), 445–449.
- [112] OGDEN, R. W., AND HILL, R. Large deformation isotropic elasticity - on the correlation of theory and experiment for incompressible rubber-like solids. *Proceedings of the Royal Society of London. A. Mathematical and Physical Sciences* 326, 1567 (1972), 565–584.
- [113] OGDEN, R. W., AND STERNBERG, E. Nonlinear elastic deformations. *Journal of Applied Mechanics* 52, 3 (09 1985), 740–741.
- [114] PELTERET, J.-P., DAVYDOV, D., MCBRIDE, A., VU, D. K., AND STEINMANN, P. Computational electro-elasticity and magneto-elasticity for quasi-incompressible media immersed in free space. *International Journal for Numerical Methods in Engineering* 108, 11 (2016), 1307–1342.
- [115] PEREZ, N. *Introduction to Fracture Mechanics*. Springer International Publishing, Cham, 2017, pp. 53–77.
- [116] PETHRICK, R. A. Design and ageing of adhesives for structural adhesive bonding – a review. *Proceedings of the Institution of Mechanical Engineers, Part L: Journal of Materials: Design and Applications* 229, 5 (2015), 349–379.
- [117] PLACETTE, M. D., FAN, X., ZHAO, J.-H., AND EDWARDS, D. Dual stage modeling of moisture absorption and desorption in epoxy mold compounds. *Microelectronics Reliability* 52 (2012), 1401–1408.
- [118] QUINN, F. X., KAMPFF, E., SMYTH, G., AND MCBRIERTY, V. J. Water in hydrogels. 1. a study of water in poly(n-vinyl-2-pyrrolidone/methyl methacrylate) copolymer. *Macromolecules* 21, 11 (1988), 3191–3198.
- [119] RANZ, T. *Elementare Materialmodelle der Linearen Viskoelastizität im Zeitbereich*. Universität der Bundeswehr München, 2007.
- [120] REDDY, J. N. *An Introduction to Continuum Mechanics*, 2 ed. Cambridge University Press, 2013.

-
- [121] REESE, S., AND GOVINDJEE, S. Theoretical and numerical aspects in the thermo-viscoelastic material behaviour of rubber-like polymers. *Mechanics of Time-Dependent Materials 1* (1997), 357–396.
- [122] REESE, S., AND GOVINDJEE, S. A theory of finite viscoelasticity and numerical aspects. *International Journal of Solids and Structures 35* (1998), 3455–3482.
- [123] RIVLIN, R. S., AND RIDEAL, E. K. Large elastic deformations of isotropic materials iv. further developments of the general theory. *Philosophical Transactions of the Royal Society of London. Series A, Mathematical and Physical Sciences 241*, 835 (1948), 379–397.
- [124] RIVLIN, R. S., SAUNDERS, D. W., AND ANDRADE, E. N. D. C. Large elastic deformations of isotropic materials vii. experiments on the deformation of rubber. *Philosophical Transactions of the Royal Society of London. Series A, Mathematical and Physical Sciences 243*, 865 (1951), 251–288.
- [125] RODRIGUES, T. A. F., CHAVES, F. J. P., SILVA, L. F. M. D., COSTA, M., AND BARBOSA, A. Q. Determination of the fracture envelope of an adhesive joint as a function of moisture. *Materialwissenschaft und Werkstofftechnik 48*, 11 (2017), 1181–1190.
- [126] SAAD, Y. A flexible inner-outer preconditioned gmres algorithm. *SIAM Journal on Scientific Computing 14*, 2 (1993), 461–469.
- [127] SANOPOULOU, M., STAMATIALIS, D. F., AND PETROPOULOS, J. H. Investigation of case ii diffusion behavior. 1. theoretical studies based on the relaxation dependent solubility model. *Macromolecules 35*, 3 (2002), 1012–1020.
- [128] SELDAN, K. *Viskoelastisches Materialverhalten von Elastomerwerkstoffen: Experimentelle Untersuchung und Modellbildung*. Dissertation, Berichte des Institut für Mechanik (Bericht 2/2001), Universität Gesamthochschule Kassel, 2000.
- [129] SEYMOUR, R. B., AND KAUFFMAN, G. B. Polyurethanes: A class of modern versatile materials. *Journal of Chemical Education 69* (1992), 909.
- [130] SHARMA, P., SAMBALE, A., STOMMEL, M., MAISL, M., HERMANN, H.-G., AND DIEBELS, S. Moisture transport in pa6 and its influence on the mechanical properties. *Continuum Mechanics and Thermodynamics 32* (2020), 307 – 325.

- [131] SIKORSKI, M. E. The adhesion of metals and factors that influence it. *Wear* 7, 2 (1964), 144–162.
- [132] SIMO, J. On a fully three-dimensional finite-strain viscoelastic damage model: Formulation and computational aspects. *Computer Methods in Applied Mechanics and Engineering* 60, 2 (1987), 153–173.
- [133] SIPS, R. The structure of a catalyst surface. *The Journal of Chemical Physics* 16 (1948), 490–495.
- [134] SMYTH, G., QUINN, F. X., AND MCBRIERTY, V. J. Water in hydrogels. 2. a study of water in poly(hydroxyethyl methacrylate). *Macromolecules* 21, 11 (1988), 3198–3204.
- [135] SOUSA, M., CORREIA, R., AND FONSECA, C. Durability of an epoxy adhesive used in civil structural applications. *Construction and Building Materials* 161 (2018), 618 – 633.
- [136] SPATSCHEK, R., MÜLLER-GUGENBERGER, C., BRENER, E., AND NESTLER, B. Phase field modeling of fracture and stress-induced phase transitions. *Phys. Rev. E* 75 (2007), 066111.
- [137] STARKOVA, O., CHANDRASEKARAN, S., SCHNOOR, T., 2, SEVCENKO, J., AND SCHULTE, K. Anomalous water diffusion in epoxy/carbon nanoparticle composites. *Polymer Degradation and Stability* 164 (2019), 127 – 135.
- [138] STEEB, H., AND DIEBELS, S. Modeling thin films applying an extended continuum theory based on a scalar-valued order parameter.: Part i: isothermal case. *International Journal of Solids and Structures* 41, 18 (2004), 5071–5085.
- [139] STRUIK, L. C. E. Physical aging in plastics and other glassy materials. *Polymer Engineering & Science* 17, 3 (1977), 165–173.
- [140] SYLVAIN, P., CORINNE, R. M., CHRISTINE, S. G., AND MARTIN, E. R. Free/bound water absorption in an epoxy adhesive. *Polymer* 46, 24 (2005), 10733–10740.
- [141] TALLEC, P., RAHIER, C., AND KAISS, A. Three-dimensional incompressible viscoelasticity in large strains: Formulation and numerical approximation. *Computer Methods in Applied Mechanics and Engineering* 109 (1993), 233–258.

-
- [142] THOMAS, N. L., AND WINDLE, A. H. A theory of case ii diffusion. *Polymer* 23, 4 (1982), 529–542.
- [143] TRELOAR, L. R. G. The elasticity of a network of long-chain molecules. i. *Rubber Chemistry and Technology* 16, 4 (1943), 746–751.
- [144] TRELOAR, L. R. G. The elasticity of a network of long-chain molecules. ii. *Rubber Chemistry and Technology* 17, 2 (1944), 296–302.
- [145] TRELOAR, L. R. G. The elasticity of a network of long-chain molecules. iii. *Rubber Chemistry and Technology* 19, 4 (1946), 1009–1021.
- [146] TRELOAR, L. R. G., HOPKINS, H. G., RIVLIN, R. S., BALL, J. M., GEE, G., ALLEN, G., AND PRICE, C. The mechanics of rubber elasticity. *Proceedings of the Royal Society of London. A. Mathematical and Physical Sciences* 351, 1666 (1976), 301–330.
- [147] TRUESDELL, C., AND TOUPIN, R. *The Classical Field Theories*. Springer Berlin Heidelberg, Berlin, Heidelberg, 1960, pp. 226–858.
- [148] VIETH, W. R., HOWELL, J. M., AND HSIEH, J. H. Dual sorption theory. *Journal of Membrane Science* 1 (1976), 177–220.
- [149] VINCENT, H., AND KARMA, A. Crack path prediction in anisotropic brittle materials. *Phys. Rev. Lett.* 95 (2005), 235501.
- [150] WATSON, S. Future emerging technologies in the wind power sector: A european perspective. *Renewable and Sustainable Energy Reviews* 113 (2019), 109270.
- [151] WEI, H., XUANHE, Z., JINXIONG, Z., AND ZHIGANG, S. A theory of coupled diffusion and large deformation in polymeric gels. *Journal of the Mechanics and Physics of Solids* 56, 5 (2008), 1779–1793.
- [152] WILLIAMS, J. G. *Fracture Mechanics of Polymers and Adhesives*. Springer Netherlands, Dordrecht, 1987, pp. 227–255.
- [153] WU, P., AND VAN DER GIESSEN, E. On improved network models for rubber elasticity and their applications to orientation hardening in glassy polymers. *Journal of the Mechanics and Physics of Solids* 41, 3 (1993), 427–456.

-
- [154] WULF, A., HESEBECK, O., KOSCHEK, K., M. BREDE, MAYER, B., JOSYULA, S., DIEBELS, S., ZIMMER, B., AND POSSART, W. Berechnung des instationären mechanischen verhaltens von alternden klebverbindungen unter einfluss von wasser auf den klebstoff. *DVS Forschungsvereinigung 469* (2021), 0–266.
- [155] YACOBI, B. G., MARTIN, S., DAVIS, K., HUDSON, A., AND HUBERT, M. Adhesive bonding in microelectronics and photonics. *Journal of Applied Physics 91*, 10 (2002), 6227–6262.
- [156] YANG, Y., YU, G., CHA, J. J., WU, H., VOSGUERITCHIAN, M., YAO, Y., BAO, Z., AND CUI, Y. Improving the performance of lithium–sulfur batteries by conductive polymer coating. *ACS Nano 5*, 11 (2011), 9187–9193. PMID: 21995642.
- [157] YEOH, O. H. Characterization of elastic properties of carbon-black-filled rubber vulcanizates. *Rubber Chemistry and Technology 63*, 5 (11 1990), 792–805.
- [158] YEOH, O. H. Some forms of the strain energy function for rubber. *Rubber Chemistry and Technology 66*, 5 (11 1993), 754–771.
- [159] ZIENKIEWICZ, O. C., AND TAYLOR, R. L. *The finite element method: basic formulation and linear problems*, vol. 1. McGraw-Hill, 1994.
- [160] ZIENKIEWICZ, O. C., AND TAYLOR, R. L. *The finite element method: solid mechanics*, vol. 2. McGraw-Hill, 2000.

A

Theoretical Background

A.1 Stress and elasticity tensors

The free energy density function used in the definition of the viscoelastic material models is dependent on the left Cauchy-Green deformation tensor. The stresses and tangent operators required to implement a material model in the material configuration need to be derived [76, 77]. The general formulation to derive Kirchhoff stresses is discussed with the help of the equation (3.42) using the relationship between Kirchhoff and Cauchy stress tensors

$$\begin{aligned}\boldsymbol{\tau} &= 2\mathbf{B} \cdot \frac{\partial W\left(\bar{\mathbf{I}}_1^{\mathbf{B}}, \bar{\mathbf{I}}_1^{\mathbf{B}_e^j}, J, m\right)}{\partial \mathbf{B}} = \boldsymbol{\tau}_{\text{vol}} + \boldsymbol{\tau}_{\text{eq}} + \sum_{j=1}^n \boldsymbol{\tau}_{\text{neq}}^j \\ \boldsymbol{\tau}_{\text{eq}} &= 2\mathbf{B} \cdot \frac{\partial W_{\text{eq}}\left(\bar{\mathbf{I}}_1^{\mathbf{B}}, m\right)}{\partial \mathbf{B}}; \quad \boldsymbol{\tau}_{\text{vol}} = 2\mathbf{B} \cdot \frac{\partial W_{\text{vol}}(J, m)}{\partial \mathbf{B}}; \\ \boldsymbol{\tau}_{\text{neq}}^j &= 2\bar{\mathbf{B}}_e^j \cdot \frac{\partial W_{\text{neq}}\left(\bar{\mathbf{I}}_1^{\mathbf{B}_e^j}, m\right)}{\partial \bar{\mathbf{B}}_e^j}.\end{aligned}\tag{A.1}$$

The necessary derivatives of invariants and tensors required to derive stress tensors with equation (A.1) are

$$\frac{\partial \bar{\mathbf{B}}}{\partial \mathbf{B}} = J^{-2/3} \left(\frac{4}{\mathbb{I}} - \frac{1}{3} \mathbf{B} \otimes \mathbf{B}^{-1} \right); \quad \frac{\partial \bar{\mathbb{I}}_1^{\bar{\mathbf{B}}}}{\partial \bar{\mathbf{B}}} = \mathbf{I}; \quad \frac{\partial J}{\partial \mathbf{B}} = \frac{1}{2} J \mathbf{B}^{-1}. \quad (\text{A.2})$$

The decoupled form of isochoric and volumetric parts of Kirchhoff stress tensor are obtained by applying the product and chain rules on the equation (A.1) and with the help of the relations given in equation (A.2) yields

$$\begin{aligned} \boldsymbol{\tau}_{\text{vol}} &= J (W_{\text{vol}}(J, m))' \mathbf{I}; \quad \boldsymbol{\tau}_{\text{eq}} = 2J^{-2/3} \left(W_{\text{eq}}(\bar{\mathbb{I}}_1^{\bar{\mathbf{B}}}, m) \right)' \left(\bar{\mathbf{B}} - \frac{1}{3} \bar{\mathbb{I}}_1^{\bar{\mathbf{B}}} \mathbf{I} \right); \\ \boldsymbol{\tau}_{\text{neq}}^j &= 2J^{-2/3} \left(W_{\text{neq}}(\bar{\mathbb{I}}_1^{\bar{\mathbf{B}}^j}, m) \right)' \left(\bar{\mathbf{B}} - \frac{1}{3} \bar{\mathbb{I}}_1^{\bar{\mathbf{B}}^j} \mathbf{I} \right). \end{aligned} \quad (\text{A.3})$$

(\bullet)' is the first order derivative of the free energy density function. These measures are derived from the free energy density functions given in the equations (3.32), (3.33) and (3.34)

$$\begin{aligned} \left(W_{\text{eq}}(\bar{\mathbb{I}}_1^{\bar{\mathbf{B}}}, m) \right)' &= \frac{\partial W_{\text{eq}}(\bar{\mathbb{I}}_1^{\bar{\mathbf{B}}}, m)}{\partial \bar{\mathbb{I}}_1^{\bar{\mathbf{B}}}} = c_{10}(m) + 2c_{20}(m) (\bar{\mathbb{I}}_1^{\bar{\mathbf{B}}} - 3) + \\ &\quad 3c_{30}(m) (\bar{\mathbb{I}}_1^{\bar{\mathbf{B}}} - 3)^2, \\ (W_{\text{vol}}(J, m))' &= \frac{\partial W_{\text{vol}}(J, m)}{\partial J} = \frac{2}{D(m)} (J - 1), \\ \left(W_{\text{neq}}(\bar{\mathbb{I}}_1^{\bar{\mathbf{B}}^j}, m) \right)' &= \frac{\partial W_{\text{neq}}(\bar{\mathbb{I}}_1^{\bar{\mathbf{B}}^j}, m)}{\partial \bar{\mathbb{I}}_1^{\bar{\mathbf{B}}^j}} = c_{10j}(m). \end{aligned} \quad (\text{A.4})$$

The derivation of the shape and volume-changing parts of the tangent tensor are the second order derivative of the free energy function

$$\begin{aligned} \overset{4}{\boldsymbol{\kappa}} &= 4\mathbf{B} \cdot \frac{\partial^2 W \left(\bar{\mathbf{I}}_1^{\bar{\mathbf{B}}}, \bar{\mathbf{I}}_1^{\bar{\mathbf{B}}^j}, J, m \right)}{\partial \mathbf{B} \partial \mathbf{B}} \cdot \mathbf{B} = \overset{4}{\boldsymbol{\kappa}}_{\text{eq}} + \overset{4}{\boldsymbol{\kappa}}_{\text{vol}} + \overset{4}{\boldsymbol{\kappa}}_{\text{neq}}^j, \\ \overset{4}{\boldsymbol{\kappa}}_{\text{eq}} &= 4\mathbf{B} \cdot \frac{\partial^2 W_{\text{eq}} \left(\bar{\mathbf{I}}_1^{\bar{\mathbf{B}}}, m \right)}{\partial \mathbf{B} \partial \mathbf{B}} \cdot \mathbf{B}; \quad \overset{4}{\boldsymbol{\kappa}}_{\text{vol}} = 4\mathbf{B} \cdot \frac{\partial^2 W_{\text{vol}} (J, m)}{\partial \mathbf{B} \partial \mathbf{B}} \cdot \mathbf{B}, \\ \overset{4}{\boldsymbol{\kappa}}_{\text{neq}}^j &= 4\bar{\mathbf{B}}_e^j \cdot \frac{\partial^2 W_{\text{neq}}^j \left(\bar{\mathbf{I}}_1^{\bar{\mathbf{B}}_e^j}, m \right)}{\partial \bar{\mathbf{B}}_e^j \partial \bar{\mathbf{B}}_e^j} \cdot \bar{\mathbf{B}}_e^j, \end{aligned} \quad (\text{A.5})$$

and are derived by applying the chain and product rule of the tensors. The tangent tensors of the shape and volume changing parts follows

$$\begin{aligned} \overset{4}{\boldsymbol{\kappa}}_{\text{eq}} &= 4 \left(W_{\text{eq}} \left(\bar{\mathbf{I}}_1^{\bar{\mathbf{B}}}, m \right) \right)' (\mathbf{I} \otimes \bar{\mathbf{B}})^{s_{24}} + 4 \left(W_{\text{eq}} \left(\bar{\mathbf{I}}_1^{\bar{\mathbf{B}}}, m \right) \right)'' (\bar{\mathbf{B}} \otimes \bar{\mathbf{B}}) - \\ &\quad \frac{4}{3} \left(\bar{\mathbf{I}}_1^{\bar{\mathbf{B}}} \left(W_{\text{eq}} \left(\bar{\mathbf{I}}_1^{\bar{\mathbf{B}}}, m \right) \right)'' + \left(W_{\text{eq}} \left(\bar{\mathbf{I}}_1^{\bar{\mathbf{B}}}, m \right) \right)' \right) (\bar{\mathbf{B}} \otimes \mathbf{I} + \mathbf{I} \otimes \bar{\mathbf{B}}) + \\ &\quad \frac{4}{9} \left(\left(\bar{\mathbf{I}}_1^{\bar{\mathbf{B}}} \right)^2 \left(W_{\text{eq}} \left(\bar{\mathbf{I}}_1^{\bar{\mathbf{B}}}, m \right) \right)'' + \bar{\mathbf{I}}_1^{\bar{\mathbf{B}}} \left(W_{\text{eq}} \left(\bar{\mathbf{I}}_1^{\bar{\mathbf{B}}}, m \right) \right)' \right) (\mathbf{I} \otimes \mathbf{I}) \\ \overset{4}{\boldsymbol{\kappa}}_{\text{vol}} &= (J^2 (W_{\text{vol}} (J, m))'' + J (W_{\text{vol}} (J, m))') \mathbf{I} \otimes \mathbf{I} \\ \overset{4}{\boldsymbol{\kappa}}_{\text{neq}}^j &= 4W'_{\text{neq}} \left(\bar{\mathbf{I}}_1^{\bar{\mathbf{B}}_e^j}, m \right) (\mathbf{I} \otimes \bar{\mathbf{B}})^{s_{24}} + 4W''_{\text{neq}} \left(\bar{\mathbf{I}}_1^{\bar{\mathbf{B}}_e^j}, m \right) (\bar{\mathbf{B}} \otimes \bar{\mathbf{B}}) - \\ &\quad \frac{4}{3} \left(\bar{\mathbf{I}}_1^{\bar{\mathbf{B}}_e^j} W''_{\text{neq}} \left(\bar{\mathbf{I}}_1^{\bar{\mathbf{B}}_e^j}, m \right) + W'_{\text{neq}} \left(\bar{\mathbf{I}}_1^{\bar{\mathbf{B}}_e^j}, m \right) \right) (\bar{\mathbf{B}} \otimes \mathbf{I} + \mathbf{I} \otimes \bar{\mathbf{B}}) + \\ &\quad \frac{4}{9} \left(\left(\bar{\mathbf{I}}_1^{\bar{\mathbf{B}}_e^j} \right)^2 W''_{\text{neq}} \left(\bar{\mathbf{I}}_1^{\bar{\mathbf{B}}_e^j}, m \right) + \bar{\mathbf{I}}_1^{\bar{\mathbf{B}}_e^j} W'_{\text{neq}} \left(\bar{\mathbf{I}}_1^{\bar{\mathbf{B}}_e^j}, m \right) \right) (\mathbf{I} \otimes \mathbf{I}). \end{aligned} \quad (\text{A.6})$$

$(\bullet)'$ is the first order derivative of the free energy given in equation (A.4) and $(\bullet)''$ is the second-order derivative of the free energy density functions. These measures are derived from the free energy density functions defined in the equations (3.32), (3.33) and (3.34)

$$\begin{aligned} \left(W_{\text{eq}} \left(\bar{\mathbf{I}}_1^{\bar{\mathbf{B}}}, m \right) \right)'' &= \frac{\partial^2 W_{\text{eq}} \left(\bar{\mathbf{I}}_1^{\bar{\mathbf{B}}}, m \right)}{\partial \bar{\mathbf{I}}_1^{\bar{\mathbf{B}}} \partial \bar{\mathbf{I}}_1^{\bar{\mathbf{B}}}} = 2c_{20}(m) + 6c_{30}(m) \left(\bar{\mathbf{I}}_1^{\bar{\mathbf{B}}} - 3 \right) \\ \left(W_{\text{vol}} (J, m) \right)'' &= \frac{\partial^2 W_{\text{vol}} (J, m)}{\partial J \partial J} = \frac{2}{D(m)} \end{aligned} \quad (\text{A.7})$$

B

Publications, Lectures and Posters

B.1 Publications and proceedings

- Josyula, S.P.; S. Diebels. 'Coupled diffusion and phase-field damage model to investigate moisture influence on fracture behaviour of viscoelastic elastomers', Computational Materials Science, Submitted.
- S.P. Josyula , M. Brede, O. Hesebeck, K. Koschek, W. Possart, A. Wulf, B. Zimmer, S. Diebels. 'Modelling the influence of moisture on the mechanical behaviour of crosslinked polyurethane adhesives', Computational Materials Science, Volume 246, 2025, ISSN 0927-0256, <https://doi.org/10.1016/j.commatsci.2024.113442>.
- Josyula, S.P.; Diebels, S. 'Numerical Investigation of Fracture Behaviour of Polyurethane Adhesives under the Influence of Moisture'. Polymers 2024, 16, 2676. <https://doi.org/10.3390/polym16182676>
- A. Wulf, O. Hesebeck, K. Koschek, M. Brede, B. Mayer, S.P. Josyula, S. Diebels, B. Zimmer, W. Possart [2021]. 'Berechnung des instationären mechanischen Verhaltens von alternden Klebverbindungen unter Einfluss von Wasser auf den Klebstoff'.

- Siva Pavan Josyula and Stefan Diebels [2019]. 'Phase-field damage model coupled with ageing in polymer adhesives due to moisture diffusion', In PAMM: Proceedings of the 8th GACM Colloquium on Computational Mechanics, Kassel, Germany.

B.2 Lectures

- A. Wulf, O. Hesebeck, K. Koschek, M. Brede, B. Mayer, S.P. Josyula, S. Diebels, B. Zimmer, W. Possart. 'Berechnung des instationären mechanischen Verhaltens von alternden Klebverbindungen unter Einfluss von Wasser auf den Klebstoff', 20. Kolloquium: Gemeinsame Forschung in der Klebtechnik, 3 - 4. March 2020, Marienberg, Würzburg.
- Siva Pavan Josyula, Selina Neuhaus, and Stefan Diebels. 'Modified phase-field fracture method to simulate the fracture behaviour in a polyurethane adhesive under stress relaxation', 7. GAMM workshop on phase-field modeling, 10. February 2020, Kaiserslautern.
- Siva Pavan Josyula and Stefan Diebels. 'Phase-field damage model coupled with ageing in polymer adhesives due to moisture diffusion', In PAMM: Proceedings of the 8th GACM Colloquium on Computational Mechanics, 28 - 30. August 2019, Kassel.
- Siva Pavan Josyula and Stefan Diebels. 'A phase-field approach describing degradation in aging polymer bonds', 12. Workshop Kontinuumsmechanik, 25 - 27. September 2019, Schwarzenborn.
- additionally five internal lectures and six lectures in the context of project meetings

B.3 Poster

- S. P. Josyula and S. Diebels, 'Phase-field Damage Model to Describe Aging in Polymer Adhesives due to Moisture Diffusion', Doktorandentag der Naturwissenschaftlich Technischen Fakultät III der Universität des Saarlandes, November 2019, Saarbrücken.